NTNU – Trondheim
Norwegian University of
Science and Technology

Corrosion Development in Welded AA6082 Alloys

Kim Blommedal

Materials Science and Engineering
Submission date: June 2013
Supervisor: Trond Furu, IMTE
Co-supervisor: Otto Lunder, IMT

Norwegian University of Science and Technology
Department of Materials Science and Engineering

Preface and Acknowledgements

This master thesis has been part of a collaboration between the author located at Norwegian University of Science and Technology (NTNU), and Ane Thorvaldsen at Sør-Trøndelag University College (HiST). Thorvaldsen has been responsible for carrying out SWAAT-testing of the alloys examined in this study[1]. The collaboration has been both informative and enjoyable, and I would like to thank Thorvaldsen for her effort and positive attitude throughout the study.

Moreover, I would like to show gratitude to my supervisors Dr. Trond Furu[2] and Dr. Otto Lunder[3] for their technical guidance and encouragement throughout this study. Also, the financial support provided by Hydro Aluminium is much appreciated. In particular, the visit to the Qatalum aluminium smelter plant in Doha, Qatar, was much appreciated and led to valuable motivation and knowledge utilized during this thesis.

Furthermore, the assistance provided by Hans Fostervoll [3] and Arne Gellein [3] during welding and ageing of the alloys is much appreciated. Also, I would like to show my gratitude to Terje Iveland [2] for his help and support during weld simulation.

Finally, I would like to thank professor Øystein Grong[4] for inspirational and informative discussions over the last couple of months.

Trondheim, June 2013
Kim Blommedal

[1] Ane Thorvaldsen, Korrosjonsoppførsel til ulike AA6082 ved forskjellige sveisemetoder. Bachelor Thesis, HiST, 2013.
[2] Hydro Aluminium, Sunndalsøra.
[3] SINTEF Materials and Chemistry, Trondheim.
[4] Norwegian University of Science and Technology (NTNU), Trondheim.

Abstract

AlMgSi alloys, frequently used as extruded profiles, generally show excellent corrosion resistance, as Mg is incorporated in the protective oxide layer, thus providing additional stabilization. However, localized corrosion forms such as intergranular corrosion (IGC) and pitting corrosion may occur as a result of improper heat treatment, or unfortunate alloying composition. In this study, four variants of AA6082 with Cu additions ranging from 0.001 to 0.60 wt% have been subjected to an accelerated IGC test, in addition to Cyclic Acidified Synthetic Sea Water (Fog) Testing (SWAAT). Moreover, the effects of welding on corrosion behaviour have been examined, and alloys have been subjected to both MIG welding, friction stir welding (FSW) and weld simulation. The effect of Cu content and ageing on the susceptibility to IGC and pitting corrosion have also been studied.

Results from this study revealed significant pitting corrosion on most variants, and the severity was found to increase with increasing Cu content and ageing time. Also, attacks from pitting corrosion was occasionally observed to be accompanied with IGC attack along sub grains. Moreover, the heat affected zone of samples welded by FSW and MIG displayed higher corrosion resistance as compared to the weld and the base metal. In addition, for the FSW variants, increased corrosion resistance was observed also for the base metal close to the heat affected zone. Despite such observations, no significant variation in corrosion potential as a function of distance from the weld could be observed. Finally, the weld seam formed during FSW proved more susceptible to attacks from pitting corrosion than the weld seam formed during MIG welding.

Sammendrag

AlMgSi-legeringer, ofte benyttet som ekstruderte profiler, viser utmerkede korrosjonsegenskaper ettersom Mg innlemmes i det beskyttende oksidsjiktet og dermed bidrar til ytterligere stabilisering av dette. Likevel kan lokale korrosjonsangrep som intekrystallinsk korrosjon (IKK) og gropkorrosjon inntreffe som en følge av ufullstendig varmebehandling, eller uheldig legeringssammensetning. I dette studiet har fire varianter av AA6082 med kobberinnhold mellom 0.001 og 0.60 wt% blitt utsatt for en akselerert IKK-test, i tillegg til en kunstig sjøvannstest (SWAAT). Videre har effekten av sveising på korrosjonsoppførselen blitt undersøkt og legeringen har blitt utsatt for både MIG sveising, friksjonssveising (FSW) og sveisesimulering. Effekten av kobberinnhold og utherding på følsomheten for IKK og gropkorrosjon har også blitt studert.

Resultater fra dette arbeidet avslørte betydelig gropkorrosjon på de fleste variantene, og graden av følsomhet ble observert til å øke med økende kobberinnhold og utherdingstid. I tillegg ble det funnet at gropkorrosjon i noen tilfeller var forbundet med IKK av subkorn. Videre ble det funnet at den varmepåvirkede sonen av de MIG sveiste og friksjonssveiste prøvene viste økt korrosjonsmostand, sammenlignet med sveis og grunnmateriale. I tillegg, for de friksjonseviste variantene, ble det påvist høy korrosjonsmostand også i deler av grunnmaterialet nære den varmepåvirkede sonen. På tross av nevnte funn, ble det ikke observert noen vesentlig endring i korrosjonspotensiale som funksjon av avstand fra sveis. Til slutt ble det observert at sveisefugen dannet etter friksjonsnsveising var mer følsom for gropkorrosjon enn sveisefugen dannet etter MIG sveising.

Contents

Preface iii

Table of Contents xi

List of Tables xiv

List of Figures xviii

List of Abbreviations xix

1. Introduction 1

2. Background 3
2.1. AlMgSi-alloys . . . 3
2.1.1. Temper designation . . . 3
2.2. Precipitation hardening . . . 4
2.2.1. Effect of Cu . . . 6
2.3. Welding . . . 7
2.3.1. Metal Inert Gas (MIG) welding . . . 7
2.3.2. Microstructure and strength evolution during MIG welding . . . 8
2.3.3. Friction Stir Welding (FSW) . . . 10
2.3.4. Microstructure and strength evolution during FSW . . . 11
2.4. Corrosion of aluminium . . . 13
2.5. Intergranular corrosion (IGC) . . . 13
2.5.1. Effect of chemical composition . . . 14
2.5.2. Effect of ageing and thermal processing . . . 17
2.5.3. Effect of quenching rate after extrusion . . . 20
2.5.4. Effect of microstructure . . . 20
2.6. Pitting corrosion . . . 21
2.7. Corrosion of welded AlMgSi-alloys . . . 26
2.7.1. Effect of filler wire . . . 28

3. Experimental 29
3.1. Alloys . . . 29

3.2. Process route . . . 30
3.2.1. Casting and homogenization . . . 30
3.2.2. Extrusion . . . 30
3.2.3. Artificial ageing . . . 31
3.3. Welding . . . 32
3.3.1. MIG welding . . . 32
3.3.2. Friction Stir Welding . . . 33
3.4. Weld simulation . . . 33
3.5. Post weld heat treatment (PWHT) . . . 37
3.6. Microstructure characterisation . . . 37
3.6.1. Sample preparation . . . 37
3.6.2. Optical microscope . . . 37
3.6.3. Anodising . . . 38
3.6.4. Hardness measurements . . . 38
3.6.5. Grain boundary microstructure . . . 39
3.7. Intergranular corrosion test . . . 39
3.8. SWAAT test . . . 40
3.8.1. Pit measurements . . . 43
3.9. Potential measurements . . . 43
3.10. Electrical conductivity measurements . . . 44

4. Results **45**
4.1. Material characterization . . . 45
4.1.1. Weld seam . . . 45
4.1.2. Microstructures . . . 46
4.2. Hardness profiles . . . 54
4.2.1. Samples subjected to FSW and MIG welding . . . 55
4.2.2. Weld simulated samples . . . 56
4.3. IGC test . . . 60
4.3.1. MIG welded samples . . . 60
4.3.2. FSW samples . . . 62
4.3.3. Weld simulated samples . . . 65
4.3.4. Weight loss measurements . . . 68
4.4. SWAAT test . . . 69
4.4.1. Samples welded by MIG and FSW . . . 71
4.4.2. Weld simulated samples . . . 77
4.5. Grain boundary microstructure . . . 83
4.5.1. Fe-rich particles . . . 84
4.5.2. Cu containing phases . . . 86
4.5.3. Fusion zone (MIG) . . . 88
4.6. Potential measurements . . . 90
4.7. Electrical conductivity . . . 91

5. Discussion **93**
5.1. As-received materials . . . 93
5.2. General corrosion resistance of tested alloys . . . 94

5.3. Effect of microstructure 95
5.4. Effect of quenching rate from elevated temperatures 96
5.5. Grain boundary precipitation and IGC susceptibility 97
5.6. Pitting corrosion susceptibility 98
5.6.1. Increased pitting resistance in the HAZ 99
5.6.2. Susceptibility of weld seam (FSW) 103
5.7. Further work 104

Conclusion **105**

References **107**

A. SWAAT - Inspection form **113**

B. Pitting measurements **114**

C. Temperature profiles during weld simulation **117**

D. Electrical conductivity measurements **119**

List of Tables

2.1. Selected mechanical properties for AlMgSi alloys 3
2.2. Overview over some selected temper designations 4

3.1. Chemical composition of the alloys examined in this study 29
3.2. Chemical composition of the filler wire used during MIG welding of alloy 6082-X 32
3.3. Selected welding parameters. 32
3.4. Peak temperatures at position of -14 mm from centre line during weld simulation 36
3.5. Operating parameters during particle analysis in LV FESEM. 39
3.6. Overview of samples tested for IGC 40
3.7. Composition of stock salt solutions prepared for the SWAAT test according to ASTM standard D1141-98 41
3.8. Overview of SWAAT-tested samples. 42

4.1. Hardness values and the corresponding standard deviation for the base material of the four alloys considered in this study. 54
4.2. Overview of observed corrosion modes including location of pitting and IGC attacks as a function of distance from centre line for weld simulated samples. 66
4.3. Weight loss measurements of all samples after IGC testing 68
4.4. Measured pit density, depth and size for all the SWAAT tested samples . . 70
4.5. Peak temperature regions and the corresponding distances from centre line. 81
4.6. Phases observed on grain boundaries for the alloys considered in this study 83
4.7. Average potential measurements for the different regions of MIG welded 6082-X / T6. 91

A.1. Regular inspections form during SWAAT testing of samples 113

B.1. Pit densities after SWAAT testing of weld simulated samples and samples subjected to MIG and FSW welding 114
B.2. Pit diameters after SWAAT testing of weld simulated samples and samples subjected to MIG and FSW welding 115

B.3. Pit depths after SWAAT testing of weld simulated samples and samples subjected to MIG and FSW welding 116

D.1. Electrical conductivity measurements across the welded section for alloy 6082-X /T6 subjected to MIG and FSW 119

List of Figures

2.1. Contributions from dissolved alloying elements in solid solution and particles from precipitation hardening 5
2.2. Effect of artificial ageing and naturally ageing on the strength evolution in AlMgSi alloys 6
2.3. Principles of the gas metal arc welding (GMAW) technique 7
2.4. Effect of artificial ageing (AA), welding (W) and post weld heat treatment (PWHT) on the microstructure evolution in AlMgSi alloys 8
2.5. Microstructure and strength evolution during GMAW 9
2.6. Principles of the friction stir welding (FSW) process 10
2.7. Classification of various regions in the friction stir weld 11
2.8. Microstructure and strength evolution during FSW 12
2.10. Corrosion rate as a function of Mn content in an AlMgSi alloy with various Fe levels 15
2.11. Conceptual illustration of the IGC mechanism 17
2.12. Isothermal time transformation (ITT) diagram illustrating various corrosion modes as a function of temperature and ageing time 18
2.13. Effect of ageing time on the susceptibility to IGC in an air cooled AlMgSi alloy 19
2.14. Effect of ageing time on the susceptibility to IGC in a water quenched AlMgSi alloy 19
2.15. Effect of cooling rate after extrusion on the susceptibility towards IGC . . 20
2.16. Pitting corrosion around an Al_3Fe particle and an oxide particle in an aluminium alloy 21
2.17. Effect of ageing on pitting potential in an Al-Cu alloy containing 3.33 wt% Cu 22
2.18. Dissolution potential of solid solution and some common intermetallic phases observed in aluminium alloys 24
2.19. Maximum pit depth as a function of exposure time for some selected alloys 25
2.20. Polarization curves for samples welded by GTAW and FSW 27
2.21. Polarization curves for T6-samples welded by GTAW and FSW 27

3.1. Temperature profile during artificial ageing of alloy 6082-X 31
3.2. Geometry of samples and placement of thermocouple for weld simulations 33

3.3. Experimental set-up of the Gleeble weld simulation station 34
3.4. Peak temperature profile for the specimens subjected to weld simulation . 35
3.5. Temperature profile during weld simulation of alloy 6082-A from T1 starting temper 36
3.6. Location of sections that have been examined in optical microscope after corrosion testing 38
3.7. Experimental set-up for the IGC test of weld simulated samples as well as samples subjected to FSW and MIG welding 40
3.8. Experimental set-up for the SWAAT test of weld simulated samples as well as samples subjected to FSW and MIG welding 42
3.9. Figure illustrating sections measuring 50x40 mm were pit analysis were done. Measurements were taken in the extrusion plane at one side of the centre line/ weld only. 43
3.10. Location of samples where potential measurements were done. All measurements presented in the figure are given in millimetres. 44

4.1. Macro images of weld seams after FSW and MIG welding of alloy 6082-X / T6 prior to corrosion testing 46
4.2. Optical micrographs of the base metal in alloy 6082-X 47
4.3. Micrographs of the welded section in alloy 6082-X after FSW and MIG welding 48
4.4. LV-FESEM secondary electron micrographs of alloy 6082-X across the welded section and the base material after MIG welding. 49
4.5. LV-FESEM secondary electron micrographs of alloy 6082-X across the welded section and the base material after FSW. 50
4.6. Micrographs of the base metal in alloy 6082-A 51
4.7. Micrographs of the base metal in alloy 6082-B 52
4.8. Micrographs of the base metal in alloy 6082-C 53
4.9. Hardness profiles of MIG welded AA6082-T6 and AA6082-T1. 55
4.10. Hardness profiles of 6082-X subjected to FSW and FSW with subsequent post weld heat treatment (PWHT) from T6 starting tempers 56
4.11. Hardness profile after weld simulation and post weld heat treatment (PWHT) of alloy 6082-A from T1 starting temper. 57
4.12. Hardness profile after weld simulation and post weld heat treatment (PWHT) of alloy 6082-B from T1 starting temper. 58
4.13. Hardness profile after weld simulation and post weld heat treatment (PWHT) of alloy 6082-C from T1 starting temper. 58
4.14. Hardness profile after weld simulation and post weld heat treatment (PWHT) of alloy 6082-X from T1 starting temper. 59
4.15. Hardness profile after weld simulation and post weld heat treatment (PWHT) of alloy 6082-X from T6 starting temper. 59
4.16. Corrosion of weld metal in 6082-X / T6 and 6082-X / T1 61
4.17. Intergranular corrosion of weld metal in alloy 6082-X. 61
4.18. Micrographs of corroded FSW samples 62
4.19. Pitting corrosion in the recrystallized layer in alloy 6082-X / T6 subjected to FSW and PWHT 63

4.20. Pitting corrosion in the nugget zone in alloy 6082-X / T6 subjected to FSW and PWHT 64
4.21. Micrographs of the corroded samples subjected to weld simulation and post weld heat treatment 65
4.22. Corrosion frequency of alloy 6082-A, 6082-B and 6082-C as a function of distance from centre line 66
4.23. Micrographs taken 5 mm from the centre line showing pitting and IGC in alloy 6082-C / T1 after PWHT. Micrographs taken parallel to the direction of extrusion. 67
4.24. Weight loss as a function of Cu-content on samples subjected to weld simulation and post weld heat treatment 69
4.25. Macro images after SWAAT testing of alloy 6082-X / T6 subjected to FSW and MIG as well as hardness profiles prior to corrosion testing 71
4.26. Micrographs of MIG welded 6082-X / T6 after SWAAT testing 72
4.27. Macro images after SWAAT testing of alloy 6082-X / T6 subjected to MIG where pits are highlighted. 73
4.28. Micrographs of sample friction welded 6082-X / T6 after SWAAT testing 73
4.29. Macro image showing a high density of pits in the centre of the friction weld in alloy 6082-X 74
4.30. Observed pit densities in the weld, the heat affected zone (HAZ) and the base material for alloy 6082-X / T6 welded by MIG and FSW 75
4.31. Observed pit diameters in the weld, the heat affected zone (HAZ) and the base material for alloy 6082-X / T6 welded by MIG and FSW. 76
4.32. Observed pit depths in the weld, the heat affected zone (HAZ) and the base material for alloy 6082-X / T6 welded by MIG and FSW. 76
4.33. Hardness profile and macro images after SWAAT testing of alloy 6082-X subjected to weld simulation and PWHT 78
4.34. Macro images after SWAAT testing of alloy 6082-A, 6082-B and 6082-C subjected to weld simulation and PWHT, as well as hardness profiles prior to corrosion testing 79
4.35. Corrosion attacks after SWAAT testing of weld simulated alloys 80
4.36. IGC and pitting corrosion after SWAAT testing of alloy 6082-X / T6 . . . 80
4.37. Observed pit densities for sample subjected to weld simulation and post weld heat treatment (PWHT) 81
4.38. Observed pit diameters for sample subjected to weld simulation and post weld heat treatment (PWHT) 82
4.39. Observed pit depths for sample subjected to weld simulation and post weld heat treatment (PWHT) 82
4.40. LV-FESEM secondary electron micrograph of a Fe-rich particle in alloy 6082-X 84
4.41. EDS analysis of a Fe-rich particle in alloy 6082-X 85
4.42. LV-FESEM secondary electron micrograph of a Cu-rich particle in alloy 6082-C 86
4.43. EDS analysis of a Cu containing particle in alloy 6082-C 87

4.44. LV-FESEM secondary electron micrograph of a particles in the weld metal of alloy 6082-X after MIG welding 88
4.45. EDS spectrum of precipitates in the weld metal in alloy 6082-X after MIG welding 89
4.46. Open circuit potential measurements of MIG welded 6082-X 90
4.47. Electrical conductivity of samples welded by MIG and FSW for various locations along the welded section. 91

5.1. Effect of microstructure on the susceptibility to IGC 95
5.2. Effect of welding on the microstructure evolution in artificially aged AlMgSi alloys 100
5.3. Galvanic effects of MIG welded samples. 102

C.1. Temperature profiles during weld simulation of all weld simulated alloys . 118

List of Abbreviations

β	Equilibrium phase (Mg_2Si)
β'	Hardening precipitate in AlMgSi alloys (semi-coherent rods)
β''	Hardening precipitate in AlMgSi alloys (semi-coherent needles)
R_m	Tensile strength
$R_{p0.2}$	Yield strength
EDS	Energy Dispersive Spectroscopy
FSW	Friction Stir Welding
GMAW	Gas Metal Arc Welding
GP-zones	Metastable Guinier-Preston zones that precipitate prior to the hardening β' and β'' particles
GTAW	Gas Tungsten Arc Welding
HAZ	Heat Affected Zone
HV	Hardness Vickers
HV1	Hardness Vickers - 1 kg load
HV5	Hardness Vickers - 5 kg load
IGC	Intergranular Corrosion
IKK	Interkrystallinsk Korrosjon
LV-FESEM	Low Vacuum Field Emission Scanning Electron Microscope
MIG	Metal Inert Gas
OCP	Open Circuit Potential
PFZ	Particle/Precipitation Free Zone
PWHT	Post Weld Heat Treatment
SSSS	Supersaturated Solid Solution

SWAAT	Cyclic Acidified Synthetic Sea Water (Fog) Testing
T1	Alloy cooled from an elevated temperature shaping step and naturally aged to a stable condition
T6	Alloy solution-treated and artificially aged to peak strength
TMAZ	Thermomechanically Affected Zone

1 Introduction

It is believed that 25% of the undiscovered oil and gas resources in the world are located in the Arctic region [1]. As a result, during the last decades oil extraction in the Arctic region has received considerable amount of attention, as oil and gas companies strive do meet the demands materials have to fulfil in such harsh environments. Traditionally, various steel qualities have been the preferable material selection for both subsea and topside installations offshore. However, with increasing focus on the petroleum reservoirs located in the Arctic regions, additional requirements have to be considered. Such requirements include superior low temperature properties, high strength-to-weight ratios as well as excellent corrosion resistance and weldability. Aluminium alloys fulfil all these requirements, and should consequently be regarded as a promising material in future oil and gas installations in the Arctic region. In fact, the density of aluminium is approximately $1/3$ of that of steels, which allows significant weight reduction of future pipelines and offshore installations. Such considerations are of up-most importance as these structures have to be transported from the manufacture site to the installation site in the Arctic. Lastly, the excellent corrosion resistance may result in the maintenance costs on platforms installations and pipelines being drastically lowered.

More than anything, aluminium is a green material. In fact, recycling of scrap aluminium only requires 5 % of the energy that was originally used to produce the metal in the first place. Moreover, emission of green house gases such as CO_2 are greatly reduced as a result of such favourable recycling processes. As a matter of fact, the Norwegian aluminium company Hydro claims that the annual emission of CO_2-gases are reduced by 92 million tons as a result of the recycling process alone [2].

AlMgSi alloys, often referred to as the 6000 series, are wrought alloys that are extensively applied within the transport industry, as well as for architectural and marine applications. The main application is as extruded products and approximately half of all extruded profiles produced world wide are AlMgSi alloys [3]. Alloy 6082, examined in this study, is a high strength alloy which can be extruded as long as the geometry is not too complex. Due to its strength, the alloy frequently serves as a load bearing material. Applications include stairs, platforms, handrails and bridges, as well as offshore applications and ship structures.

However, despite the superior corrosion resistance, localized corrosion attacks such as intergranular corrosion (IGC) and pitting corrosion may occur as a result of unfavourable

thermal processing or alloying content. Copper is often added to increase the overall strength of the alloy. However, numerous studies [4–14] have reported that alloys containing Cu, or excess Si, may prove susceptible to IGC and pitting corrosion. Despite wide agreement on the detrimental effects from Cu on the corrosion resistance, a lower concentration which prevents corrosion is yet to be determined. It was originally suggested that a Cu concentration of 0.4 wt% was needed in order to promote IGC [14]. However, aggressive attacks from IGC has recently been reported in AlMgSi(Cu) alloys with Cu content as low as 0.12 wt% [10]. In addition, slow cooling after extrusion, or under ageing, is considered unfortunate with respect to corrosion resistance and IGC in particular. Overageing, on the other hand, is regarded to promote attacks from pitting corrosion.

Objectives of thesis

The effect of welding on the corrosion resistance in AlMgSi alloys, despite its industrial importance, has not received considerable attention and is not fully understood. As a result, this study aims to examine the effect of both metal inert gas (MIG) welding, friction stir welding (FSW) and weld simulation on localized corrosion attacks such as IGC and pitting corrosion. Welding of aluminium results in heating of the metal causing substantial redistribution of alloying elements, which in turn will affect the mechanical properties and possibly also the corrosion resistance.

In this study, four variants of aluminium alloy AA6082 have been subjected to an accelerated IGC test as well as a cyclic acidified synthetic sea water test (SWAAT). Moreover, the four variants were alloys with Cu contents ranging from 0.001 to 0.60 wt% and Mg/Si ratios ranging from 0.62 to 0.69. As a result, all tested alloys contained significant amounts of excess Si. Also, as all the tested alloys were extruded products, the effect of microstructure on corrosion behaviour has also been evaluated. In fact, studies have suggested that a deformed fibrous structure as a result of extrusion may prove beneficial with respect to the corrosion resistance [4, 15].

Furthermore, the corrosion resistance at various locations from the weld zone has been evaluated, preferably by the means of optical microscopy. Also, potential measurements and electrical conductivity measurements have been carried out in order to evaluate the susceptibility towards localized corrosion. Finally, simple weight loss measurements have been performed on all variants in order to estimate the corrosion rate.

2 | Background

2.1. AlMgSi-alloys

AlMgSi-alloys contain Mg and Si in the range of 0.5-1.3 and 0.4-1.4 wt% respectively, in addition to other trace elements and contaminations such as Fe, Mn, Cr, Cu and Zn. In a balanced alloy the ratio between Mg and Si is 1.73, which is equivalent to the observed ratio between Mg and Si in the equilibrium phase β (Mg_2Si) [4]. This ratio is of importance with regards to corrosion and will be discussed in greater detail in section 2.5. An important feature of these alloys is the ability to increase their strength through artificial ageing. As a result, the mechanical properties of these alloys can be manipulated as seen by the strength range in table 2.1.

Table 2.1.: *Some selected mechanical properties for the AlMgSi alloys [3].*

Selected mechanical properties	
$R_{p0.2}$	190-360 MPa
R_m	220-390 MPa
Elongation	12-17%

Moreover, the far most important application of these alloys is in the form of extruded profiles, and over 2 million extruded AlMgSi profiles are produced annually [3]. Other important applications include tubing, as well as rolled and forged products [16].

2.1.1. Temper designation

Properties of aluminium alloys can be manipulated to a great extent by a variety of different heat treatments. AlMgSi alloys are often age-hardened to increase their strength through precipitation hardening which is discussed in section 2.2. Table 2.2 below summarizes the main temper designations applied to age-hardened alloys.

Table 2.2.: *Overview over some selected temper designations [17].*

Selected temper designations	
T1	Cooled from an elevated temperature shaping step and naturally aged to a stable condition
T3	Solution-treated, cold worked and naturally aged
T4	Solution-treated and naturally aged
T6	Solution-treated and artificially aged to peak strength
T7	Solution-treated and overaged

2.2. Precipitation hardening

The overall hardness, and hence the yield strength, of AlMgSi alloys is the sum of three contributions as seen in equation 2.1 below.

$$\sigma_y = \sigma_i + \sigma_{ss} + \sigma_p \tag{2.1}$$

Here σ_i is the intrinsic contribution for pure aluminium, σ_{ss} is the contribution from alloying elements in solid solution and σ_p is the contribution from hardening particles (i.e. precipitation hardening). The contributions from dissolved alloying elements in solid solution and particles from precipitation hardening are illustrated in figure 2.1. As seen in the figure, both bypassing and shearing of hardening particles by dislocations contribute to the total increase in strength [18–20]. Moreover, bypassing is recognized by dislocation movement through larger particles, whereas they move by a shearing mechanism in the case of smaller particles. A peak in strength is observed for a mixture of bypassing and shearing mechanisms. In this section only the contribution to strength from hardening particles will be discussed.

Precipitation hardening occurs as a result of artificial ageing where the alloy is first heated to a temperature above the solvus line, however still below the eutectic temperature to avoid local melting of the alloy. This first initial step is known as solution heat treatment and is usually performed at temperatures close to 530 $^{\circ}\mathrm{C}$ for 30 minutes, followed by quenching to room temperature. All alloying elements are then in solid solution and are said to be in a supersaturated solid solution (SSSS). The second step during artificial ageing involves heating the alloy to an intermediate temperature, usually 150-190 $^{\circ}\mathrm{C}$ [12]. However, a temperature range of 70-300 $^{\circ}\mathrm{C}$ may theoretically be used and will result in precipitation of hardening precipitates. During artificial ageing a series of metastable phases will precipitate with increasing holding time, until the equilibrium phase β (Mg_2Si) forms if the alloy is overaged. The precipitation sequence is dependent on alloying elements present and the ratio between Si and Mg. For a balanced alloy, containing Si and Mg in stoichiometric ratio (i.e. Mg/Si = 1.73), the precipitation sequence may be written as:

$$\textit{SSSS} \rightarrow \textit{solute clusters} \rightarrow \textit{GP-zones} \rightarrow \beta'' \rightarrow \beta' \rightarrow \beta\ (Mg_2Si) \tag{2.2}$$

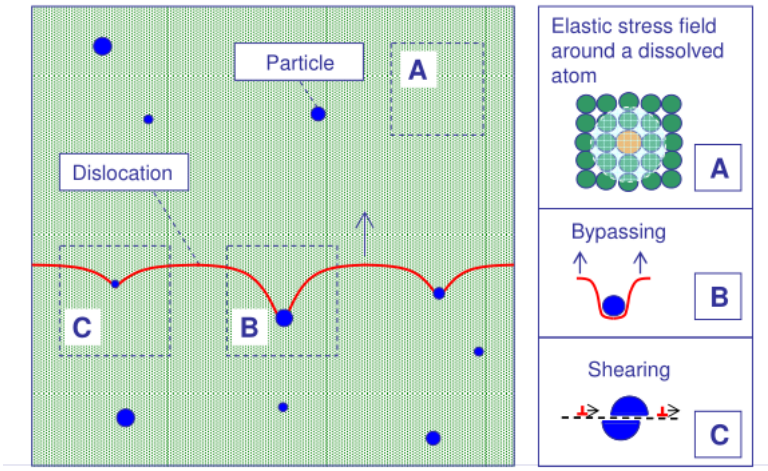

Figure 2.1.: *Contributions from dissolved alloying elements in solid solution (A) and particles from precipitation hardening (B,C). Dislocations may either move through bypassing (B) of larger particles or shearing in the case of smaller particles (C) [20].*

As can be seen from figure 2.2, a peak in strength is observed for a given mixture of β' and β'' precipitates. An important difference between these precipitates is their morphology. The β'' phase is monoclinal consisting of semi-coherent needles, whereas the β' phase is coarser and heaxagonal consisting of semi-coherent rods [3]. The chemical composition of the β'' phase was initially believed to be Mg_5Si_6, however recent studies indicate that the composition should be $Mg_5Al_2Si_4$ [12]. The composition of β' is believed to be $Mg_{1.8}Si$ [21]. Finally, if the alloy is overaged (e.g. during welding), the equilibrium phase β (Mg_2Si) forms which is completely incoherent and is regarded as a brittle and unfavourable phase, due to the severe reduction in hardness as indicated by figure 2.2. However, as can be seen in the same figure, if naturally ageing is performed only GP-zones will form and the precipitation sequence will be incomplete. In other words, alloys that are naturally aged will usually be significantly softer than alloys that have undergone controlled artificial ageing. Also, GP-zones are thermally unstable, and alloys that are naturally aged may lose their strength rather easily during thermal cycles such as welding.

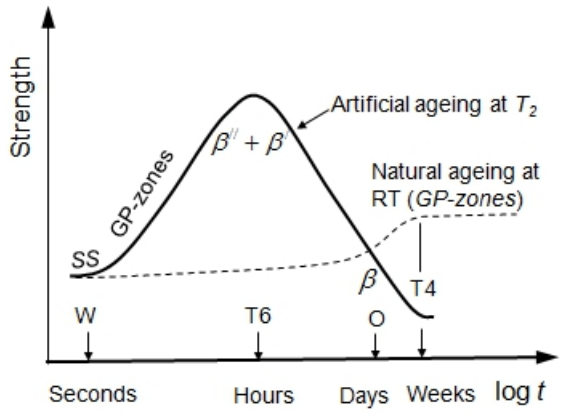

Figure 2.2.: *Effect of artificial ageing and naturally ageing on the strength evolution in AlMgSi alloys. Naturally ageing only allows GP-zones to form [22].*

2.2.1. Effect of Cu

Esmaeili and Lloyd [23] studied the effect of Cu addition on the precipitation kinetics in AlMgSi alloys. The authors found that Cu tended to increase the precipitation rate if solution heat treatment and quenching were immediately followed by artificial ageing. For pre-aged alloys, on the other hand, no correlation between Cu additions and precipitation kinetics were found. This theory was later confirmed by Marioara et al. [21] who showed that Cu containing alloys displayed hardness values greater than Cu-free alloys, due to a higher volume fraction of precipitates. Moreover, for Cu-rich alloys, the precipitation sequence may be written as [4, 24]:

$$SSSS \rightarrow \text{solute clusters} \rightarrow \textit{GP-zones} \rightarrow \textit{Q'} \rightarrow \textit{Q} \tag{2.3}$$

The chemical composition of the Q' and Q phases are similar [24], however the stoichiometry is yet to be determined. Some suggested compositions are $Al_3Mg_9Si_7Cu_2$ [25], $Al_5Mg_8Si_6Cu_2$ [14] and $Al_4Mg_8Si_7Cu_2$ [6]. In this study, the latter composition will be used.

2.3. Welding

Welding of aluminium is usually performed either by fusion welding or solid state welding. During fusion welding the weld is melted, whereas solid state welding only allows heating of the weld without any melting taking place. Moreover, important methods within fusion welding and solid state welding are Metal Inert Gas (MIG) welding and Friction Stir Welding (FSW) respectively. As a result, these techniques are presented in the following.

2.3.1. Metal Inert Gas (MIG) welding

MIG welding, or gas metal arc welding (GMAW), is a welding method that is frequently applied industrially and can be used to weld a vast variety of materials. The principle of MIG welding is shown in figure 2.3 below. A consumable wire is fed continuously from a wire feeder and act both as filler metal and electrode. When the wire touches the parent metal an arc is established and metal is transferred. The transfer mode depends on the current and the wire diameter. The arc and the weld pool are protected by the shielding gas which often is an inert gas such as argon or helium.

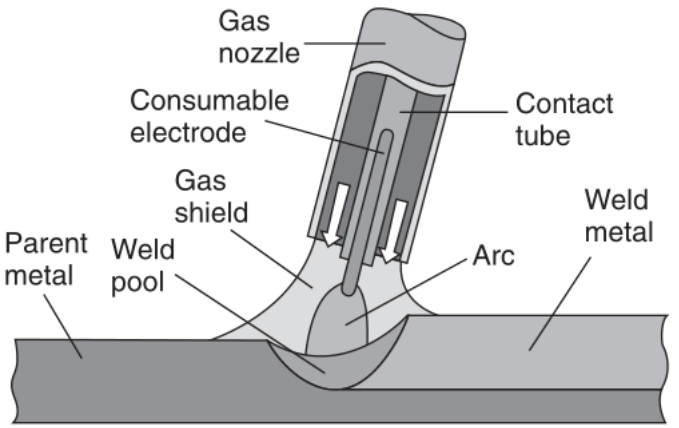

Figure 2.3.: *Figure illustrating the principles of the gas metal arc welding (GMAW) technique [16].*

MIG welding can be performed in all positions and provides high welding speeds as well as excellent oxide film removal [16]. A major problem that arises during fusion welding of aluminium is significant softening of the alloy both in the weld, as well as in the heat affected zone. This problem will be addressed in some further detail in section 2.3.2.

2.3.2. Microstructure and strength evolution during MIG welding

As already discussed in the section concerning MIG welding, fusion welding of aluminium alloys will always cause degradation of the mechanical properties of the region in proximity of the weld, known as the heat affected zone (HAZ). This degradation can be explained by the dissolution of the hardening precipitates β'' and β' [18]. Also, the weld metal itself is melted and will upon solidification form an as-cast microstructure which is susceptible to hot cracking [26].

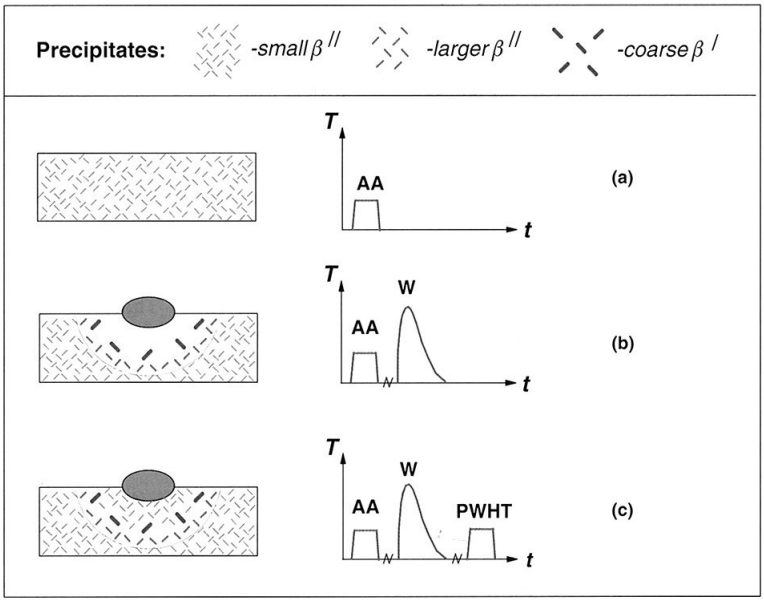

Figure 2.4.: *Effect of thermal cycles such as artificial ageing (AA), welding (W) and post weld heat treatment (PWHT) on the microstructure evolution in AlMgSi alloys [18].*

Changes in the microstructure, and strength of fusion welded AlMgSi alloys, were studied by Myhr et al. [18] and Grong [22]. A simplified overview of the microstructure evolution during artificial ageing (AA), fusion welding (W) and post weld heat treatment (PWHT) is presented in figure 2.4.

The artificially aged alloy contains small high-density hardening precipitates (β'') which are distributed throughout the material. However, when subjected to high temperatures, such as welding, the smallest particles are dissolved at the expense of the larger precipitates which are allowed to grow (i.e. Ostwald ripening principle). This dissolution process may start at temperatures as low as 250 °C [18]. However, in the region closest to the weld all hardening precipitates are dissolved and the microstructure is said to be fully reverted. As a result, a substantial decrease in hardness is expected in this region. However, a small increase in hardness after welding may be observed due to effects of natural ageing.

Consequently, the position of minimum strength in the HAZ is shifted to the partly reverted region, were coarsening of hardening precipitates has taken place. As a result, a soft zone is formed some distance from the fusion line. In fact, studies have shown that the minimum strength in the HAZ of AA6082-T6 may be in the order of 140 MPa, whereas the strength in the base metal is in the order of 280 MPa [27]. As a result, a strength reduction of approximately 50 % may be expected during fusion welding of aluminium alloys.

Finally, depending on the concentration of vacancy clusters and solute in the matrix, PWHT of the alloy may allow reprecipitation of the β'' precipitates close to the fusion line, which will provide some strength recovery (figure 2.4c). Figure 2.5 presents a typical temperature profile and strength evolution through the HAZ of a MIG welded aluminium alloy.

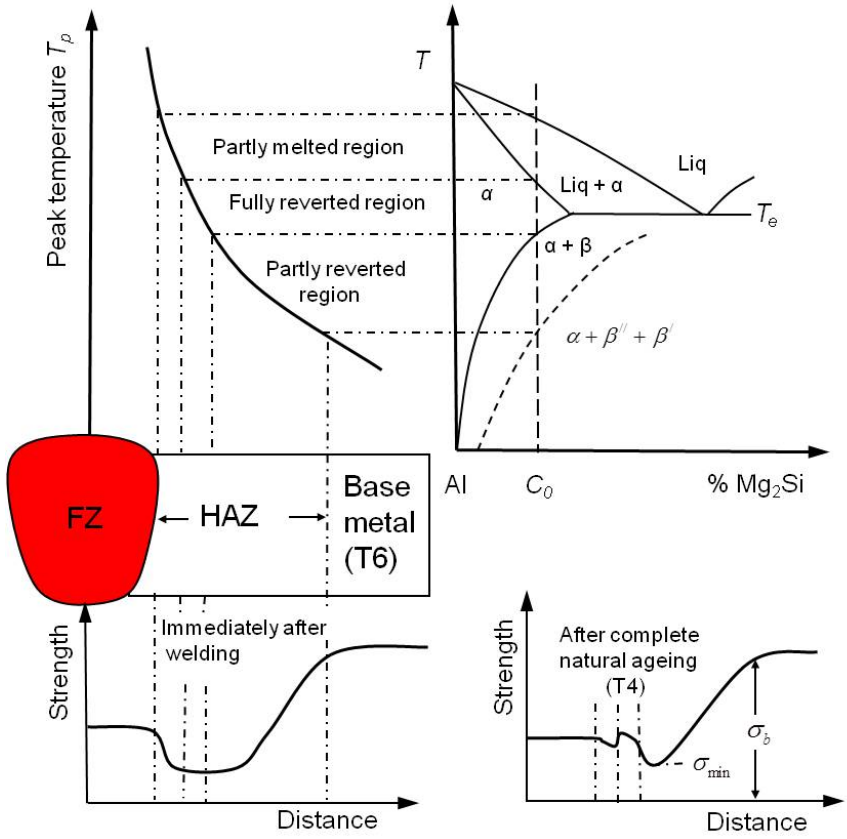

Figure 2.5.: *Microstructure and strength evolution during GMAW.* ***Top part of figure****: Formation of various microstructural regions after single pass butt welding of a T6 tempered alloy.* ***Bottom part of figure****: Strength evolution across the HAZ of the plate immediately after welding and after complete naturally ageing [22].*

2.3.3. Friction Stir Welding (FSW)

Friction stir welding (FSW), invented in 1991, is probably the most important welding technique with respect to cold welding of aluminium. In this process a wear resistant tool is allowed to rotate on the work piece, which plastically deforms and heats the aluminium sheets that are to be welded (figure 2.6). By moving the probe in the direction of the joint line, plastically deformed material will flow from the front to the rear of the probe [16]. The main advantage concerning FSW is the prevention of a fusion zone as no melting of metal takes place, which prevents cracks in the weld metal. Instead, a thermomechanically affected zone (TMAZ) forms which is affected both by the deformation introduced during welding as well as frictional heat.

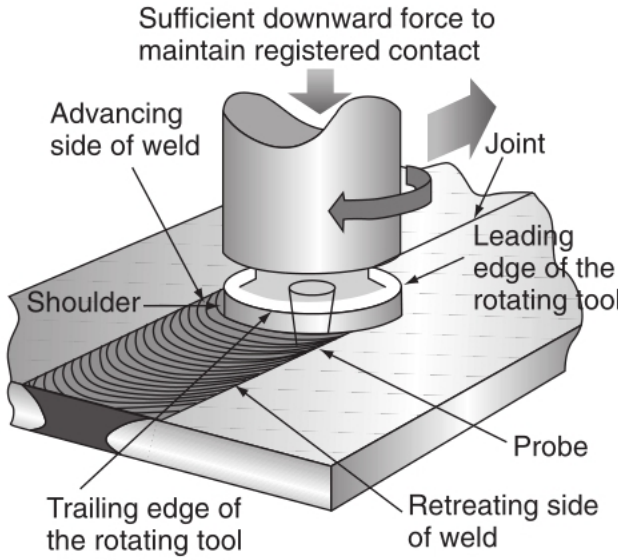

Figure 2.6.: *Figure illustrating the principles of the friction stir welding process [16].*

Moreover. the FSW technique allows dissimilar alloys, or alloys that cannot be joined by fusion welding, to be welded. Also, FSW provides a fine grained microstructure with improved mechanical properties compared to those obtained with fusion welding. Finally, studies have shown that FSW results in improved corrosion resistance in welded joints [28, 29]. The corrosion resistance of welded AlMgSi alloys will be discussed in greater detail in section 2.7.

The friction stir weld may be divided into various sections depending on the microstructure after welding. Moreover, an examples of such a classification is shown in figure 2.7. Such zones include the weld nugget, the thermomechanically affected zone (TMAZ) and the heat affected zone (HAZ).

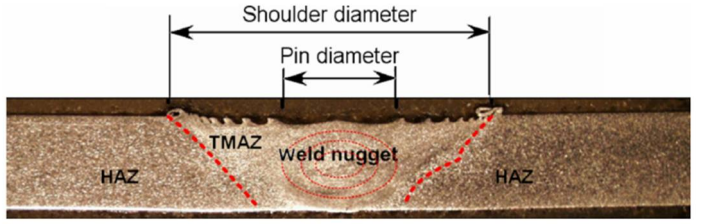

Figure 2.7.: *Classification of various regions in the friction stir weld [30].*

2.3.4. Microstructure and strength evolution during FSW

The main advantage associated with friction stir welds is the prevention of the as-cast microstructure associated with MIG welds, as the temperature never exceeds the melting point of the alloy. In fact, the maximum temperature rarely exceeds the eutectic temperature in order to prevent local melting of the alloy [31]. Nevertheless, despite the reduction in temperature, a significant strength reduction in the HAZ is expected as indicated by figure 2.8. In fact, the minimum strength in the HAZ of butt-welded AA6082-T6 may be in the order of 150 MPa [31, 32]. As a result, the minimum strength in the HAZ is only slightly improved by the use of FSW as compared to MIG welding. Also, effects of natural ageing seen after MIG welding is normally not observed in alloys welded by FSW.

During friction welding of aluminium alloys a fine-grained microstructure is usually formed in the centre of the weld. Such a favourable microstructure is formed due to recrystallization processes which arises due to friction heat, as well as heat generated during plastic deformation of the metal. Moreover, the grain size in the weld centre increases with increasing peak temperature and rotation speed during welding.

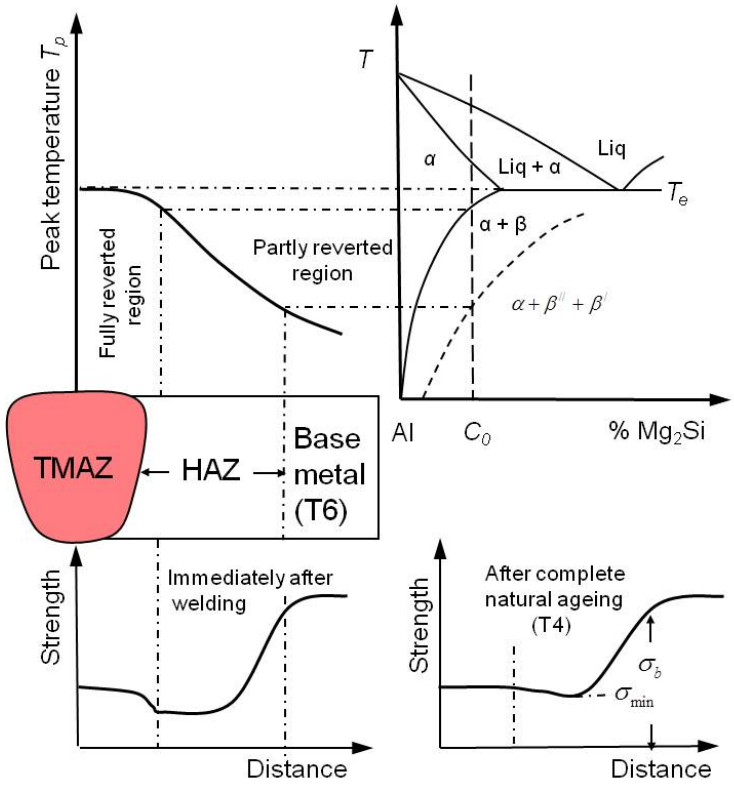

Figure 2.8.: *Microstructure and strength evolution during FSW.* ***Top part of figure****: Formation of various microstructural regions after single pass butt welding of a T6 tempered alloy.* ***Bottom part of figure****: Strength evolution across the HAZ of the plate immediately after welding and after complete naturally ageing [22].*

2.4. Corrosion of aluminium

AlMgSi alloys are generally expected to show excellent corrosion resistance as Mg is incorporated in the oxide layer which acts as a stabilizing agent. However, localized corrosion attacks such as intergranular corrosion (IGC) and pitting corrosion have been observed in numerous alloys, particularly those containing copper [4–14, 33]. In the following sections these localized corrosion forms are discussed in some greater detail, and recent studies on these topics are presented.

Section 2.5 includes studies on both IGC and pitting corrosion, however with main focus on the former corrosion form. Moreover, section 2.6 is dedicated to pitting corrosion only, whereas section 2.7 deals with corrosion of welded AlMgSi alloys.

2.5. Intergranular corrosion (IGC)

Intergranular corrosion (IGC) is a localized form of corrosion that arises due to potential differences between the grain boundaries and the aluminium matrix. The potential difference develops due to precipitation of cathodic or anodic phases at the grain boundary. In AlMgSi alloys such precipitate are often cathodic as ennobling elements Cu and Si tend to migrate to the grain boundaries. However, precipitates may also be anodic e.g. when Mg-rich precipitates forms, as in some weld metals. In the case of intermetallic phases forming at the grain boundaries, a depletion region close to the grain boundary forms which becomes active. A suggested mechanism responsible for IGC in AlMgSi(Cu) alloys developed by Svenningsen et al. [5], is shown in figure 2.9.

Moreover, recent examinations [4–10] suggest that copper is the element that causes the most severe IGC attacks in AlMgSi alloys, as it tends to form continuous Cu-rich phases at the grain boundaries (Q-phase). It should however be noted that other alloying elements may cause susceptibility to IGC, with Si being the prime example. In fact, Si concentrations in excess of what is required to form Mg_2Si (i.e. Mg/Si < 1.73), has been reported to cause susceptibility to IGC [4]. Based on the above mentioned studies, the main causes to IGC in AlMgSi alloys can be summarized as the following:

1. Alloy contains Cu.
2. Improper thermomechanical treatment (e.g. underageing, slow cooling after extrusion).
3. Alloy contains excess Si beyond what is required to form Mg_2Si.
4. Unfavourable microstructure (e.g. high angle grain boundaries)

It is, however, important to note that the above list is not absolute, and a range of parameters may effect the overall susceptibility. Some important effects that has been observed during the last decade are presented in the following sections.

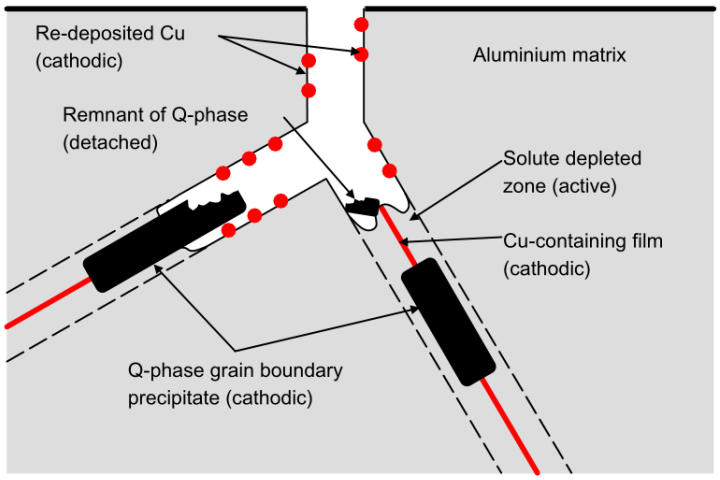

Figure 2.9.: *Suggested IGC mechanism in Cu containing AlMgSi alloys. The Q-phase is a Cu-rich cathodic precipitate with the chemical composition being* $Al_4Mg_8Si_7Cu_2$ *[5, 6]*

2.5.1. Effect of chemical composition

Perhaps the most important factor with regards to IGC susceptibility is the chemical composition of the exposed alloy. In the following a presentation of the main alloying elements in AlMgSi alloys are presented, and their effect on the corrosion resistance is discussed.

Cu and Si

Copper is often added to AlMgSi alloys to increase the strength of the alloy through solid solution hardening, as well as accelerating the precipitation sequence as seen in section 2.2.1. However, as will be seen in the following, alloys that contain copper are reported to display reduced corrosion resistance to localized corrosion and intergranular corrosion in particular.

Mondolfo [14] first stated that alloys containing 0.3-0.4 wt % Cu or excess Si occasionally proved susceptible to IGC. In this context the term excess silicon refers to an unbalanced alloy containing Si beyond what is required to form Mg_2Si, meaning Mg/Si ratios below 1.73 [4]. Recent examinations [4–13] reflect the importance of Cu content on the susceptibility towards IGC. The above-mentioned Cu-limits, however, appear to be too high. In fact, IGC has been observed for Cu contents as low as 0.12 wt% [10]. Despite numerous studies on the effect of Cu on IGC suscpetibility over the last decades, an accurate Cu-limit is yet to be found. This may be linked to the fact that the sensitivity to IGC is a complex issue and several parameters need to be taken into account such as effects of thermal history, microstructure and welding.

Whether it is excess Si or Cu that has the greatest influence on the sensitivity to IGC, has been given some attention in the literature. However, most studies suggest that the Cu content of the alloy is the dominating factor. Si forms coarse precipitates at the grain boundaries which are not as detrimental as in the case of Cu, which tends to cause knife-line attacks [4]. Moreover, Zhan et al. [11] did not observe any correlation between the Mg/Si ratio and the susceptibility to IGC. In fact, the sensitivity was solely controlled by the Cu content. In this study, the Si content was fixed at 1 wt%, whereas the Mg and Cu contents were allowed to vary. However, Si depletion around the grain boundary seems to play a vital role in establishing active zones at the grain boundaries, which is necessary in order to stimulate the propagation of IGC [4].

Mn and Fe

Fe forms cathodic intermetallic phases with aluminium (Al_3Fe and Al_6Fe) which may cause severe attacks in the form of pitting corrosion in aluminium alloys [4, 34, 35]. This effect may be counterbalanced by additions of Mn as it combines with iron, thus forming less harmful AlMnFe phases [36, 34]. These phases may also combine with Si, thus improving the resistance to IGC, as well as the corrosion resistance in general. Figure 2.10 illustrates the positive effects of Mn addition in an AlMgSi alloy containing 1.0 and 0.7 wt % of Si and Mg respectively, where the loss in strength due to corrosion is drastically reduced with increasing Mn addditions. The figure is based on studies by Chadwick et al. [37] reported by Mondolfo [14]. It should, however, be ntoed that the beneficial effects from Mn additions were not observed in the absence of iron. In the study case the samples were immersed in 3 wt% NaCl and 1 vol% HCl for 24 hours.

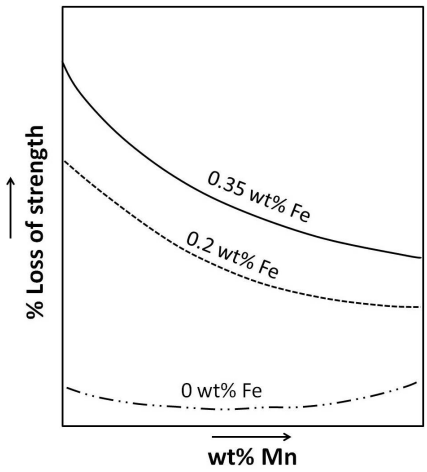

Figure 2.10.: *Figure illustrates the corrosion rate as a function of Mn content in an AlMgSi alloy with various Fe levels. Figure is based on studies by Chadwick et al. [37] as reported by Mondolfo [14]. An interesting observation is the increase in corrosion rate with increasing Mn additions for Fe-lean alloys. However, for medium and high Fe-levels the positive effects of Mn are apparent.*

Finally, Mn may restrict grain boundary precipitation, thus lowering the susceptibility towards IGC [14, 36, 37]. In fact, Mondolfo [36] stated that the corrosion resistance was the property that was affected the most by Mn additions.

Mg

In solid solution Mg is not expected to effect the corrosion behaviour in AlMgSi alloys, and only a minimal change in corrosion potential has been observd [38]. However, Mg tend to combine with Al thus forming anodic intermetallic phases. The equilibrium phase Mg_2Si could also cause susceptibility to IGC, as the phase is active compared to the surrounding Al-matrix [39–41]. However, the phase tends to become depleted in Mg and transforms into silicon oxide which is insulating. As a result, Mg_2Si precipitates does not seem to be as detrimental as the Cu-rich Q-phase. Nevertheless, during MIG welding of aluminium Mg-rich filler metals are often used. As a result, weld metals may prove susceptible to IGC as anodic phases such as Al_3Mg_2 or Al_8Mg_5 may form.

Cr and Zn

Cr is reported to increase the overall corrosion behaviour in AlMgSi alloys, as it tends to form innocuous compounds with the more harmful elements Si and Fe [39]. Additions of Zn shifts the corrosion potential in negative (active) direction, and should consequently oppose the detrimental effects of Cu. However, additions up to 0.5 wt% has not been shown to provide any additional corrosion resistance [14].

2.5.2. Effect of ageing and thermal processing

The effect of ageing on the susceptibility towards IGC is an issue that has lead to some disagreement among scientists over the last decades. Mondolfo [14] first suggested that the peak aged (T6) alloys were the ones that proved most vulnerable to attacks from IGC. These observations were also reported later in a study by El-Menshawy et al. [42]. Furthermore, Minoda et al. [15] found corrosion attacks 300 μm deep in a 6061-T6 alloy containing 0.33 wt% Cu.

However, recent examinations [4, 5, 8–10] suggest that alloys that are underaged display the highest susceptibility to IGC (figure 2.11). The susceptibility was reported to decrease with ageing to a peak strength temper condition. As a matter of fact, majority of studies on

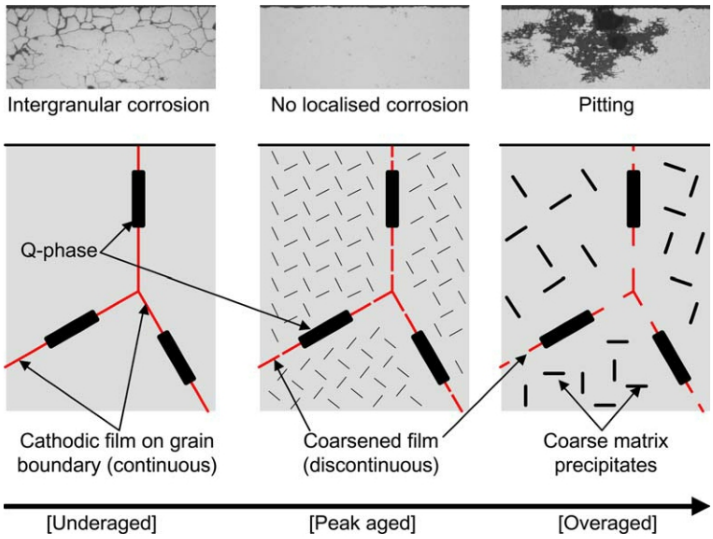

Figure 2.11.: *Figure illustrates the mechanisms responsible for the different corrosion modes observed during ageing of an AlMgSi alloy containing 0.13 wt% Cu. The mechanism suggest that a continuous Q-phase is of vital importance in order for intergranular corrosion to be observed. [5]*

the effect of ageing indicate increasing IGC resistance in peak strength alloys compared to underaged alloys. Studies by Svenningsen et al. [5, 8–10] and Hurlen Larsen et al. [4] all strongly indicate increasing susceptibility to IGC in underaged AlMgSi alloys, as opposed to those which are peak aged. These findings were explained by the detrimental Cu-film becoming discontinuous with increasing ageing time, thus reducing the driving force for IGC formation. Figure 2.12 shows an isothermal time transformation (ITT) diagram developed by Svenningsen et al. on the basis of numerous samples of an AlMgSi alloy containing 0.13 wt% Cu. As can be seen from the diagram, no IGC attacks could be observed for holding times corresponding to a peak aged sample (i.e. 185 °C for 5 hours). However, for underaged samples IGC attacks were reported. For the overaged samples, on the other hand, pitting corrosion was the dominating corrosion mode.

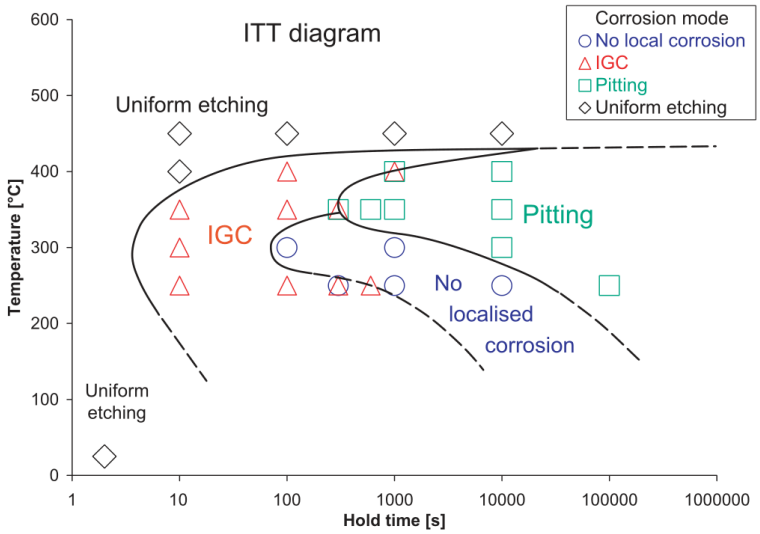

Figure 2.12.: *Isothermal time transformation (ITT) diagram illustrating various corrosion modes as a function of temperature and holding time (i.e. ageing time) in AlMgSi alloys. Diagram is empirically developed by Svenningsen et al. [8].*

The effect of artificial ageing on solution heat treated alloys, followed by air cooling and water quenching are shown in figure 2.13 and 2.14 respectively. For the air cooled samples a marked decrease in IGC attacks can be observed for increasing ageing time, until almost no corrosion can be seen. However, overageing resulted in localized corrosion. For the water quenched samples the attacks were observed to be even more aggressive than for the air cooled samples, particularly in the underaged state. However, as opposed to the air cooled samples, IGC was observed in the peak aged state, although the attacks were greatly reduced as compared to the underaged state.

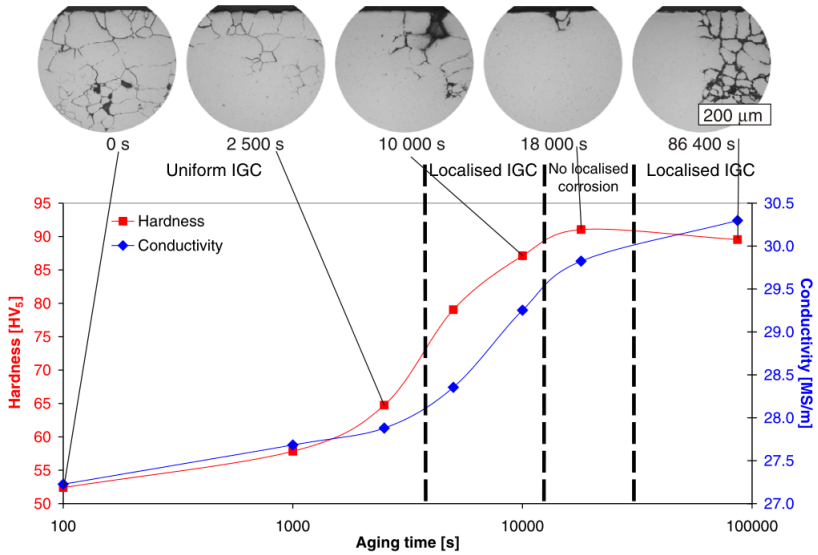

Figure 2.13.: *Effect of ageing time on the susceptibility to IGC in an air cooled AlMgSi alloy containing 0.60, 0.55 and 0.17 wt% of Si, Mg and Cu respectively [9].*

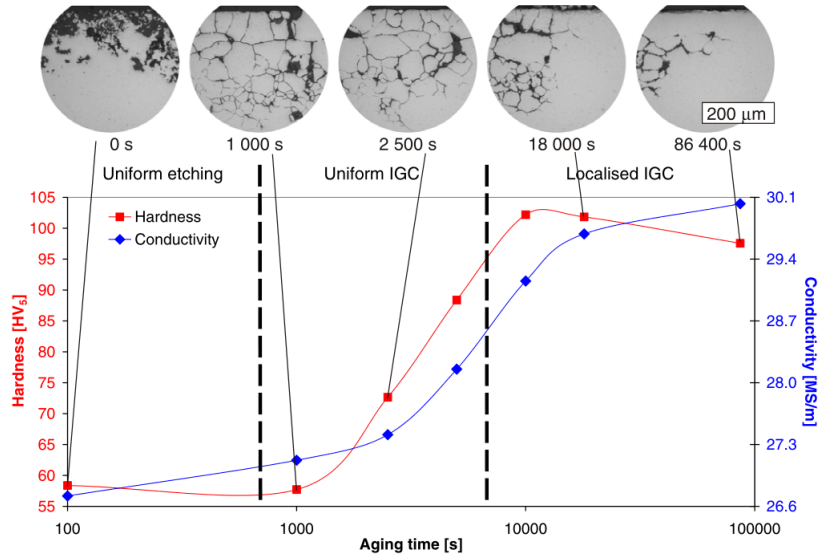

Figure 2.14.: *Effect of ageing time on the susceptibility to IGC in a water quenched AlMgSi alloy containing 0.60, 0.55 and 0.17 wt% of Si, Mg and Cu respectively [9].*

2.5.3. Effect of quenching rate after extrusion

Svenningsen et al. [8–10] and Hurlen Larsen et al. [4] observed how the susceptibility towards IGC was affected by quenching rate after extrusion. Figure 2.15 shows micrographs of the alloy in naturally aged temper condition when subjected to **A)** air cooling and **B)** water quenching. The authors concluded that the air cooled samples proved to be far more susceptible to IGC, than those which were rapidly quenched in water. These findings were explained by extensive precipitation of Q-phase ($Al_4Mg_8Si_7Cu_2$) and β-phase (Mg_2Si) on the grain boundaries in the air cooled samples, which are known to cause attacks from IGC as already mentioned. For the water quenched samples, however, this precipitation was limited.

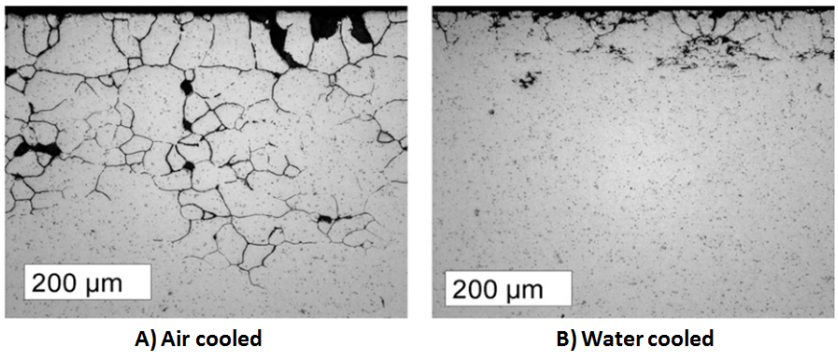

Figure 2.15.: *Effect of cooling rate after extrusion on the susceptibility towards IGC in an AlMgSi alloy containing 0.60, 0.55 and 0.17 wt% of Si, Mg and Cu respectively.* ***A)*** *Air cooled and* ***B)*** *Water quenched [9].*

2.5.4. Effect of microstructure

Some studies have examined the correlation between microstructure and sensitivity to IGC. Hurlen Larsen et al. [4] found that a fibrous microstructure proved beneficial with respect to the corrosion resistance of the alloy. Profiles consisting of a coarse recrystallized layer and fine grains mid-thickness, were characterized by IGC attacks limited to the recrystallized layer. Another study by Minoda and Yoshida [15] showed that high angle bondaries, typically observed in the recrystallized layer, were sensitive to IGC. Low angle boundaries, however, proved more corrosion resistant. These findings were explained by the fact that particle free zones (PFZ), and grain boundary precipitates, more easily form on high angle boundaries as opposed to low angle boundaries.

2.6. Pitting corrosion

Frankel defined pitting corrosion as "*localized accelerated dissolution of metal that occurs as a result of breakdown of the otherwise protective passive film on the metal surface*" [43]. The corrosion form, and particular its propagation stage, is closely related to that observed for crevice corrosion [44, 45]. Moreover, in aluminium alloys, pitting corrosion is strongly related to second phase particles, such as intermetallic phases, resulting in significant local changes in the corrosion potential. As a result, a potential difference arises which may give rise to the growth of pits. However, the importance of these second phase particles is not fully understood [43].

Intermetallic particles form due to low solubility of most alloying elements in aluminium. The main precipitates that form in AlMgSi alloys are considered to be Fe intermetallics and $MgSi$ particle types [40]. Figure 2.16 illustrates a suggested mechanism of pitting corrosion around a Al_3Fe particle.

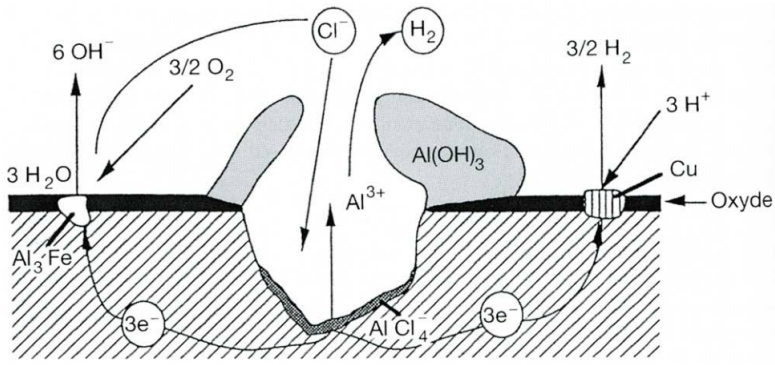

Figure 2.16.: *Pitting corrosion around a Al_3Fe particle and an oxide particle in an aluminium alloy [46].*

Park et al. [35] studied the role of Al_3Fe particles in AA6061. The authors suggested that pitting occurred as a result of alkaline dissolution of the aluminium matrix around the particles, which transforms into acidic fast growing pits. However, this mechanism fails to explain the observed transformation from alkaline cavities to acidic pits.

Moreover, Nisancioglu [34] observed that initially cathodic Al_3Fe phases were dealloyed on Al when sunjected to a NaOH solution. Depletion of Al from the particle was found to be detrimental to cathodic behaviour, due to the formation of a Fe-rich protective oxide on the surface of the particle. Moreover, enrichment of Si and Mn to the Al_3Fe phase resulted in a reduction of both the cathodic and anodic reaction rate. Moreover, according to Eckermann et al. [40], some uncertainty exists regarding the importance of MgSi and Si precipitates on the corrosion behaviour in AlMgSi alloys, although the particles have been reported to active corrosion mechanisms. The authors observed that selective dissolution

of Mg on MgSi phases started immediately after immersion of the samples in a 1 M NaCl solution. As a result, Si-oxides are left in the matrix which are insulating and does not cause any corrosion to take place. However, MgSi remnants were reported to increase the cathodic current by a factor of three which could cause corrosion, especially if other intermeallic particles (i.e. Fe-rich phases) were inactive.

However, the effect of Cu content on pit density during the initiation stage seems to be clear. In fact, the pit density is found to increase from 100 pits per cm^{-2} in AA1199 to 1000 pits cm^{-2} in an alloy containing 4 wt% Cu [17]. Moreover, Cu located in solid solution is noble to the aluminium matrix and the pitting potential is reported to increase significantly with increasing Cu content [47]. However, copper tends to form intermetallic particles which may be both noble and active (e.g. Al_2CuMg). Moreover, Muller and Galvele [47] observed that ageing of an Al-Cu alloy reduced the corrosion potential. In fact, a decrease of over 100 mV was reported as can be seen in figure 2.17. In this study ageing was done at 240 °C on an alloy containing 3.33 wt% Cu which was immersed in 1 M NaCl.

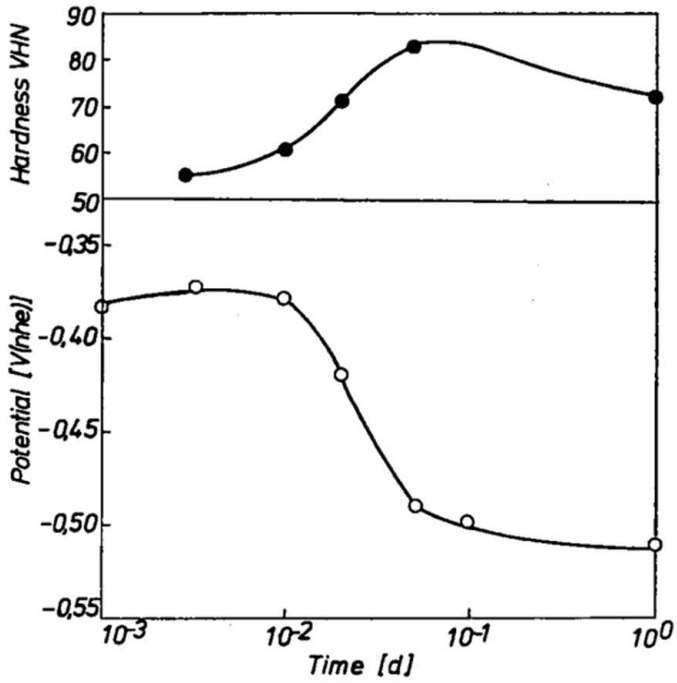

Figure 2.17.: *Effect of ageing on pitting potential in an Al-Cu alloy containing 3.33 wt% Cu. [47].*

These findings are in accordance with studies by Hurlen Larsen et al. and Svenningsen et al. [4, 5, 8–10] presented in section 2.5.2 which suggested that overaged samples were particular susceptible to pitting corrosion.

The initiation stage for pitting corrosion is not fully understood despite numerous studies and suggested models [48]. However, a fundamental criteria for initiation of pitting corrosion, is the presence of aggressive ions such as chlorides. In order to maintain electronegativity in the pit, chloride ions will start to migrate to the bottom of the pit were Al^{3+} dissolves according to equation 2.4.

$$2Al \rightarrow 2Al^{3+} + 6e^- \tag{2.4}$$

The possible cathodic reactions are the reduction of hydrogen and oxygen according to equation 2.5 and 2.6 respectively [46].

$$6H^+ + 6e^- \rightarrow 3H_2 \tag{2.5}$$

$$\frac{3}{2}O_2 + 3H_2O + 6e^- \rightarrow 6OH^- \tag{2.6}$$

As can be seen from the above equations, the pH will increase locally as hydroxide ions are formed and hydrogen ions are consumed. The overall reaction now becomes (eq. 2.7):

$$2Al + 3H_2O + \frac{3}{2}O_2 \rightarrow 2Al(OH)_3 \tag{2.7}$$

Furthermore, hydrolysis of the dissolved aluminium ions will occur according to equation 2.8.

$$Al^{3+} + 3H_2O \rightarrow Al(OH)_3 + 3H^+ \tag{2.8}$$

The corrosion product $Al(OH)_3$ is a white substance which is easily detected by the naked eye. Some common phases observed in aluminium alloys and their dissolution potential is shown in figure 2.18.

Solid solution	Dissolution potential (mV SCE)	Intermetallic phase
	−170	Si
	−430	Al_3Ni
	−470	Al_3Fe
Al–4Cu	−610	
	−640	Al_2Cu
Al–1Mn	−650	
1050A	−750	
	−760	Al_6Mn
Al–3Mg	−780	
Al–5Mg	−790	
Al–1Zn	−850	
	−910	Al_2CuMg
	−960	$MgZn_2$
Al–5Zn	−970	
	−1150	Al_3Mg_2
	−1190	Mg_2Si

Figure 2.18.: *Dissolution potential of solid solution and some common intermetallic phases observed in aluminium alloys [46].*

Bardal [49] reported how the depth of pits in AlSiMg alloys developed with time when exposed to artificial sea water, and the results are shown in figure 2.19. Moreover, it was found that the depth of the pits could be described by the following relation:

$$d = Kt^{1/3} \tag{2.9}$$

In the above equation d is the depth of the growth given in micrometers and t is the exposure time given in months. The constant K depends on parameters such as type of alloy, exposed area and environment. However, it should be noted that equation 2.9 is not always valid, and the exponent may deviate from 1/3 particularly during the initiation phase.

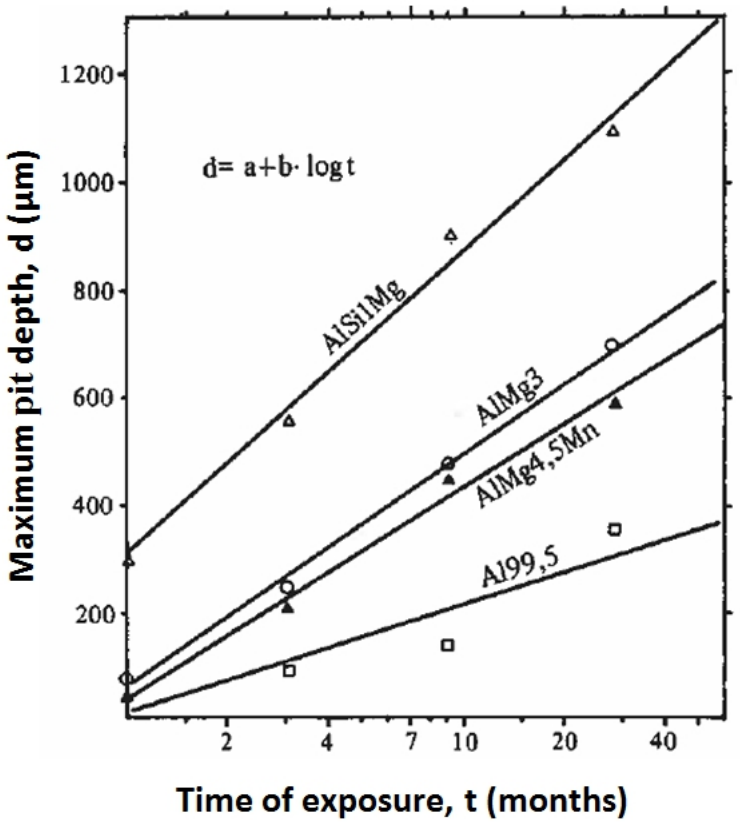

Figure 2.19.: *Maximum pit depth as a function of exposure time for some selected alloys [49].*

2.7. Corrosion of welded AlMgSi-alloys

The corrosion properties of welded AlMgSi alloys is an issue that has been given some attention only during the very last couple of years, and most studies are carried out within the last decade. Such a study was done by Ruan et al. [50] where the corrosion behaviour of robotic MIG-welded AA6082-T6 was examined. The filler wire used was ER5356 which contained 4.88 wt% magnesium. The authors found pitting corrosion both on the base material and the weld seam. However, uniform corrosion was observed on the weld seam as well as some grain boundary corrosion. This corrosion behaviour was not observed on the base metal. In conclusion, the base material displayed improved corrosion resistance as compared to the weld seam.

Majority of studies on corrosion of welded aluminium profiles have, however, been concerned with alloys welded by solid state processes such as friction stir welding (FSW). Monetta et al. [51] studied the effect of welding parameters on the corrosion behaviour of friction stir welded AA6056 from a T78[1] starting temper. It was found that a lower welding speed provided the highest corrosion resistance. As for the above-mentioned case study by Ruan et al., the dominant corrosion mode was reported to be pitting, however, grain boundary corrosion was also observed. An interesting observation was made by the authors in this study, as they observed that intergranular corrosion was always accompanied with pitting attacks. Finally IGC was observed both on the surface of the samples as well as inside the pits. However, what should be noted in this study is the Cu content of the test samples being as high as 0.96 wt %.

Moreover, in a study by Fahimpour et al. [29], welding of AA6061-T6 containing 0.19 wt% Cu was done both by FSW, as well as by gas tungsten arc welding (GTAW) . In other words a comparison was done between a solid state welding method (FSW) and one involving a fusion zone (GTAW). For the profiles welded using GTAW a filler wire containing 5 wt% Si was used (AA4043). For both welding methods the most aggressive corrosion attacks were found in the welded section. Moreover, it was concluded that FSW provided improved corrosion resistance as compared to GTAW. Finally, heat treatment of the welded region to a T6 temper condition provided improved corrosion resistance. In fact, the corrosion resistance was in some cases found to be higher than in the base metal.

Another comparison of the corrosion behaviour between GTAW and FSW of an AlMgSi alloy was made by Maggiolino and Schmid [28]. The authors found that the corrosion resistance was reduced in the welded region, however, the samples welded using GTAW were found to be more susceptible to localized corrosion attacks as seen in figure 2.20. Moreover, heat treatment of the welded samples to a T6 temper condition (i.e. PWHT) shifted the corrosion potential in a positive direction. This effect was found to be pronounced in the welded region compared to the base metal as shown in figure 2.21.

[1] The T78 temper condition involved solution heat treatment at 550 °C followed by air cooling to room temperature. Furthermore, after welding, the alloy were heat treated at 175 °C for 6 hours and 13 hours at 190 °C.

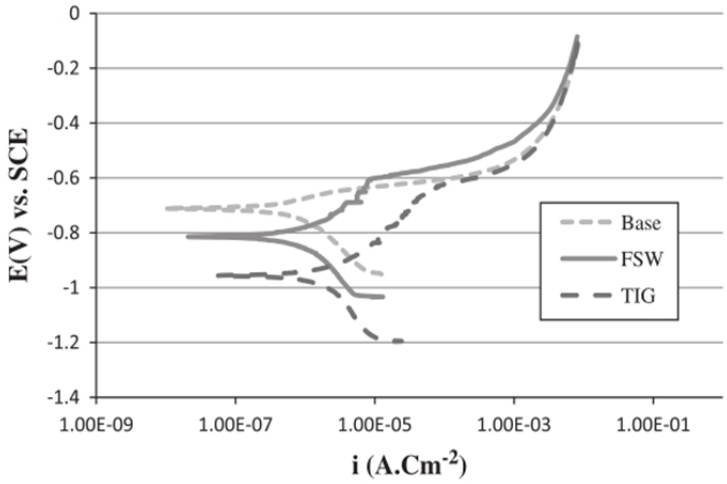

Figure 2.20.: *Polarization curves for samples welded by GTAW (TIG in figure) and FSW in addition to the base metal [29].*

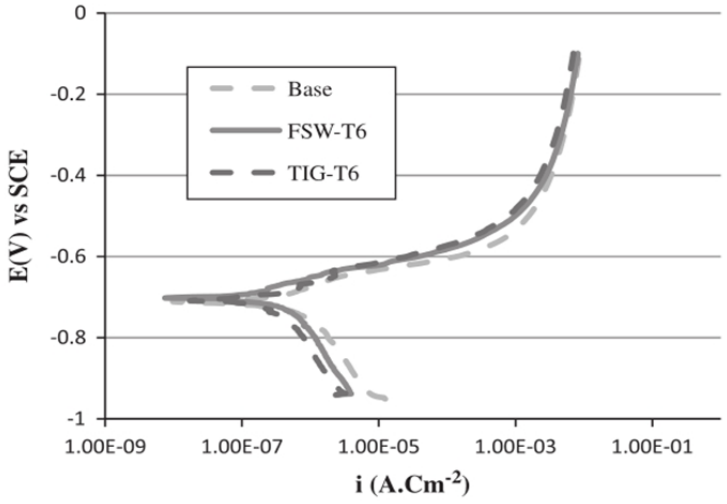

Figure 2.21.: *Polarization curves for T6-samples welded by GTAW (TIG in figure) and FSW in addition to the base metal [29].*

2.7.1. Effect of filler wire

A study by Metwally and Mosalam (1996) [26] compared the corrosion resistance of two Mg-rich filler alloys (AA5356 and AA5183) and a Si-rich filler alloy (AA4043). In this study the authors found that the Mg-rich filler alloys proved to be more susceptible to IGC than the Si-rich filler alloy. These findings were explained by the formation of active Mg_2Al_3 phases along the grain boundaries. For the Si-rich alloy, on the other hand, the corrosion resistance was found to be superior compared to the Mg-rich filler metals.

3 | Experimental

3.1. Alloys

In this study four different variants of aluminium alloy AA6082 has been subjected to an accelerated IGC test and a Cyclic Acidified Synthetic Sea Water (Fog) Test (SWAAT). The chemical compositions of the alloys are given in table 3.1.

Table 3.1.: *Chemical composition of the alloys examined in this study along with the Mg/Si ratio. All the compositions are given in wt%. Elements with concentrations lower than 0.001 wt% are not listed.*

	6082-X	**6082-A**	**6082-B**	**6082-C**
Si	1.04	0.96	0.95	1.00
Mg	0.64	0.66	0.65	0.68
Mn	0.53	0.56	0.57	0.59
Fe	0.21	0.27	0.27	0.28
Cu	0.002	0.001	0.10	0.60
Cr	0.00	0.16	0.16	0.16
Ti	0.01	0.01	0.01	0.01
Ga	0.01	0.01	0.01	0.01
B	0.002	0.002	0.002	0.003
V	0.010	0.002	0.002	0.002
Al	Bal	Bal	Bal	Bal
Mg/Si	0.62	0.69	0.68	0.68

All samples are extruded products with thickness of 2 mm for alloys 6082-A, 6082-B and 6082-C, and 3 mm for alloy 6082-X.

3.2. Process route

In the following a presentation of the history of the as-received profiles is presented. This includes casting, homogenisation, extrusion and finally artificial ageing for selected samples.

3.2.1. Casting and homogenization

The received alloys were direct chill (DC) cast at Hydro Research and Technology Development (RTD) centre located at Sunndalsøra, producing billets with diameters of 203 mm and lengths of 3.25 meters. Furthermore, the billets were homogenized by heating to 580 °C with a heating rate of 200 °C / h. After holding for two hours the alloys were cooled to room temperature with a cooling rate of 300-350 °C / h.

3.2.2. Extrusion

Extrusion was performed separately for alloy 6082-X and alloys 6082-A, 6082-B and 6082-C. As a result, a separate characterization is presented in the following.

Alloy 6082-X

Extrusion of alloy 6082-X was performed at Hydro Aluminium Profiler at Raufoss industrial plant producing profiles 205 mm wide with a thickness of 3 mm. The billet temperature was 515 °C and the extrusion velocity was 5-6 m/min. The extruded profiles were first spray-cooled until a temperature of 360 °C was reached, followed by cooling in room temperature with a cooling rate of 200 °C/h. The extrusion step was followed by solution heat treatment of the profiles in lab furnaces at 540 °C for 30 minutes, followed by quenching in water.

Alloys 6082-A, 6082-B and 6082-C

Extrusion of alloys 6082-A, 6082-B and 6082-C were done at SINTEF Materials and Chemistry at NTNU, Trondheim by the use of a 800 ton hydraulic press and induction heating coils. Prior to extrusion the billets were preheated to 410 °C. The extrusion step was performed at velocities of approximately 4 mm/s, producing profiles 40 mm wide with thickness of approximately 2 mm. The extrusion step was followed by solution heat treatment in lab furnaces at 530 °C for 15 minutes, followed by quenching in water.

3.2.3. Artificial ageing

All alloys had been stored for approximately fours years before artificial ageing was performed. As a result, contributions from naturally ageing is considered to be substantial. Nevertheless, artificial ageing was performed on selected samples of all alloys. However, satisfactory results were only obtained for alloy 6082-X. This issue is discussed in further detail in section 5.1. All samples subjected to artificial ageing were aged directly from their naturally aged condition (T1). All of the profiles that were friction stir welded were artificially aged prior to the welding cycle. However MIG welding, as well as weld simulation, were performed both on artificially aged and naturally aged profiles.

Artificial ageing was done by the use of air circulations furnaces at SINTEF Materials and Chemistry, Trondheim. The profiles were heated to 185 °C by a heating rate of 200 °C/h and held at this temperature for 5 hours, before being air cooled to room temperature. The measured temperature profile during artificial ageing of ally 6082-X is shown in figure 3.1 below. Thermocouples (type K) were placed both in the middle of the furnace between two plates (blue line), and at the top of all the profiles (red line). As can be seen, the heating rate was found to be slightly lower between the profiles as compared to the top part of the furnace.

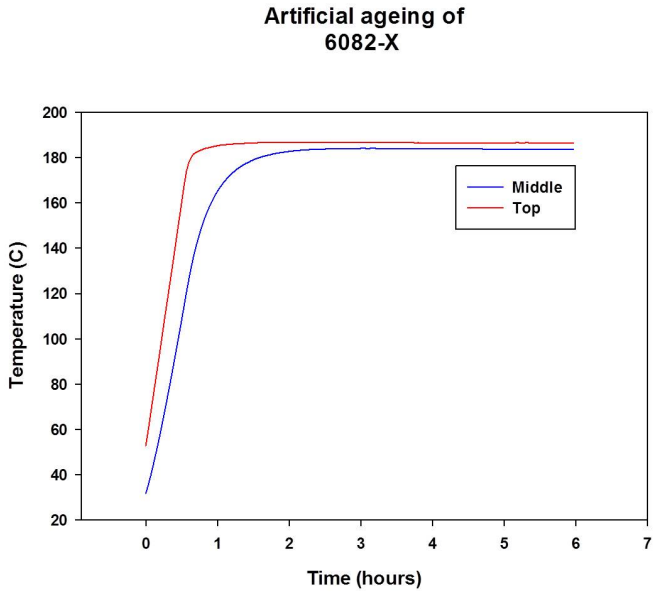

Figure 3.1.: *Temperature profile during artificial ageing of alloy 6082-X. Two thermocouples were used to monitor the temperature, one between two plates in the middle (blue line) and another at the top part of the profiles (red line).*

3.3. Welding

In this study the effects of fusion welding (MIG), friction stir welding (FSW) and weld simulation have been investigated. MIG welding and FSW were only performed on alloy 6082-X, whereas weld simulation was done on all alloys.

3.3.1. MIG welding

Robotic MIG welding was performed on alloy 6082-X from T6 and T1 starting tempers on profiles measuring 0.3 x 20 x 40 cm at SINTEF Materials and Chemistry at NTNU, Trondheim. The filler wire used was AA5183 with chemical composition shown in table 3.2.

Table 3.2.: *Chemical composition of the filler wire used during MIG welding of alloy 6082-X [52]. All compositions are given in wt%.*

Filler wire	Si	Mg	Mn	Fe	Cu	Cr	Ti	Zn	Al
AA5183	0.4	4.8	0.8	<0.40	<0.10	0.15	<0.15	<0.25	Bal

Prior to the welding cycle, the profiles to be welded very heavily clamped which resulted in thermal stresses in the as-welded condition. Moreover, a stainless steel backing plate was used for all welding experiments. Finally, the oxide layer close to the weld joint was mechanically removed prior to welding. Main welding parameters are presented in table 3.3 below.

Table 3.3.: *Selected welding parameters.*

Parameter	Value
Filler wire	AA5183
Shielding gas	4.6 Ar
Heat input	0.10 kJ/mm^2
Welding speed	10 mm/s
Plate gap	1 mm
Plate thickness	3 mm
Mean current	165-170 A
Potential	22 V
Push angle	$\sim 15\,^\circ$

3.3.2. Friction Stir Welding

Friction stir welding was performed on alloy 6082-X from a T6 starting temper on profiles measuring 0.3 x 20 x 100 cm. The welding was performed at Marine Aluminium AS, Husøy according to standard practice at the facility. However, due to confidentiality reasons, no further details are presented.

3.4. Weld simulation

In order to simulate a fusion welding technique, such as MIG welding, weld simulation was performed. Such simulation should ideally reflect the temperature profile and microstructural changes during fusion welding, with exception of the fusion zone itself as no melting of the material occurs.

Weld simulations were performed at Hydro R&D Center located at Sunndalsøra by the use of a Gleeble 3500 thermal system. The geometry of samples and placement of the thermocouple are shown in figure 3.2. Weld simulation was carried out on samples 6082-A, 6082-B and 6082-C from T1 starting tempers. For alloy 6082-X weld simulation was performed for both T1 and T6 starting tempers.

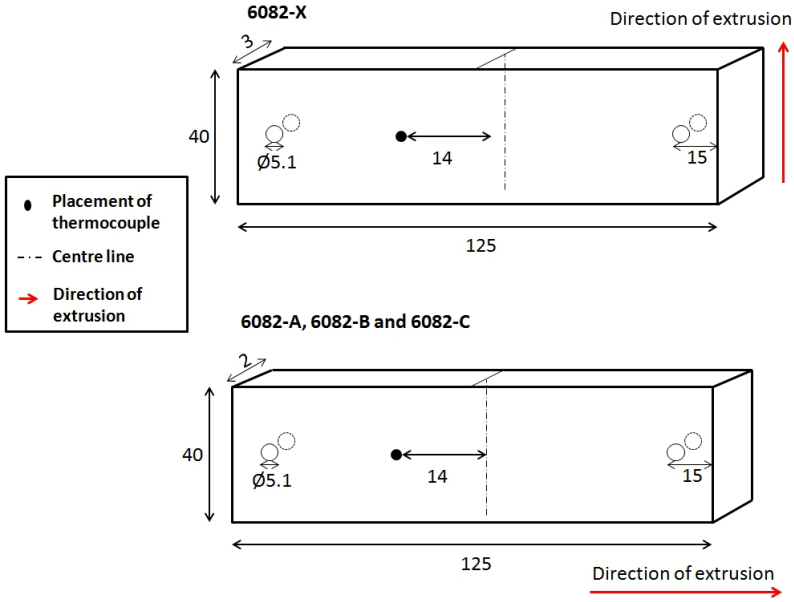

Figure 3.2.: *Figure shows the geometry of samples and the placement of thermocouple for weld simulations. Note that the direction of extrusion and plate thickness were different for alloy 6082-X* ***(upper figure)*** *as compared to alloys 6082-A, 6082-B and 6082-C* ***(lower figure)****. All the measurements are given in millimetres.*

The specimens were heated by the direct resistance heating (the Joule effect), which involves heating the alloys by passing a direct current through two clamps at each side of the aluminium sample. The heating rate was set to approximately 100 $^{\circ}\mathrm{C}/s$. Moreover, the temperature, and hence the current flowing, was monitored by a spot welded K-type thermocouple placed 14 mm from the centre line. A placement of 14 mm from the centre line was chosen in order to observe the temperature evolution in the heat affected zone. Water cooled aluminium jaws at each side allowed efficient extraction of heat from the samples to occur, which caused the temperature profile to be parabolic as seen in figure 3.4. In addition, Cu wedges were used in order to allow heat to be extracted more efficiently. The experimental set-up for weld simulation of the samples is illustrated in figure 3.3.

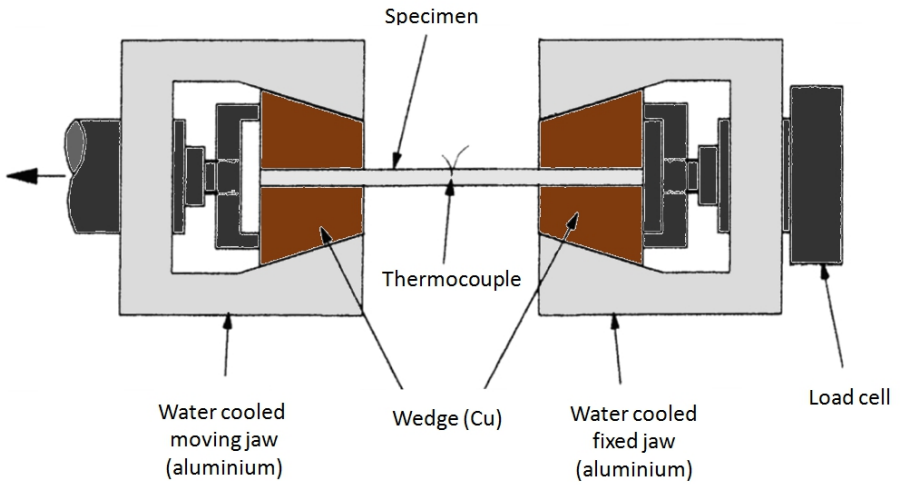

Figure 3.3.: *Experimental set-up of the Gleeble weld simulation station. Figure is not to scale.*

In order to calibrate the Gleeble machine, thermocouples were initially placed at positions of -20, -14, 0 and +20 mm from the centre of the specimen. The resulting peak temperature profile as a function of distance from the centre line is shown in figure 3.4. The chosen thermal profile allowed the centre of the specimen to be heated to approximately 560 $^{\circ}\mathrm{C}$ for 2 seconds, before undergoing controlled cooling. The peak temperature was chosen in order to get a temperature profile through the HAZ which could correlate to ordinary fusion welding of AlMgSi alloys. However, in order to avoid local melting of the alloy, no higher temperatures were attempted. As can be seen, the profile is not completely symmetric due to uneven extraction of heat from the cooling jaws during the weld simulation cycle.

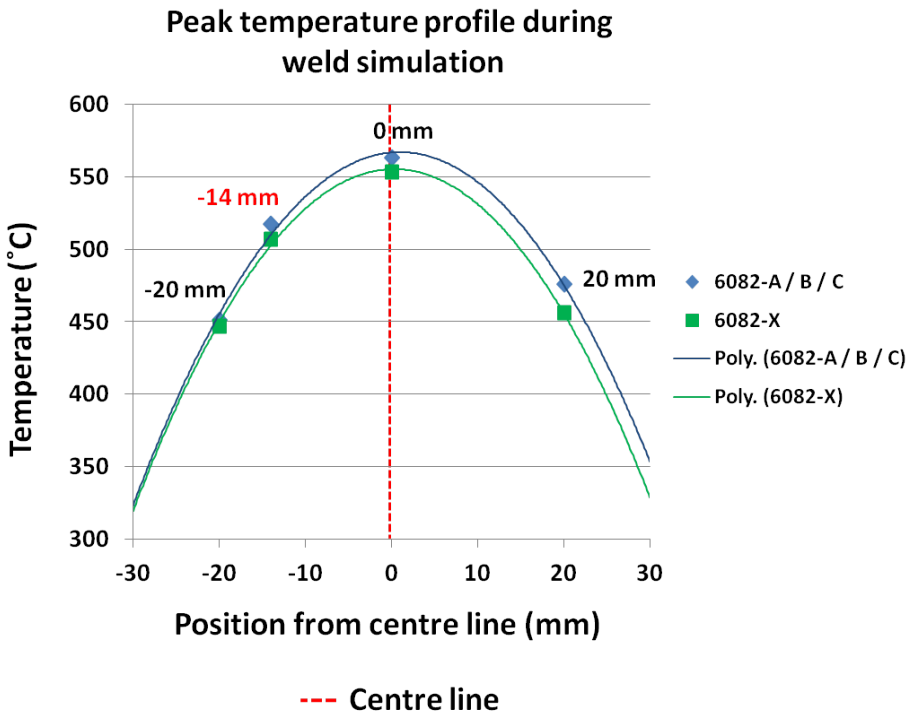

Figure 3.4.: *Peak temperature profile for the specimens subjected to weld simulation. Note the asymmetry of the profile due to dissimilarities in the cooling capability of the two cooling jaws causing uneven extraction of heat. During weld simulation a thermocouple was placed at position -14 mm from the centre line.*

Moreover, as can be seen from figure 3.4, the temperature gradient was found to be slightly more shallow for alloy 6082-X as compared to alloys 6082-A, 6082-B and 6082-C. This observation is probably linked to the thickness of alloy 6082-X being 3 mm, as opposed to 2 mm for the three other alloys. Also, alloy 6082-X was cut perpendicular to the direction of extrusion in contrast to the three other alloys which were cut parallel to the direction of extrusion.

Figure 3.5 shows the temperature profile during weld simulation of alloy 6082-A at a distance of -14 mm from the centre line (i.e. the heat affected zone) corresponding to the position of the thermocouple. As all the profiles proved almost identical, except small variations in peak temperatures, only one of the profiles are presented in this section. All temperature profiles can be found in appendix C. The observed peak temperatures were just below 520 °C for most of the samples. Furthermore, as the position of the thermocouple was -14 mm from the centre line, a higher peak temperature is expected at the centre line as shown in figure 3.4.

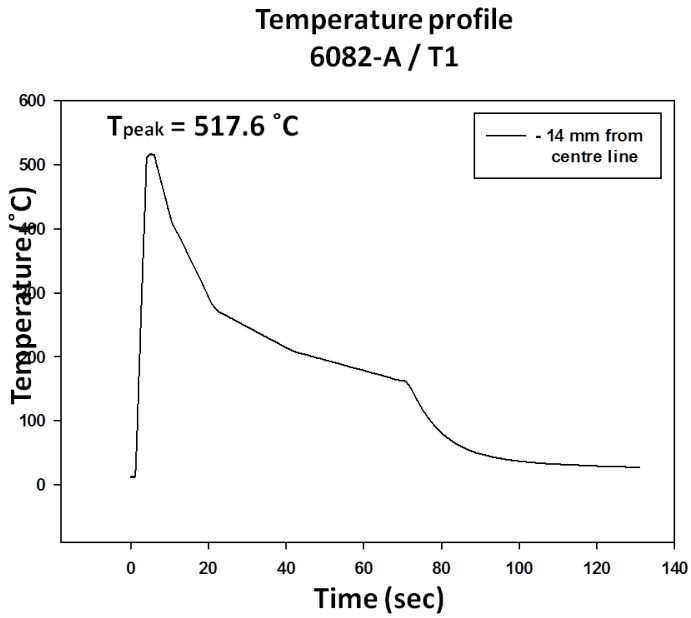

Figure 3.5.: *Temperature profile during weld simulation of alloy 6082-A from T1 starting temper. Note the position of the profile being located -14 mm from the centre line (i.e. in the heat affected zone).*

Table 3.4 gives the peak temperature at position of -14 mm from the centre line. As can be seen from the table, the peak temperature for alloy 6082-X was found to be slightly lower than for alloys 6082-A, 6082-B and 6082-C as already mentioned and shown in figure 3.4.

Table 3.4.: *Peak temperatures at position of -14 mm from centre line during weld simulation. Temper refers to the initial temper condition prior to weld simulation.*

Alloy	Temper	$T_{peak}^{-14\ mm}$ (°C)	Thickness (mm)
6082-X	T1	506.9	3
6082-X	T6	513.5	3
6082-A	T1	517.6	2
6082-B	T1	517.0	2
6082-C	T1	517.0	2

3.5. Post weld heat treatment (PWHT)

Post weld heat treatment was performed on samples subjected to weld simulation in addition to profiles welded by FSW. The heat treatment procedure was similar as to the ageing step (section 3.2.3), and was done by the use of air circulations furnaces at SINTEF Materials and Chemistry, Trondheim. The profiles were heated to 185 $^{\circ}\mathrm{C}$ by a heating rate of 200 $^{\circ}\mathrm{C}$ / h and held at this temperature for 5 hours, before being air cooled to room temperature.

3.6. Microstructure characterisation

Microstructure analysis was performed both in optical microscope and scanning electron microscope (SEM). Both analysis methods followed the same preparation method as described in section 3.6.1. Finally, hardness measurements across the welded section were done on all alloys.

3.6.1. Sample preparation

Samples were prepared by a series of steps. First, samples were cut to approximately 30x40 mm sections, by the use of a water cooled Discotom cutting tool, followed by cold mounting in a ClaroCit resin. The mounted samples were then ground by the use of water proof SiC grinding papers with increasing fineness. Grinding papers used were in accordance with FEPA (Federation of European Abrasive Products) "P" Standard 43-GB [53]. Papers used were P500, P800, P1000, P2400 and P4000 presented in chronological order. During grinding, water was used as lubricant.

Grinding was followed by polishing of the samples by the use of 3-1 μm polishing disks, with DiaPro Mol and OP-S suspensions respectively.

In between each grinding and polishing step, all samples were rinsed in soap water and ethanol. Moreover, for both grinding and polishing, a sample holder and a Struers modular rotating preparation systems was used.

3.6.2. Optical microscope

Analysis in optical microscope was done by the use of a Leica MeF4 optical microscope and a Jenoptik Laser Optik System camera type ProgRes C10 plus. The location of the sections that have been examined in optical microscope after corrosion testing is shown in figure 3.6. It should be noted that alloy 6082-X were examined perpendicular to the direction of extrusion, whereas alloys 6082-A, 6082-B and 6082-C were studied parallel to the direction of extrusion

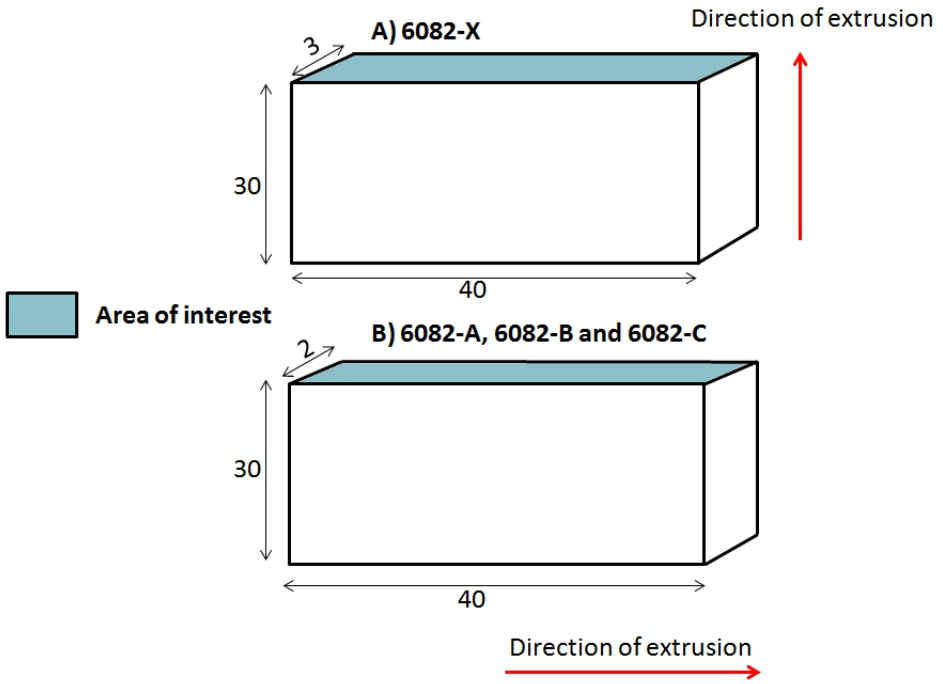

Figure 3.6.: *Location of the sections that have been examined in optical microscope after corrosion testing.* ***A)*** *Alloy 6082-X and* ***B)*** *alloys 6082-A, 6082-B and 6082-C.*

3.6.3. Anodising

Anodising was performed on selected samples in order to examine the grain orientation and moreover the extent of the recrystallized layer after extrusion. The process involved immersion of selected samples either in an electrolyte containing 2% HF, 2% HBF_4, 48 % ethanol and 48 % H_2O by volume, or an electrolyte containing 5% HBF_4 and 95 % H_2O by volume. Both electrolytes produced similar results. The potential and current was set to 20 V and 1 A respectively. Moreover, the required immersion time was found to vary for the individual samples, however a holding time of approximately 90 seconds was found to provide satisfactory results for most variants. Finally, all samples were immediately washed in water and ethanol after immersion and then air dried.

3.6.4. Hardness measurements

Vickers hardness (HV) measurements were taken on all samples prior to any corrosion testing. For the samples that were subjected to weld simulation and FSW, hardness measurements were made by a Matsuzawa DVK-1S hardness tester and the applied load and loading time were 5 kg and 15 seconds respectively. For samples that were subjected to

MIG welding, a Struers Duramin-A2500 hardness tester was used with the applied load and loading time being 1 kg and 30 seconds respectively.

3.6.5. Grain boundary microstructure

Grain boundary precipitates were analysed in a Zeiss Supra 55 VP Low Vacuum Field Emission Scanning Electron Microscope (LV-FESEM) with main operating parameters presented in table 3.5. In order to identify the various phases possibly being responsible for localized corrosion, energy dispersive spectroscopy (EDS) analyses were carried out on selected particles.

Table 3.5.: *Operating parameters during particle analysis in LV FESEM.*

Parameter	Value
Detectors	Backscatter (AsB), secondary (SE2)
Acc. voltage	10-20 kV
Working distance	8-9 mm
Current	103 μA
Aperture radius	120 μm

Moreover, in order to minimize selective dissolution of Mg during sample preparation, samples were occasionally prepared without water nor suspension liquids. Instead, ethanol and 1-3 μm diamond sprays were used. In this way, Mg-rich phases could more easily be observed during EDS analysis.

3.7. Intergranular corrosion test

When testing for IGC an accelerated corrosion test adapted from the British standard BS 11846 method B was used [54]. Following this procedure the samples were first rinsed in acetone and ethanol, followed by alkaline etching in a 7.5 % NaOH solution at 55-60 °C for 3-4 minutes. The samples were then immersed in 65 % nitric acid (HNO_3) for 2 minutes followed by rinsing in water. The accelerated test itself consisted of immersion of the samples in an aqueous solution containing 1 vol% 10 M HCl and 3 wt% NaCl for 24 hours at ambient temperature and pressure, which resulted in a pH of approximately 1.0. After the corrosion test, the sample were immersed in the nitric acid solution once again followed by rinsing in water. In order to measure any weight loss due to corrosion, the samples were weighed both before and after the IGC test.

An overview of the samples that were tested for IGC is shown in table 3.6. Moreover, the experimental set-up for the IGC test is shown in figure 3.7 below. Alloys were separated during immersion thus preventing metallic contact of the samples. Also, to maintain the aggressive nature of the electrolyte throughout the test, all beakers were filled with at least

Table 3.6.: *Overview of samples tested for IGC. Temper refers to the initial temper condition prior to any thermal cycle. X = IGC tested, WS = Weld simulated, PWHT = Post weld heat treatment, MIG = Metal inert gas welded, FSW = Friction stir welded.*

Alloy	Temper	WS	WS +PWHT	MIG	FSW	FSW +PWHT
6082-X	*T1*	x	x	x	-	-
	T6	-	-	x	x	x
6082-A	*T1*	x	x	-	-	-
6082-B	*T1*	x	x	-	-	-
6082-C	*T1*	x	x	-	-	-

2 litres of electrolyte. Finally, pH measurements were made to ensure that the aggressive nature of the electrolyte was maintained.

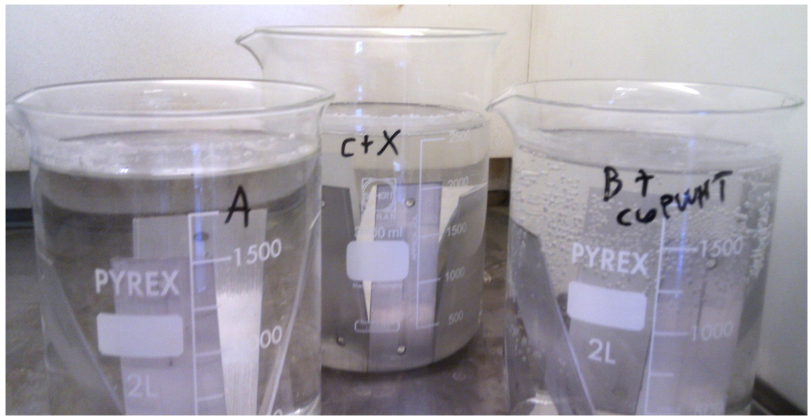

Figure 3.7.: *Experimental set-up for the IGC test of weld simulated samples as well as samples subjected to FSW and MIG welding*

3.8. SWAAT test

Cyclic Acidified Synthetic Sea Water (Fog) Testing (SWAAT) of weld simulated samples, as well as samples subjected to FSW and MIG welding, was performed at Sør-Trøndelag University College (HiST) by Ane Thorvaldsen [55]. Moreover, SWAAT testing was originally planned to be performed on samples from T6 starting tempers only. However, due to improper heat treatment of as-recievied alloys, as discussed in section 3.2.3, alloys 6082-

A, 6082-B and 6082-C where tested from a T1 starting temper. Alloy 6082-X, on the other hand, displayed expected hardness values and was tested from a T6 starting temper.

SWAAT testing followed ASTM standard G85 - 11 (Annex A3), which is a standard practice for acidified synthetic sea water (fog) testing [56]. Moreover, the electrolyte was prepared as described in ASTM standard D1141-98 [57]. Following this standard, two different stock salt solutions were prepared as shown in table 3.7 below.

Table 3.7.: *Composition of stock salt solutions prepared for the SWAAT test according to ASTM standard D1141-98 [57].*

Stock no.	Salt	Amount(g)
1	$MgCl_2 \cdot 6H_2O$	2778.0
	$CaCl_2$	289.5
	$SrCl_2 \cdot 6H_2O$	10.5
2	KCl	347.5
	$NaHCO_3$	100.5
	KBr	50.0
	H_3BO_3	13.5
	NaF	1.5

Stock solution 1 and 2 was prepared by mixing the listed salts and amounts with 5 litres of deionized water. Moreover, the beaker with solutions were immersed in a heated salt bath to ensure dissolution of the salts. Moreover, the SWAAT electrolyte itself was prepared by mixing 500 ml of stock solution 1 with 250 ml of stock solution 2 in a 25 litre container. Thereafter, 613.35 g $NaCl$ and 102.35 g Na_2SO_4 were added to the solution. The volume of the mixture was increased to 24 litres by adding deionized water. Moreover, the pH was adjusted to 2.8-3.0 by adding 180 ml of water free acetic acid. The total volume of the mixture was then increased to 25 litres by further additions of deionized water. Finally, two portions of the above-mentioned solution à 50 litres were added to the SWAAT chamber, resulting in a total electrolyte volume of 100 litres.

Also according to ASTM standard G85 - 11, the fog rate should be in the range of 1.0 to 2.0 ml/h per 80 cm^2 of horizontal collection area [56]. In order to ensure that these requirements were met, a 24 hour spray test were performed and the fog rate was measured to 1.7375 mL/h, which is acceptable. Finally, in order to ensure consistent supply of electrolyte to the SWAAT chamber, the salt concentration was measured on a daily basis. Also, pH measurements were made regularly. A complete inspection form during SWAAT testing of samples is presented in appendix A.

Furthermore, the duration of the test was set to 25 days for samples subjected to MIG welding and weld simulation. However, due to delays during friction welding of alloy 6082-X, FSW variants were only subjected to SWAAT testing for 15 days. An overview of the SWAAT tested samples is given in table 3.8. Finally, macro images of alloy 6082-X / T6 during SWAAT testing are shown in figure 3.8.

Table 3.8.: *Overview of SWAAT-tested samples. Temper refers to the initial temper condition prior to any thermal cycle. X = SWAAT tested, WS = Weld simulated, PWHT = Post weld heat treatment, MIG = Metal inert gas welded, FSW = Friction stir welded.*

Alloy	Temper	WS	WS +PWHT	MIG	FSW	FSW +PWHT
6082-X	*T6*	-	x	x	-	x
6082-A	*T1*	-	x	-	-	-
6082-B	*T1*	-	x	-	-	-
6082-C	*T1*	-	x	-	-	-

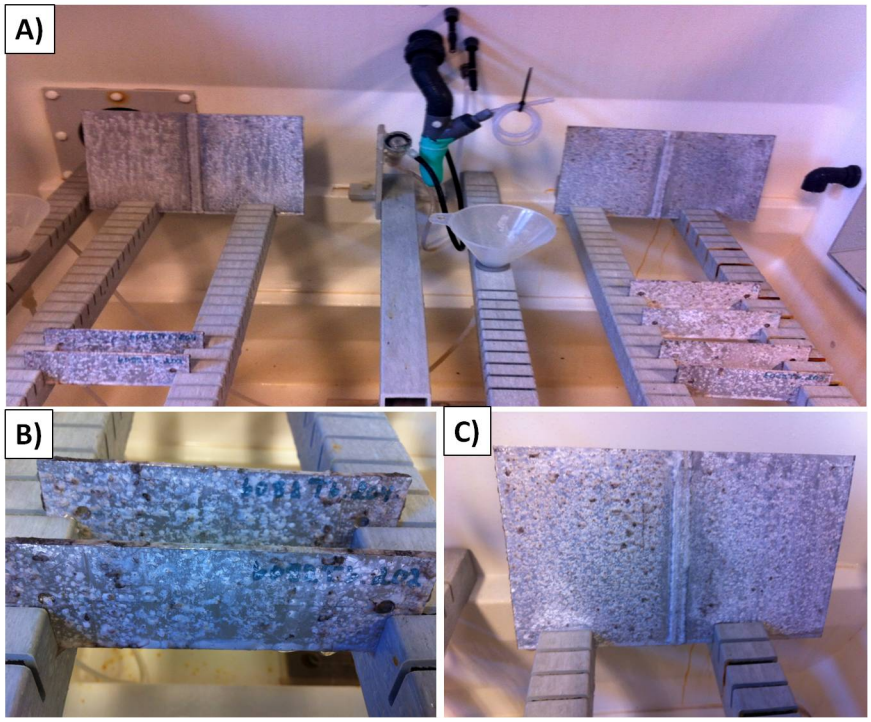

Figure 3.8.: *Experimental set-up for the SWAAT test of weld simulated samples as well as samples subjected to FSW and MIG welding.* ***A)*** *Overview of the chamber,* ***B)*** *Weld simulated 6082-X / T6 and* ***C)*** *MIG welded 6082-X / T6.*

3.8.1. Pit measurements

Measurements of pits after SWAAT testing were done on those visible by the naked eye. Moreover, pit density was measured on a macro scale, whereas pit depth and diameter was measured by the use of optical microscope. Analysis were done on sections measuring 50x40 mm according to figure 3.9. It should be noted that measurements were taken only at one side of the centre line. All measurements were done in the extrusion plane.

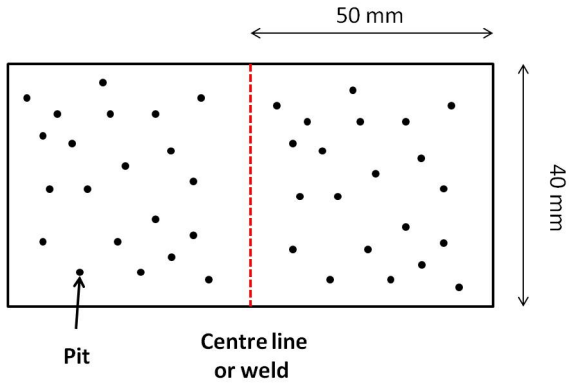

Figure 3.9.: *Figure illustrating sections measuring 50x40 mm were pit analysis were done. Measurements were taken in the extrusion plane at one side of the centre line/ weld only.*

3.9. Potential measurements

In order to observe the corrosion behaviour as a function of distance from the fusion zone, the open circuit potential (OCP) was measured for MIG welded 6082-X / T6. In this experiment four different regions were tested including the fusion zone, the region close to the fusion line, the heat affected zone and the base material. The location of the four different sections that were tested are shown in figure 3.10 numbered 1-4. In all cases the exposed area was fixed at 30 mm^2 and any redundant area was coated. Due to the unstable nature of the OCP for most aluminium alloys, measurements were taken for at least 12 hours in order to obtain steady-state and stable measurements.

The experimental set-up consisted of a potentiostat with a saturated calomel reference electrode and a platinum counter electrode. The electrolyte used was equivalent to the one used during the SWAAT testing as described in section 3.8. Prior to any measurements the samples were rinsed in acetone and surfaces were lightly ground.

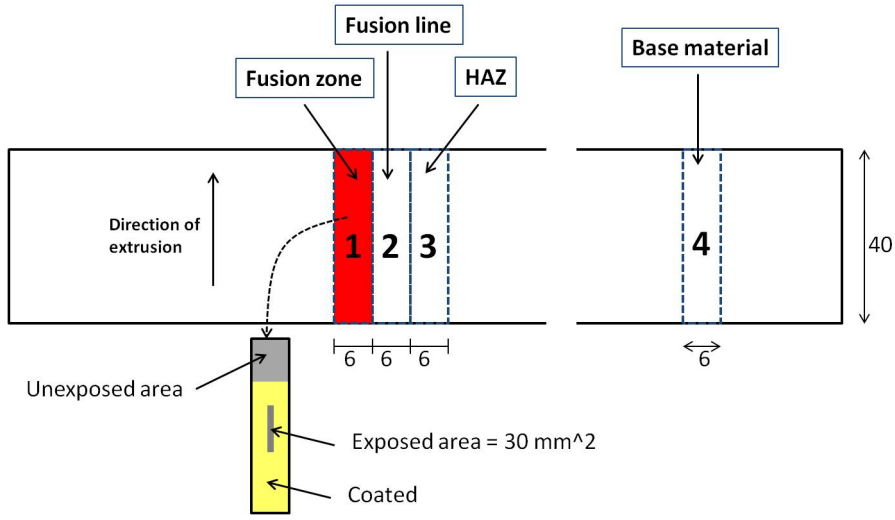

Figure 3.10.: *Location of samples where potential measurements were done. All measurements presented in the figure are given in millimetres.*

3.10. Electrical conductivity measurements

In order to determine the amount of alloying elements in solid solution, and hence the susceptibility to pitting corrosion, electrical conductivity measurements were made in the weld, the HAZ and the base metal. The electrical conductivities were determined by applying a Foerster Sigmascope 2.069. The instrument was calibrated before any readings were taken, and the frequency was set to 120 kHz. The diameter of the probe used was measured to be 7 mm. Samples were ground and polished prior to the measurements in order to a obtain a flat surface profile.

4 Results

4.1. Material characterization

Prior to corrosion testing a material characterization of the as-received test materials was performed. The characterization included macro and micro analysis, as well as examinations of intermetallic phases and electrical conductivity measurements and hardness measurements. Such analyses were done both for the welded section, the heat affected zone and the base material.

4.1.1. Weld seam

Figure 4.1 shows the weld seam of alloy 6082-X welded by both FSW (A,B) and MIG welding (C,D) techniques. As seen by the figure, the weld seam for the MIG welded samples were covered by a dark oxide layer, possibly MgO. However, prior to corrosion testing this layer was removed by alkaline etching (section 3.7). Also, for the samples welded by FSW the characteristic "keyhole" could easily be observed which represents the point of initiation for the FSW process.

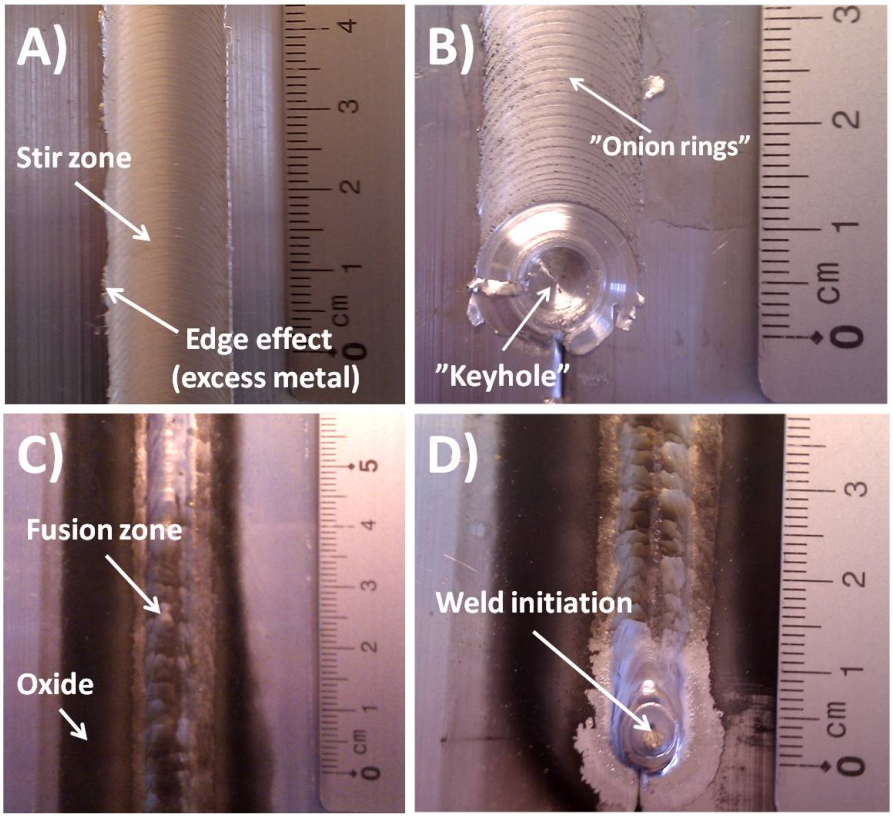

Figure 4.1.: *Macro images of weld seams after FSW and MIG welding of alloy 6082-X / T6 prior to corrosion testing. A) weld seam after FSW, B) weld initiation point for the FSW process often referred to as the "keyhole", C) weld seam after MIG welding (note the pronounced dark oxide layer) and D) weld initiation point after MIG welding.*

4.1.2. Microstructures

Optical micrographs and LV-FESEM micrographs of alloys 6082-X, 6082-A, 6082-B and 6082-C are shown in figure 4.2 through 4.8. What should be noted from the optical micrographs is the extent of the recrystallized layer being around 200 μm in 6082-X, and almost non-existing in alloys 6082-A, 6082-B and 6082-C. As seen in section 2.5.4, the extent of the recrystallized layer may play a crucial role when the susceptibility towards IGC is to be determined.

Alloy 6082-X

The microstructure of the base material in alloy 6082-X both parallel and perpendicular to the direction of extrusion are presented in figure 4.2. The microstructure consists of a thin recrystallized layer with a thickness of approximately 200 μm, and a bulk region with a fibrous microstructure due to extrusion. Moreover, figure 4.3 presents micrographs of the

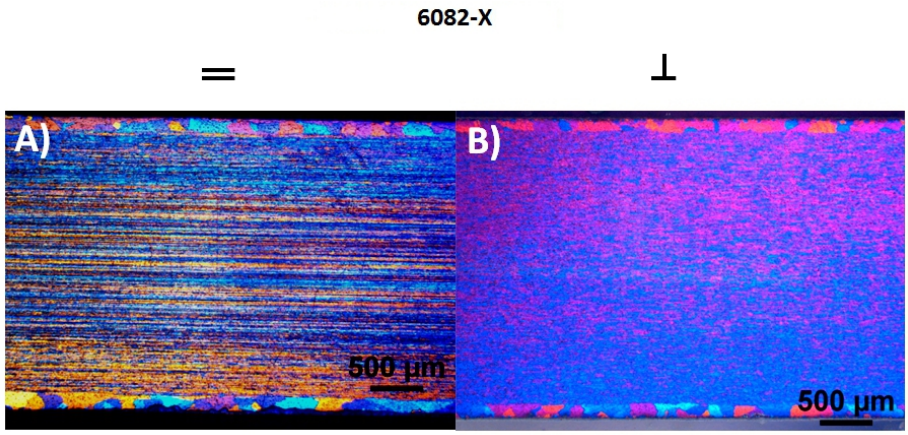

Figure 4.2.: *Micrographs of the base metal in alloy 6082-X parallel to the direction of extrusion (A) and perpendicular to the direction of extrusion (B).*

welded section in alloy 6082-X after FSW (A,B) and MIG welding (C,D). Note the as-cast structure in the weld metal for the MIG welded alloy and the thermo-mechanically affected zone (TMAZ) for the FSW sample. Moreover, the recrystallized layer in the heat affected zone appears to vary depending on the welding technique. From the figure the layer is observed to be thicker for the samples welded by FSW as compared to MIG welding. In fact, examinations reveal that the extent of the recrystallized layer for the samples welded by FSW is approximately 250 μm, as opposed to 140 μm for the MIG welded samples.

Figure 4.4 shows LV-FESEM micrographs of alloy 6082-X across the welded section (A,B) and the base material (C,D). In the welded section, the characteristic as-cast microstructure is observed, whereas a combination of equiaxed and elongated grains is observed for the base metal. Figure 4.4B shows the boundary region between the fusion line and the heat affected zone. In the heat affected zone close to the fusion line rather large equiaxed grains (10 μm) are observed, as opposed to the smaller elongated grains in the base metal. Finally, figure 4.5 shows LV-FESEM micrographs of alloy 6082-X across the friction stir welded section. As can be seen from the figure, no significant variation in the microstructure can be seen. However, the grain structure in the TMAZ appears more equiaxed in nature, as compared to the more elongated grains in the base metal.

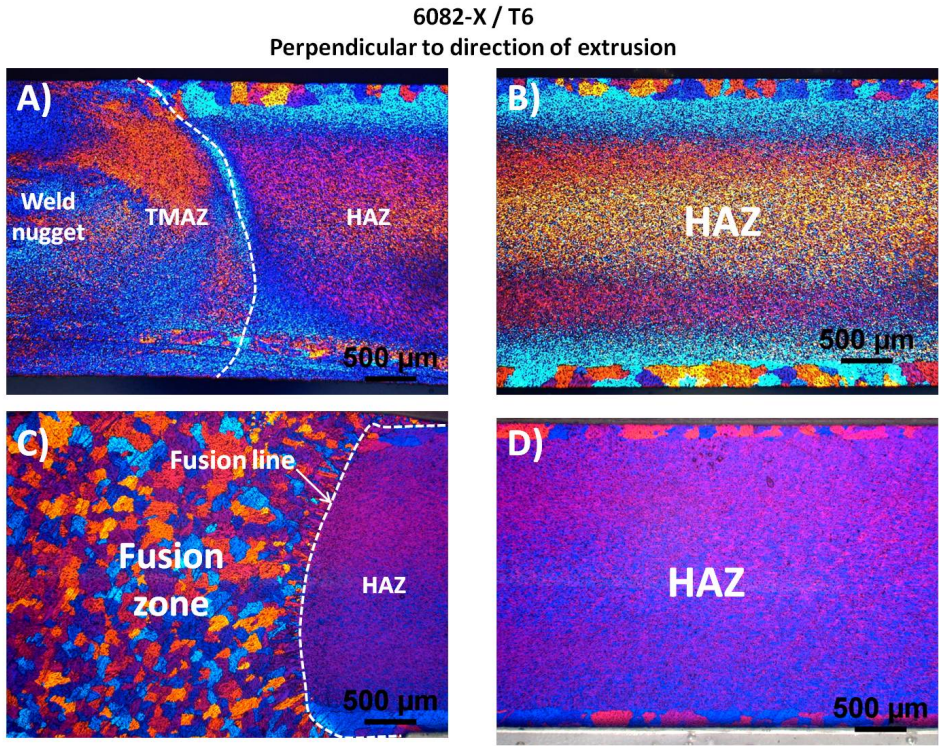

Figure 4.3.: *Micrographs of the welded section in alloy 6082-X after FSW (top) and MIG welding (bottom) from T6 starting tempers.* ***After FSW****:* ***A)*** *Weld nugget, thermomechanically affected zone (TMAZ) and heat affected zone (HAZ) and* ***B)*** *HAZ.* ***After MIG****:* ***C)*** *Fusion zone and* ***D)*** *HAZ. All micrographs are taken perpendicular to the direction of extrusion.*

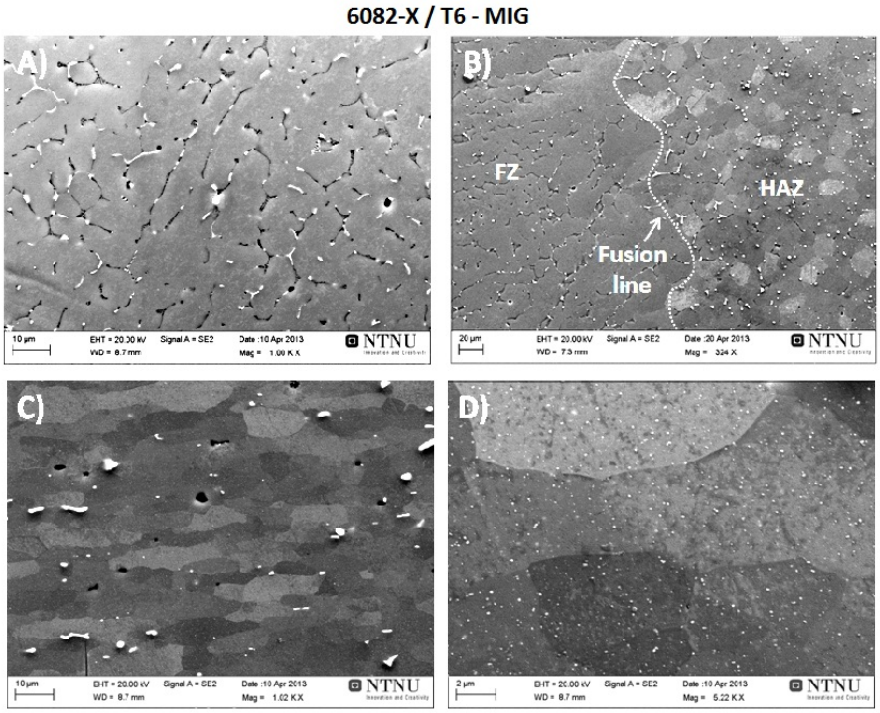

Figure 4.4.: *LV-FESEM secondary electron micrographs of alloy 6082-X across the welded section and the base material after MIG welding.* ***A)*** *Weld metal,* ***B)*** *Fusion zone, fusion line, HAZ* ***C)*** *and* ***D)*** *base material. All micrographs are cross sectional images perpendicular to the direction of extrusion.*

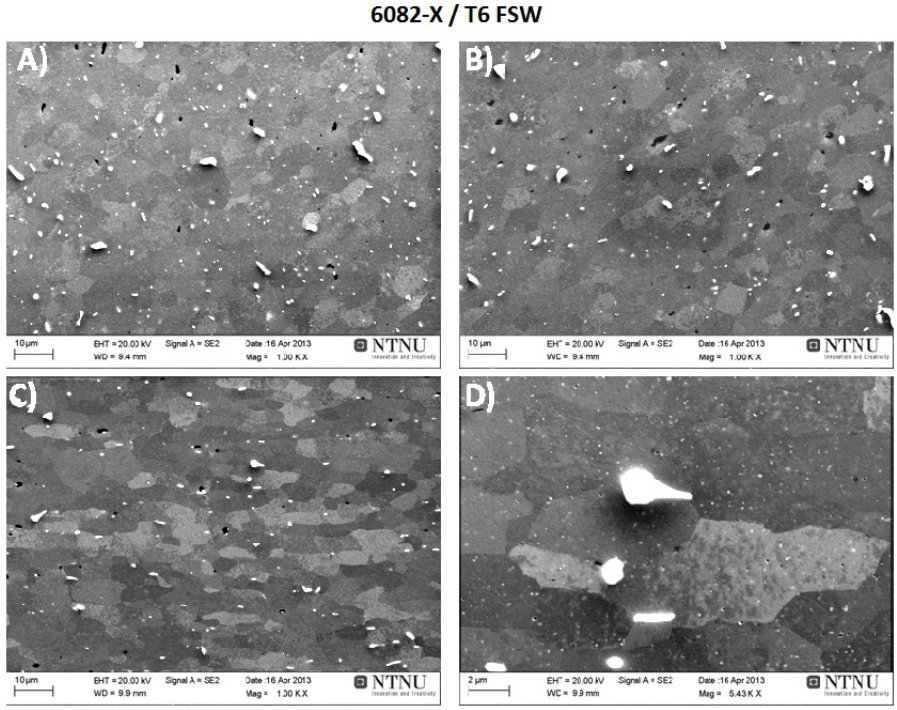

Figure 4.5.: *LV-FESEM secondary electron micrographs of alloy 6082-X across the welded section and the base material after FSW.* ***A)*** *Weld nugget,* ***B)*** *HAZ,* ***C)*** *and* ***D)*** *base material. All micrographs are cross sectional images perpendicular to the direction of extrusion.*

Alloy 6082-A

Optical micrographs of the base material of alloy 6082-A both parallel and perpendicular to the direction of extrusion can be seen in figure 4.6A and B. The material is characterized a by completely deformed bulk region displaying a fibrous microstructure, and no recrystallized layer can be observed. Finally, LV-FESEM micrographs of the alloy are shown in figures 4.6C and D where small equiaxed grains (sub grains) may be observed, in addition to a high density of intermetallic particles.

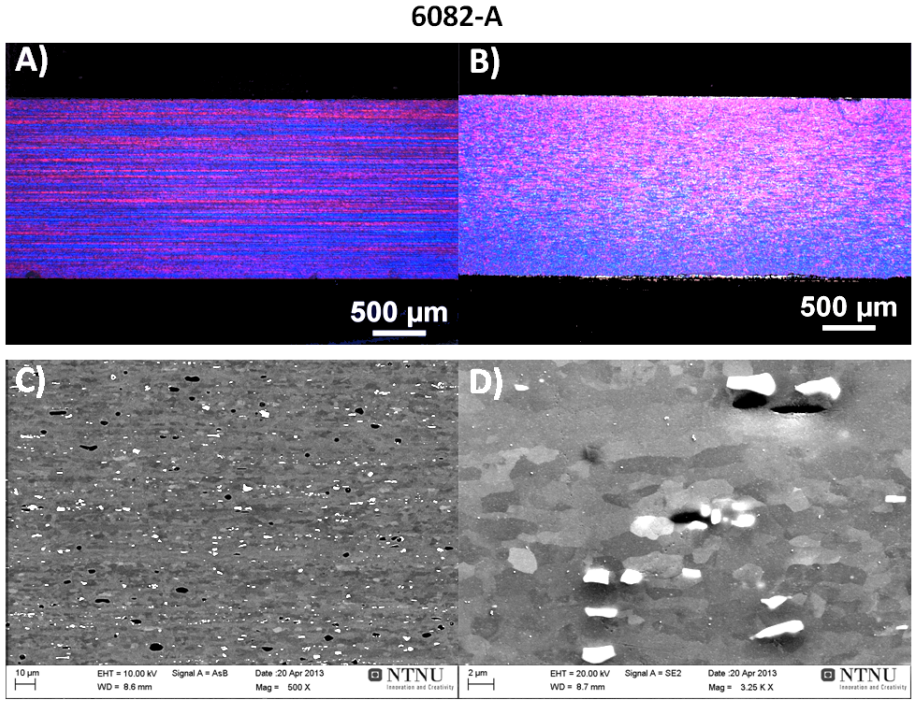

Figure 4.6.: ***Upper****: Micrographs of the base metal in alloy 6082-A parallel to the direction of extrusion (**A**) and perpendicular to the direction of extrusion (**B**). **Lower**: LV-FESEM micrographs of the as-extruded microstructure parallel to direction of extrusion (**C,D**).*

Alloy 6082-B

Figure 4.7A and B shows optical micrographs of the base material of alloy 6082-B both parallel and perpendicular to the direction of extrusion. The microstructrue is found to prove very similar to the one observed in alloy 6082-A and the recrystallized layer is completely absent. However, the fibrous microstructure is perhaps not as easily observed as in the case of alloys 6082-A and 6082-X. LV-FESEM micrographs of the alloy are shown in figure 4.6C and D. As for alloy 6082-A, small equiaxed grains (sub grains) may be seen in addition to a high density of intermetallic particles.

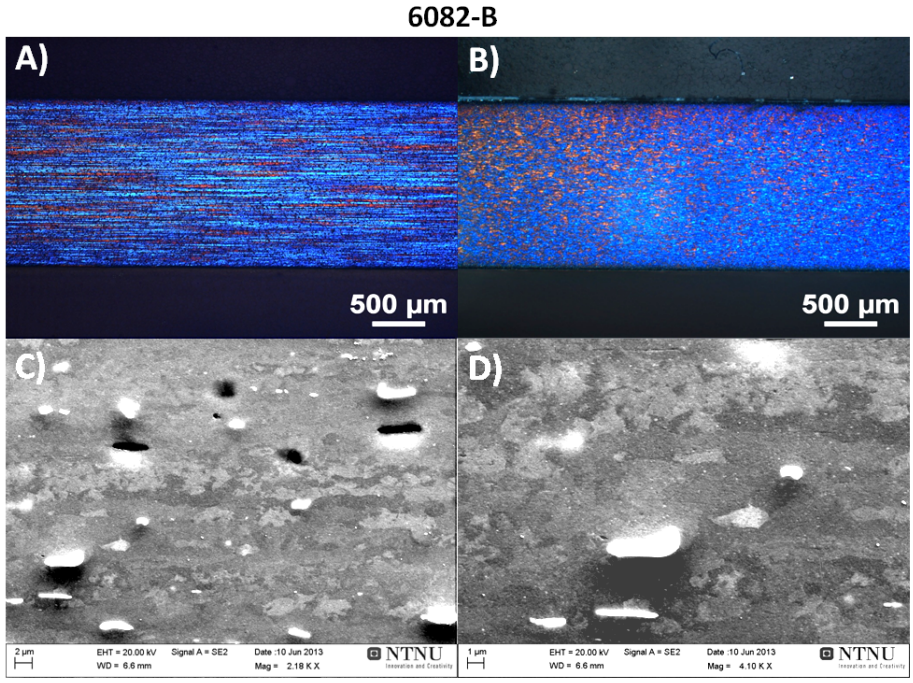

Figure 4.7.: ***Upper****: Micrographs of the base metal in alloy 6082-B parallel to the direction of extrusion (A) and perpendicular to the direction of extrusion (B).* ***Lower****: LV-FESEM secondary electron micrographs of the as-extruded microstructure parallel to direction of extrusion (**C,D**).*

Alloy 6082-C

Optical micrographs of the base material of alloy 6082-C both parallel and perpendicular to the direction of extrusion can be seen in figure 4.8A and B. However, as for alloys 6082-A and 6082-B no recrystallized layer was observed. Finally, LV-FESEM micrographs of the alloy are shown in figure 4.6C and D. As for alloys 6082-A and 6082-B, small equiaxed grains (sub grains) may be seen in addition to a high density of intermetallic particles

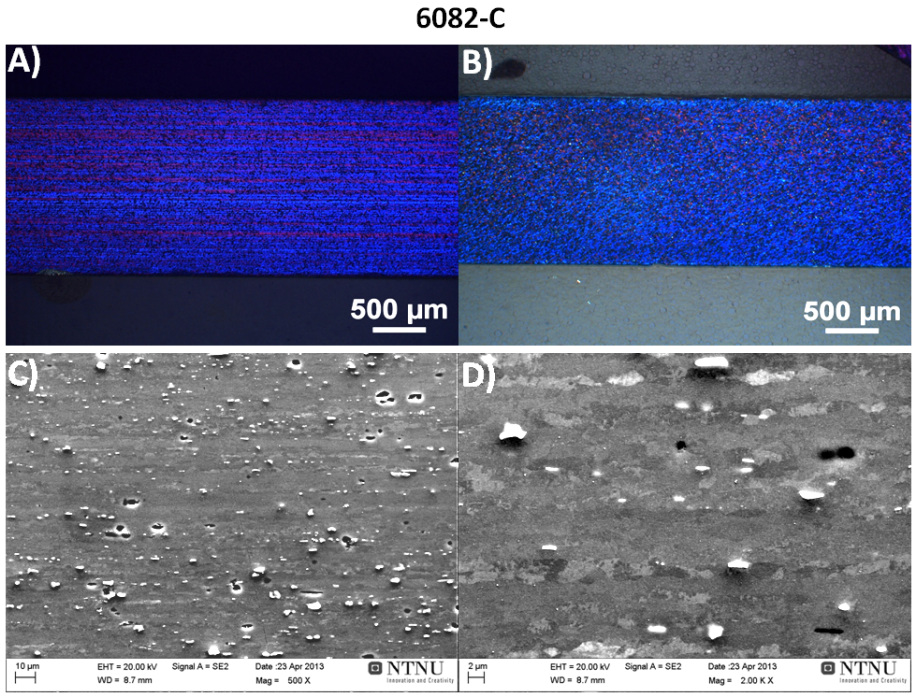

Figure 4.8.: ***Upper****: Micrographs of the base metal in alloy 6082-C parallel to the direction of extrusion (A) and perpendicular to the direction of extrusion (B).* ***Lower****: LV-FESEM secondary electron micrographs of the as-extruded microstructure parallel to direction of extrusion (**C,D**).*

4.2. Hardness profiles

Measured hardness values of the base material for the four alloys considered in this study are presented in table 4.1 below. Alloys 6082-A, 6082-B and 6082-C were also delivered in a T6 temper condition. However, hardness measurements revealed that the desired strength level was not met. In fact, hardness measurements were found to be almost identical to the samples in T1 temper condition. As a result, all received samples of alloy 6082-A, 6082-B and 6082-C are considered to possess a T1 temper condition. This issue is discussed in further detail in section 5.1. Alloy 6082-X, on the other hand, displayed expected hardness values for both temper condition.

Table 4.1.: *Hardness values and the corresponding standard deviation for the base material of the four alloys considered in this study.*

Alloy	Temper	Hardness (HV5)	Standard Deviation
6082-X	T1	78.4	2.5
6082-X	T6	100.5	2.0
6082-A	T1	53.3	0.8
6082-B	T1	54.7	0.4
6082-C	T1	61	1.6

4.2.1. Samples subjected to FSW and MIG welding

Hardness profiles of MIG welded 6082-X in T6 and T1 temper condition are shown in figure 4.9. As can be seen, both temper conditions displayed minimum hardness values of 64 HV in the HAZ. The extent of the HAZ is estimated to be approximately 20 mm and 25 mm for the T6 and T1 temper condition respectively.

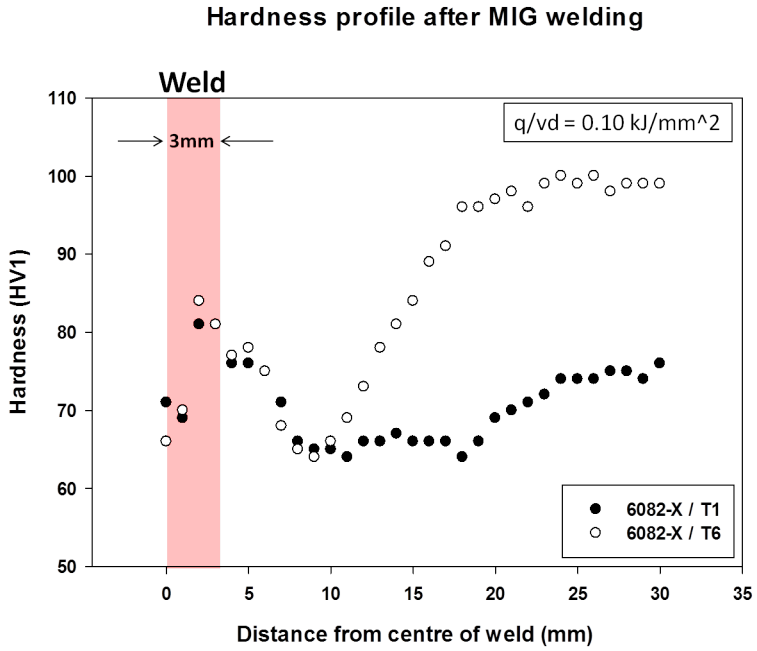

Figure 4.9.: *Hardness profiles across the welded section of MIG welded AA6082-T6 and AA6082-T1. Measurements taken along the plane perpendicular to the direction of extrusion. Heat input (q/vd) was maintained at 0.10* kJ/mm^2.

Hardness profiles of 6082-X subjected to FSW and FSW with subsequent post weld heat treatment (PWHT) from T6 starting tempers are shown in figure 4.10. Prior to PWHT a minimum hardness value of 65 HV was observed in the HAZ for the friction welded alloy. As a result, despite the extent of the HAZ being greatly reduced by the FSW technique, as compared to MIG welding, the minimum strength in the HAZ was not improved. However, PWHT resulted in the minimum strength level in the HAZ being increased to 81 HV for the samples welded by FSW. Post weld heat treatment was not performed on MIG welded samples.

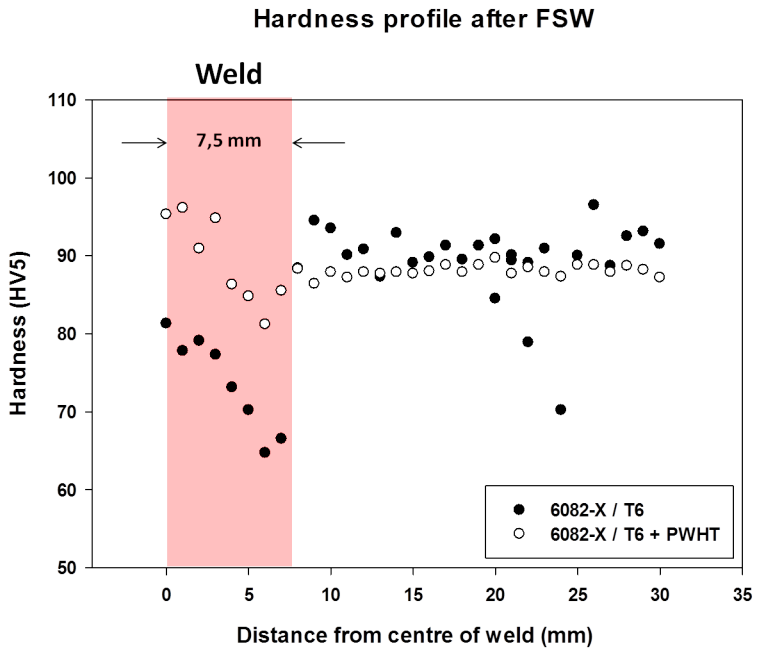

Figure 4.10.: *Hardness profiles of 6082-X subjected to FSW and FSW with subsequent post weld heat treatment (PWHT) from T6 starting tempers. Measurements taken along the plane perpendicular to the direction of extrusion.*

Also, as can be seen from the figure, the hardness in the base metal of the T6-FSW sample is found to be approximately 90 HV, as opposed to 100 HV for the T6-MIG sample. As a result, some overageing has taken place during artificial ageing of the FSW profiles. Moreover, by performing PWHT on the T6-FSW samples the hardness in the base metal was observed to be reduced even further, although the variation was small. Finally, some soft zones may be observed for the T6-FSW variants which may be regions were precipitation of hardening particles has been limited. However, with subsequent PWHT these soft zones are no longer observed as reprecipitation of hardening precipitates has taken place.

4.2.2. Weld simulated samples

Hardness measurements of weld simulated samples are shown in figure 4.11 through 4.15. All measurements were taken in the extrusion plane.

Alloys 6082-A, 6082-B and 6082-C

For the naturally aged (T1) alloys 6082-A, 6082-B and 6082-C, the effect of weld simulation proves beneficial with respect to the observed hardness. This phenomenon is explained by dissolution of the thermally unstable GP-zones and subsequent solution heat treatment close to the centre line, where the temperature has been above approximately 530 °C. Upon cooling precipitation of the hardening β' and β'' particles has taken place, thus increasing the hardness in this area. At distances too far from the centre line, say 30 mm, the peak temperature has not been high enough and no effect of artificial ageing can be observed. Finally, by performing post weld heat treatment (PWHT), the effects from artificial ageing are amplified even more as the hardness profile is shifted to higher hardness values particularly at the centre line. However, at the outer edges, no effect from PWHT is seen. As a result, the susceptibility to artificial ageing far from the centre line is found to be low. Such observations are believed to result from low densities of quenched-in vacancy clusters or solute in the alloy, and the phenomenon is discussed in further detail in section 5.1.

Moreover, the effect of Cu content on the precipitation of β' and β'' is apparent when moving from 6082-A through 6082-C with the Cu concentrations increasing from 0.001 to 0.60 wt% respectively. As can be seen in figure 4.11 through 4.13, the maximum hardness value increases from 62 HV for alloy 6082-A, to 90 HV in the case of alloy 6082-C. Also, the effect of PWHT on the weld simulated samples appears to be strongly related to the Cu concentration. In fact, for alloy 6082-C containing 0.60 wt% Cu, the increase in hardness at the centre line after PWHT is close to 30 HV, whereas no difference in hardness at the centre line can be observed for alloy 6082-A after the same heat treatment.

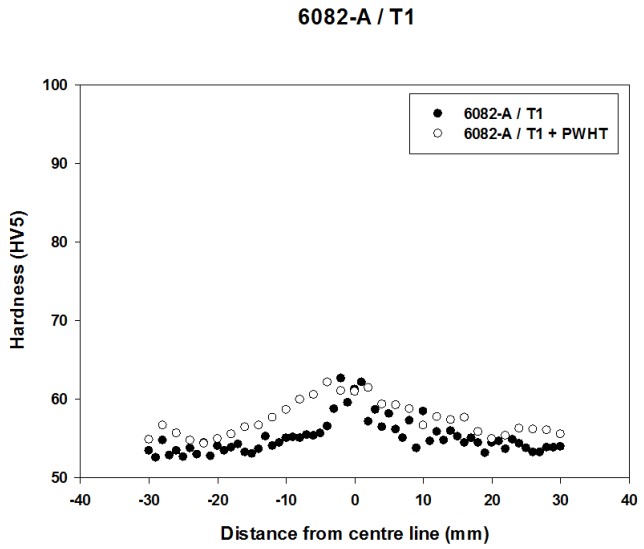

Figure 4.11.: *Hardness profile after weld simulation and post weld heat treatment (PWHT) of alloy 6082-A from T1 starting temper.*

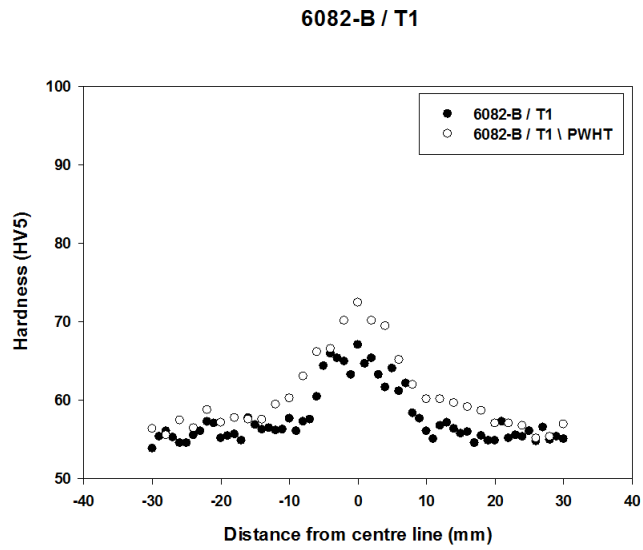

Figure 4.12.: *Hardness profile after weld simulation and post weld heat treatment (PWHT) of alloy 6082-B from T1 starting temper.*

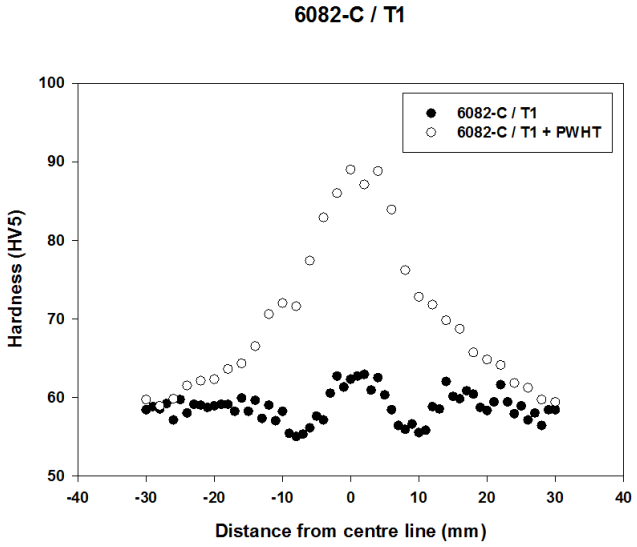

Figure 4.13.: *Hardness profile after weld simulation and post weld heat treatment (PWHT) of alloy 6082-C from T1 starting temper.*

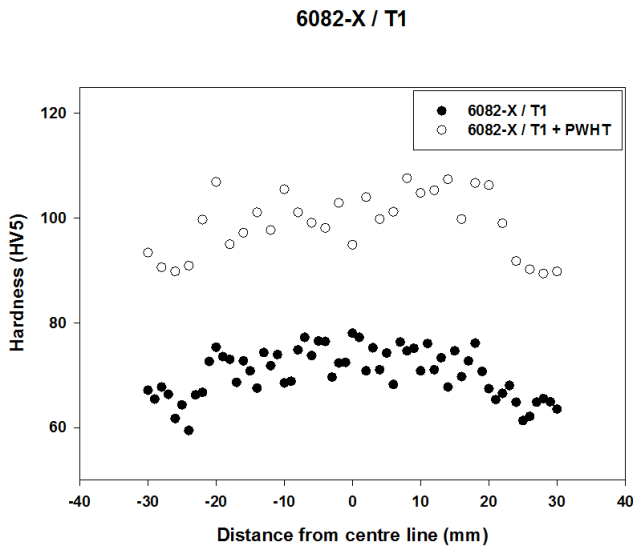

Figure 4.14.: *Hardness profile after weld simulation and post weld heat treatment (PWHT) of alloy 6082-X from T1 starting temper.*

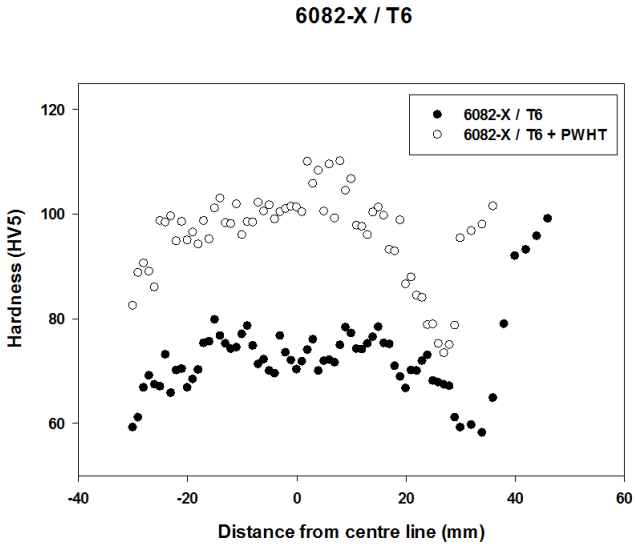

Figure 4.15.: *Hardness profile after weld simulation and post weld heat treatment (PWHT) of alloy 6082-X from T6 starting temper.*

Alloy 6082-X

The hardness profile of alloy 6082-X after weld simulation proves different compared to alloys 6082-A, 6082-B and 6082-C. From figures 4.14 and 4.15 it appears as if the entire length of the sample is affected during weld simulation. As a result, it seems as if alloy 6082-X is more susceptible to artificial ageing as compared to the three other alloys. Finally, a sudden reduction in hardness approximately 30 mm from the centre line was observed in sample 6082-X / T6. These measurements are expected to be related to local overageing of the alloy and hence a reduction in observed hardness. As will be seen in later sections, this region was observed to display increasing susceptibility to pitting corrosion.

4.3. IGC test

Optical micrographs of IGC tested samples are shown in sections 4.3.1 through 4.3.3 for samples subjected to MIG, FSW and weld simulation respectively. In all cases the weld, the heat affected zone and the base material was examined. However, only locations where corrosion attacks were observed are presented.

4.3.1. MIG welded samples

Analysis of MIG welded 6082-X after the accelerated IGC test revealed moderate corrosion of the weld metal, however no corrosion of the heat affected zone nor the base material. Profiles were tested both in naturally aged and artificially aged temper condition.

Welded section

Figure 4.16 shows micrographs of the welded section of alloy 6082-X. As can be seen from the figure, corrosion attacks can be observed in the weld metal for both temper conditions. Closer examinations, shown in figure 4.17, reveal that the corrosion attacks are in fact intergranular corrosion, with maximum depths of 135 μm and 100 μm for the T6 and T1 tempers respectively. However, due to the as-cast microstructure of the fusion zone, the IGC attacks do not form wide networks across the weld. Instead, the propagation appears to be limited to the discontinuous network of second phase particles. As a result, the formation of discontinuous second phase particle networks in the weld metal seems to inhibit the propagation of IGC, thus proving beneficial with regards to corrosion resistance. Finally, as the corrosion attacks were observed solely in the weld metal, no significant effect of temper condition on the corrosion resistance was observed.

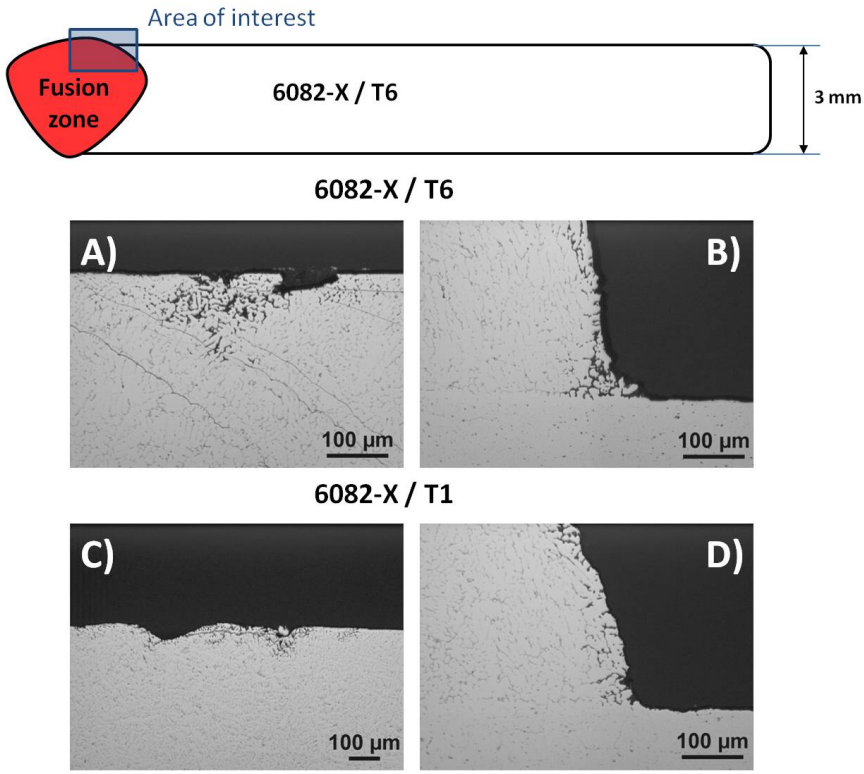

Figure 4.16.: *Corrosion of weld metal in 6082-X / T6 (**A,B**) and 6082-X / T1 (**C,D**). Micrographs taken perpendicular to the direction of extrusion.*

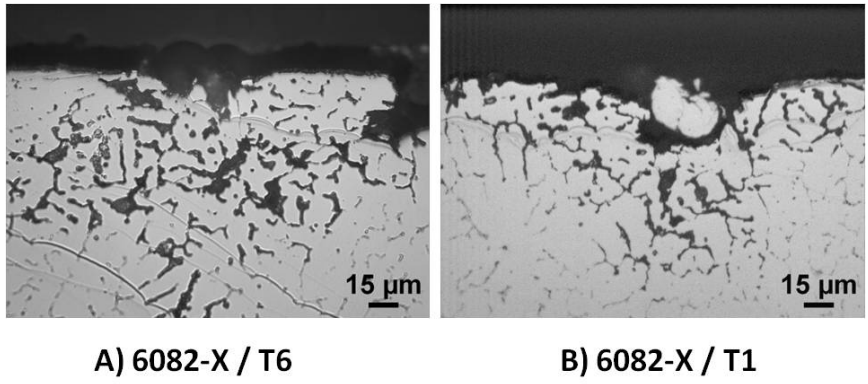

Figure 4.17.: *Intergranular corrosion of weld metal in alloy 6082-X. Micrographs taken perpendicular to the direction of extrusion*

4.3.2. FSW samples

Results from the accelerated IGC test of alloy 6082-X subjected to FSW, and FSW with subsequent PWHT, are shown in figure 4.18. Closer examination of the weld in the latter sample is shown in figure 4.19.

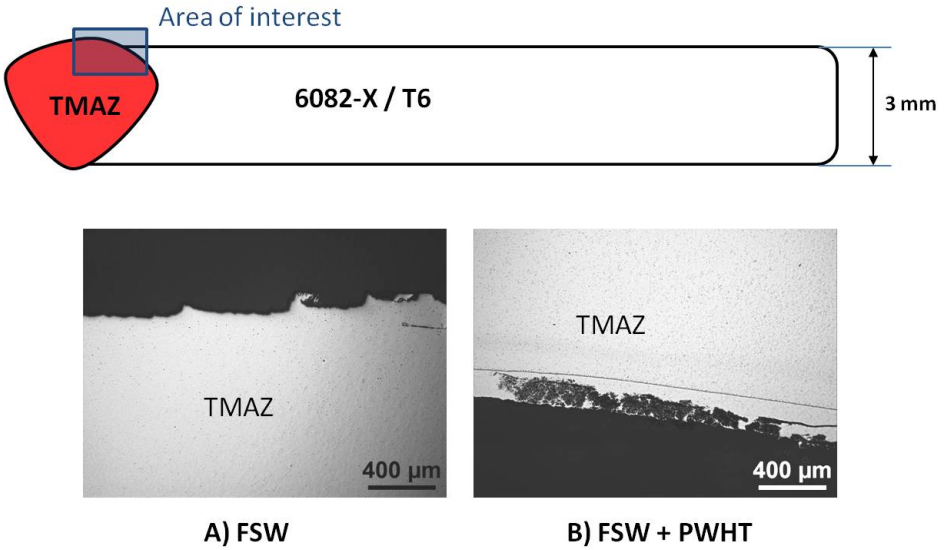

Figure 4.18.: *Micrographs of corroded FSW samples.* ***A)*** *Superficial attacks in the TMAZ.* ***B)*** *Corrosion of recrystallized layer in the TMAZ. Micrographs taken perpendicular to the direction of extrusion.*

Welded section

Micrographs of the welded section revealed pitting corrosion, and possibly IGC, in the recrystallized layer. However, these corrosion attacks were only observed close to the TMAZ. As for the MIG welded samples, no IGC nor pitting corrosion were observed in the HAZ and the base material.

Closer examination of the corroded recrystallized layer in the TMAZ of alloy 6082-X / T6 subjected to FSW and PWHT are shown in figure 4.19. From the figure, it appears as if these corrosion attacks are correlated to the rough surface profile (excess metal) at the edge of the stir zone as seen in figure 4.1A. Moreover, in the TMAZ attacks from pitting corrosion were observed for the same sample (FSW+PWHT) as can be seen in figure 4.20.

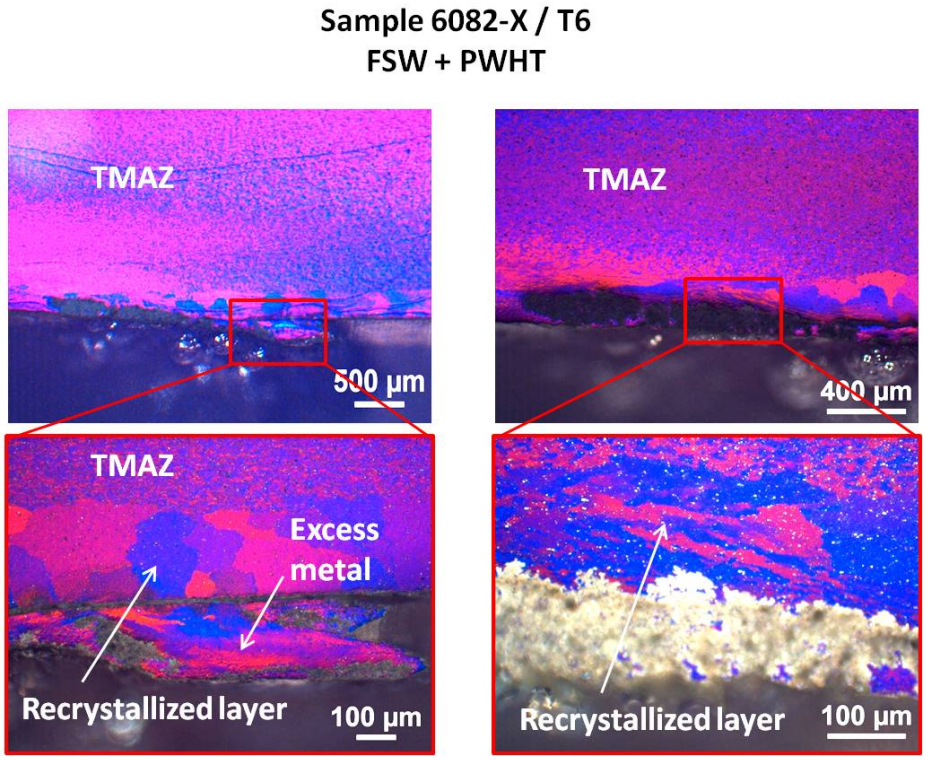

Figure 4.19.: *Pitting corrosion in the recrystallized layer in alloy 6082-X / T6 subjected to FSW and PWHT. Micrographs taken perpendicular to the direction of extrusion.*

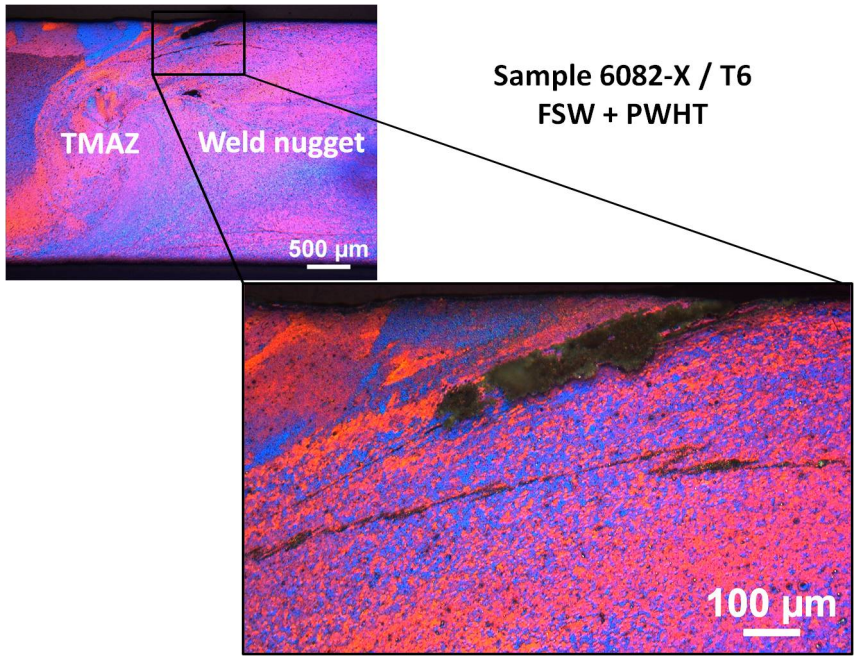

Figure 4.20.: *Pitting corrosion in the TMAZ in alloy 6082-X / T6 subjected to FSW and PWHT. Micrographs taken perpendicular to the direction of extrusion.*

4.3.3. Weld simulated samples

Micrographs of IGC tested samples subjected to weld simulation are shown in figure 4.21, in addition to samples subjected to weld simulation with subsequent PWHT. As can be seen from the figure no attacks from IGC nor pitting corrosion were observed for the Cu lean alloys 6082-A and 6082-X. For alloys 6082-B and 6082-C containing 0.10 and 0.60 wt % Cu respectively, both IGC and pitting corrosion were observed. However, the extent of observed corrosion attacks were small and IGC seemed to be limited to sub grains. Finally, no significant effect from PWHT can be observed.

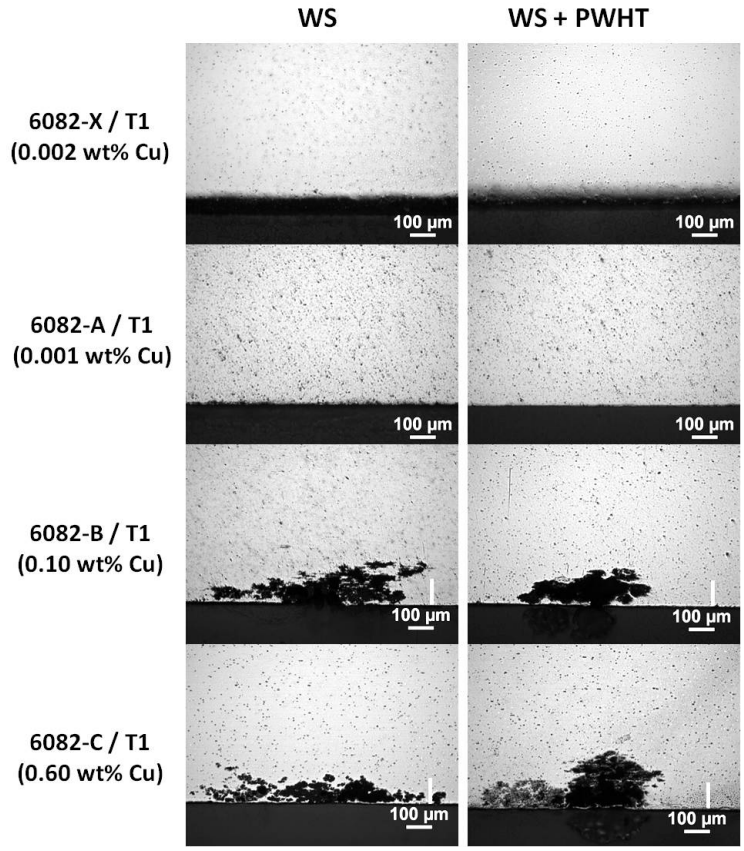

Figure 4.21.: *Micrographs of the corroded samples subjected to weld simulation (WS) and post weld heat treatment (PWHT). Micrographs taken perpendicular to the direction of extrusion for alloy 6082-X and parallel to the direction of extrusion for alloys 6082-A, 6082-B and 6082-C.*

Table 4.2 gives an overview of the observed corrosion modes as well as the location of the corrosion attacks. As can be seen, the corrosion frequency was found to increase with increasing Cu content.

Table 4.2.: *Overview of observed corrosion modes including location of pitting and IGC attacks as a function of distance from centre line for weld simulated samples.*

Alloy	Temper	PWHT	Corrosion Mode [a]	Distance from centre line (mm)
6082-X	T1	Yes	Uniform	-
6082-X	T1	No	Uniform	-
6082-A	T1	Yes	Uniform	-
6082-A	T1	No	Uniform	-
6082-B	T1	Yes	Pitting, IGC	15,20,20,45,60
6082-B	T1	No	Pitting, IGC	40,45,50,60
6082-C	T1	Yes	Pitting, IGC	5,20,35,40,45,50,52,55,60
6082-C	T1	No	Pitting, IGC	30,35,40,45,50,52,55,60

[a] All IGC attacks were observed to propagate along sub grains.

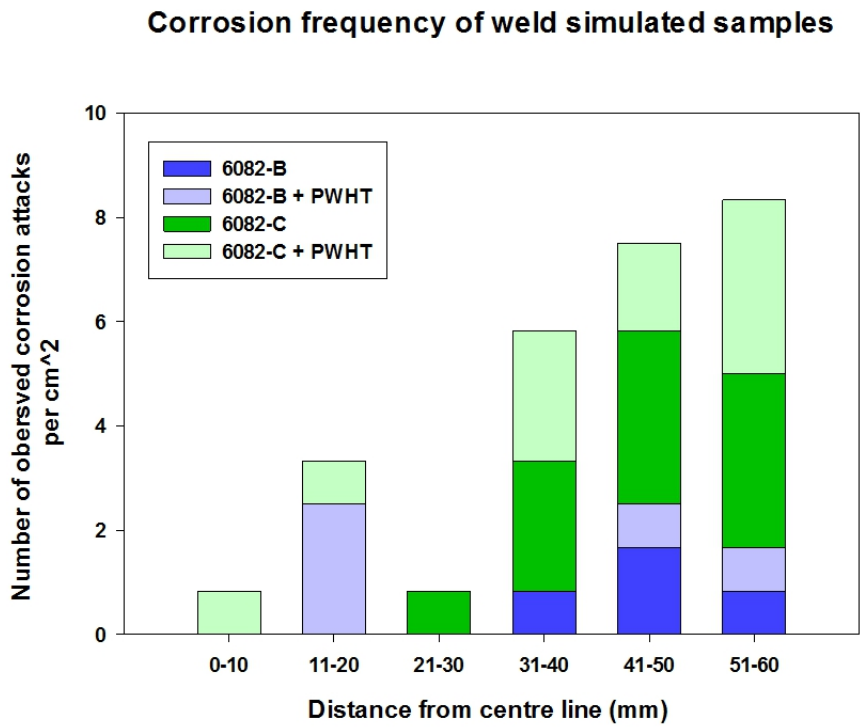

Figure 4.22.: *Corrosion frequency of alloy 6082-A, 6082-B and 6082-C as a function of distance from centre line. It should be noted that no corrosion attacks were observed for alloy 6082-X nor 6082-A. All registred pits had a pit depth greater than or equal to 30 μm.*

An overview of the observed corrosion frequency in alloys 6082-B and 6082-C as a function of distance from centre line is shown in figure 4.22. It should be noted that the figure only provides the frequency and not the extent of the particular attack. In fact, most attacks were found to be rather small and IGC was only observed along sub grains with grain diameters in the order of 1-3 μm. Nevertheless, the frequency was observed to increase with increasing distance from the centre line, at least in the case of alloy 6082-C. Figure 4.23 shows pitting corrosion as well as IGC along subgrains in naturally aged 6082-C after PWHT.

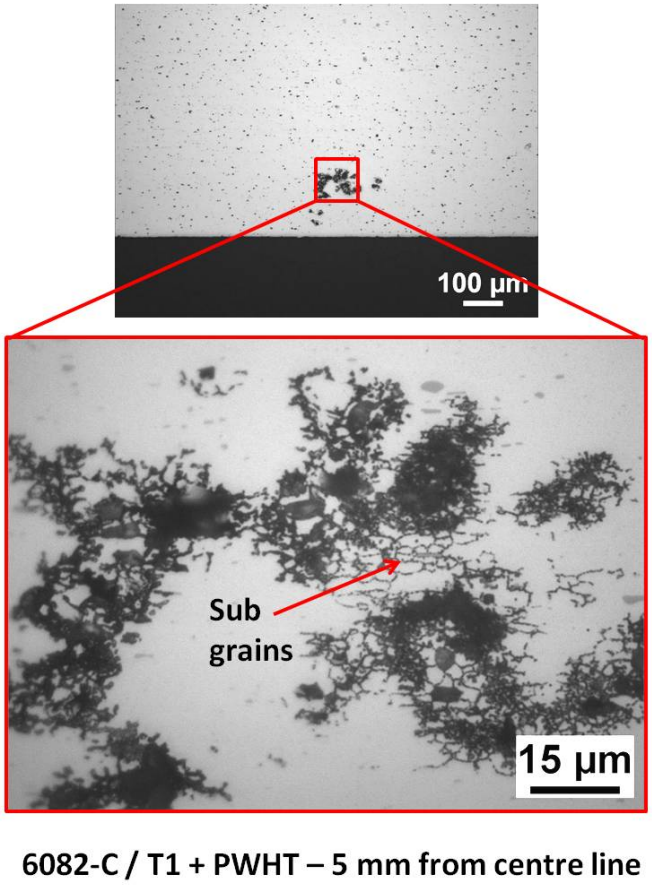

Figure 4.23.: *Micrographs taken 5 mm from the centre line showing pitting and IGC in alloy 6082-C / T1 after PWHT. Micrographs taken parallel to the direction of extrusion.*

4.3.4. Weight loss measurements

Weight loss measurements after the accelerated IGC test are presented in table 4.3.

Table 4.3.: *Weight loss measurements of all the samples after IGC testing. WS = weld simulated, PWHT = post weld heat treatment.*

Sample	Cu ($wt\%$)	Temper	Area (cm^2)	Weight loss (mg/cm^2)	Corroded layer (μm)
MIG					
6082-X	0.002	T1	220.7	0.30	1.3
6082-X	0.002	T6	223.4	0.40	1.6
FSW					
6082-X	0.002	T6	120.7	0.41	1.5
FSW + PWHT					
6082-X	0.002	T6	116.0	0.6	2.2
WS					
6082-A	0.001	T1	105.9	0.62	2.3
6082-B	0.10	T1	105.9	1.37	5.1
6082-C	0.60	T1	104.1	2.98	11.0
6082-X	0.002	T1	109.9	0.55	2.0
WS + PWHT					
6082-A	0.001	T1	104.1	0.72	2.7
6082-B	0.10	T1	102.5	1.17	4.3
6082-C	0.60	T1	104.1	2.84	10.5
6082-X	0.002	T1	109.9	0.64	2.4

As can be seen from the table, the effect of Cu content on the weight loss is detrimental as the weight loss is found to increase rapidly with increasing copper concentration. Also, post weld heat treatment does not seem to have any significant effect on corrosion resistance, and only a minor decrease in weight loss is seen. Moreover, these observations are shown schematically in figure 4.24 for weld simulated samples. However, the data presented above only gives the total weight loss and cannot be used to establish the definite extent of localized corrosion. Finally, samples welded by FSW and MIG show similar weight loss, thus no correlation between welding technique and corrosion rate can be drawn, at least not from simple weight loss measurements.

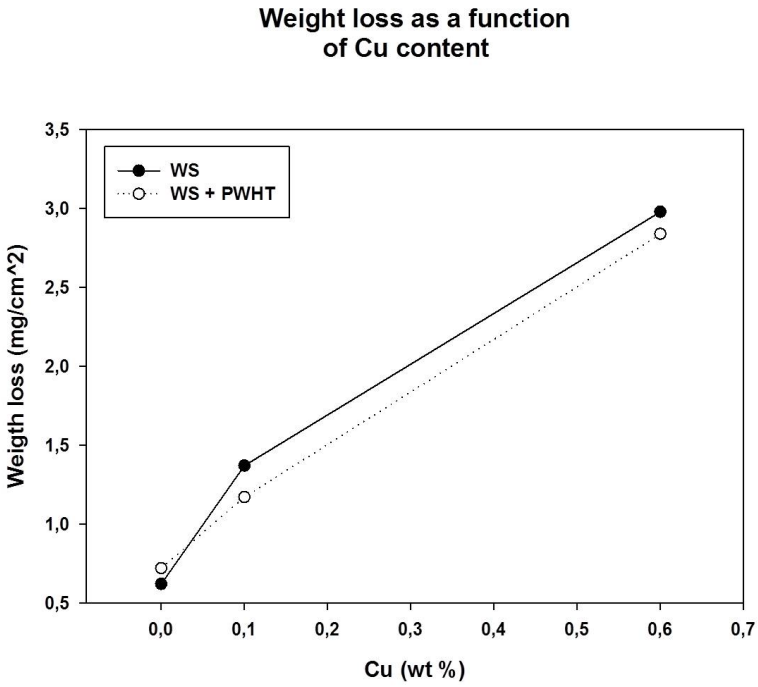

Figure 4.24.: *Weight loss as a function of Cu-content on samples subjected to weld simulation (WS) and post weld heat treatment (PWHT). Data is based on measurements of alloys 6082-A, 6082-B and 6082-C with Cu concentrations of 0, 0.10 and 0.60 wt% respectively.*

4.4. SWAAT test

Table 4.4 presents pit density as well as pit size and depth for all the samples that were subjected to SWAAT testing. As can be seen from the table, in the case of alloys 6082-A, 6082-B and 6082-C, the severity from pitting corrosion increases with increasing Cu-content. In fact, both pit density, pit diameter and pit depth increases as the Cu content increases from 0 wt% in the case of alloys 6082-X and 6082-A to 0.60 wt% for alloy 6082-C. Furthermore, the maximum pit depth is found to be almost 1.2 mm, which is significant considering the plate thickness being 2 mm.

Analysis of alloy 6082-X revealed that samples welded by FSW appears to be the ones that display the highest resistance towards pitting corrosion. However, the maximum pit depth observed is found to be somewhat higher than for the MIG welded samples. The comparison between MIG and FSW welding techniques may, however, be misguided as the MIG samples were exposed to SWAAT testing for 25 days, whereas the duration for the FSW samples were 15 days. In addition, PWHT was performed on FSW samples only.

All measurements of pits after SWAAT testing are presented in appendix B as a function of distance from centre line or weld.

Table 4.4.: *Measured pit density, depth and size for all the SWAAT tested samples. Presented mean data are based on average values for selected pits at distances ranging from 0 to 50 mm from the centre line. Also, pit density data are based on all pits observed on a macro scale within the above-mentioned range. Tested area* = 20 cm^2.

Sample $(Alloy/temper)$	**Cu** $(wt\%)$	**Pit density** $(pits/cm^2)$	**Mean size** *(mm)*	**Mean depth** **(**μm**)**	**Max depth** **(**μm**)**
WS + PWHT					
6082-A / T1	0.001	1.5	0.5	215	370
6082-B / T1	0.10	3.4	1.2	439	800
6082-C / T1	0.60	3.8	1.9	619	1150
6082-X / T6	0.002	3.3	0.5	375	560
MIG					
6082-X / T6	0.002	3.8	0.4	287	400
FSW + PWHT					
6082-X / T6	0.002	2.2	0.4	269	460

Moreover, results from the SWAAT test revealed pitting corrosion on all samples, and the susceptibility was in general observed to increase with increasing Cu content. However, for artificially aged samples of alloy 6082-X severe pitting attacks were found. In sections 4.4.1 and 4.4.2 macro images of alloys 6082-X,6082-A,6082-B and 6082-C after SWAAT testing are presented, along with the measured hardness profile. Also, pit density, pit depth and pit diameter are determined as a function of distance from centre line for the various welding cycles.

4.4.1. Samples welded by MIG and FSW

This section contains optical micrographs as well as macro images of samples subjected to FSW and MIG welding after SWAAT testing. For the macro images the corresponding hardness profiles are presented, in order to examine if there exists a correlation between attacks from pits and microstructural effects. Moreover, the corrosion resistance in the weld metal, the HAZ and the base metal has been evaluated.

Figure 4.25 shows macro images of alloy 6082-X welded by FSW + PWHT and MIG. An interesting observation for both cases is the low pit density in the HAZ close to the weld. As a result, it appears as if welding has a beneficial effect on the resistance towards pitting corrosion. However, for the FSW samples a high density of small pits, with pit sizes of approximately 0.4 mm and pit depths between 70 and 360 μm, were observed in the centre of the friction weld. Also, for the MIG welded samples, pits measuring 0.5 mm with average depths of approximately 300 μm were observed in the fusion zone. It should, however, be noted that significant variations in pit depth and size were observed. Finally, the narrow HAZ for the FSW samples as compared to the MIG samples should be noted.

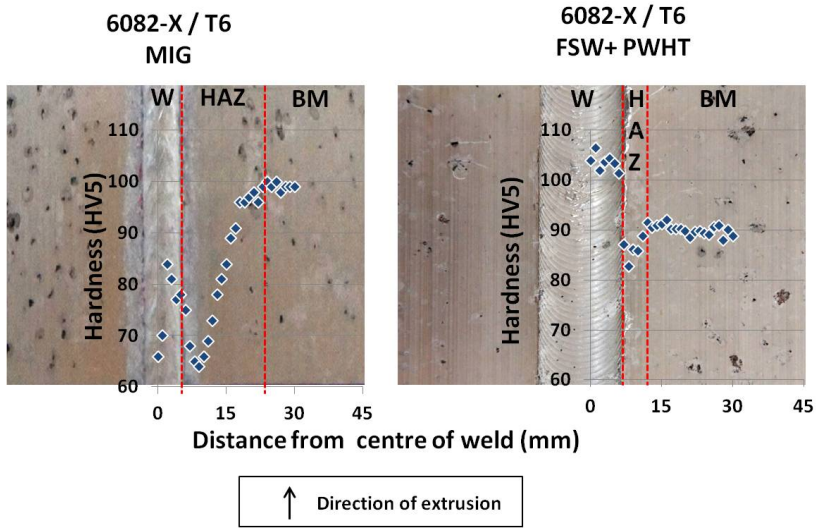

Figure 4.25.: *Macro images after SWAAT testing of alloy 6082-X / T6 subjected to MIG (left) and FSW + PWHT (right), as well as hardness profiles prior to corrosion testing. Indicated regions are based on hardness measurements across the welded section. W = weld, HAZ = Heat affected zone, BM = Base metal.*

Moreover, for the samples welded by FSW, superior corrosion resistance is observed even at some distance into the base metal. As a matter of fact, for both welding techniques, a region 5-15 mm from the centre of the weld is observed to display increasing resistance to pitting corrosion. This increased resistance to pitting corrosion in the heat affected zone for both welds is discussed in further detail in section 5.6.1.

MIG

Figure 4.26 shows corrosion attacks in MIG welded 6082-X / T6 at the fusion line, in the HAZ close to the fusion line and in the base material. An interesting observation is the difference in corrosion behaviour observed in the HAZ and the base material. In the HAZ the recrystallized layer appear to have been severely etched, however in the base material these attacks are not observed.

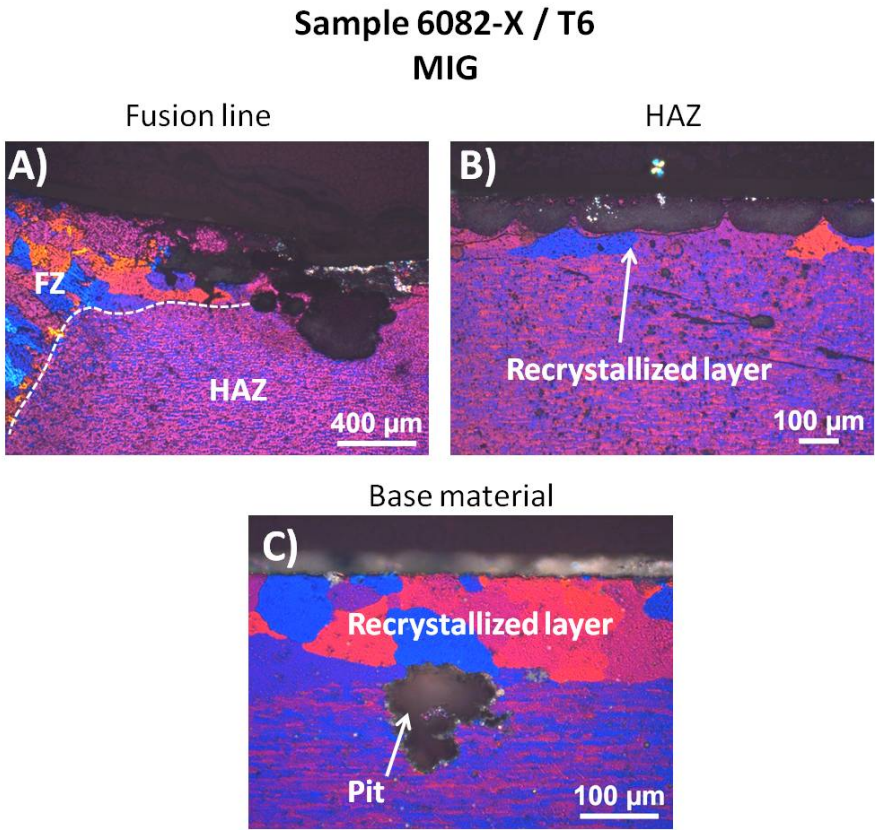

Figure 4.26.: *Micrographs of MIG welded 6082-X / T6 after SWAAT testing taken perpendicular to the direction of extrusion.* ***A)*** *Pitting corrosion at the fusion line,* ***B)*** *Etching of the recrystallized layer in the HAZ close to the fusion line and* ***C)*** *Pitting corrosion in the base metal, however no etching of the recrystallized layer. FZ = Fusion zone, HAZ = Heat affected zone.*

In figure 4.27 macro images after SWAAT testing of alloy 6082-X / T6 subjected to MIG welding are shown and all the observed pits are highlighted with black dots. Moreover, from the figure the improved resistance to pitting corrosion in the heat affected zone may be observed. Also, the etched layer close to the fusion zone should be noted.

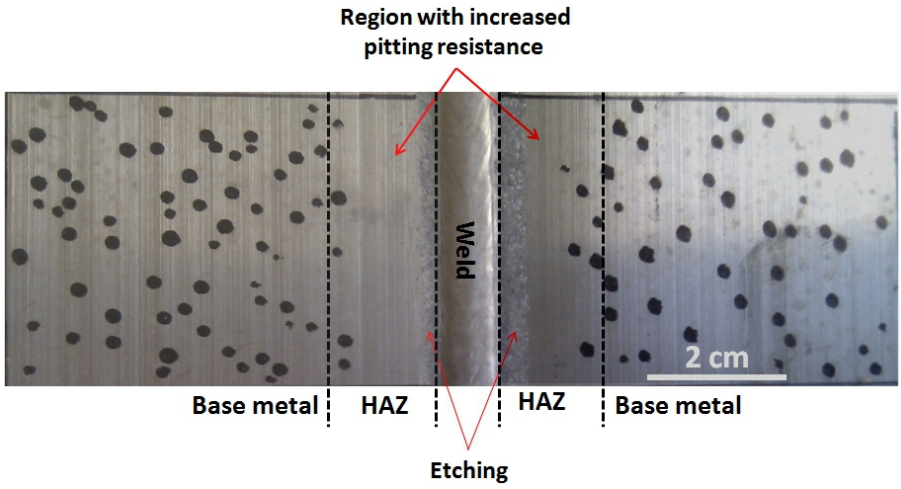

Figure 4.27.: *Macro images after SWAAT testing of alloy 6082-X / T6 subjected to MIG. Pits are highlighted with black dots. Note the lack of pits in the heat affected zone and the etched layer close to the fusion zone.*

FSW

For the FSW samples severe pitting corrosion was observed in the base metal as seen in figure 4.28. Also, as seen in figure 4.28B some IGC is observed along the recrystallized grains. For the FSW samples, however, no etching of the welded section was observed.

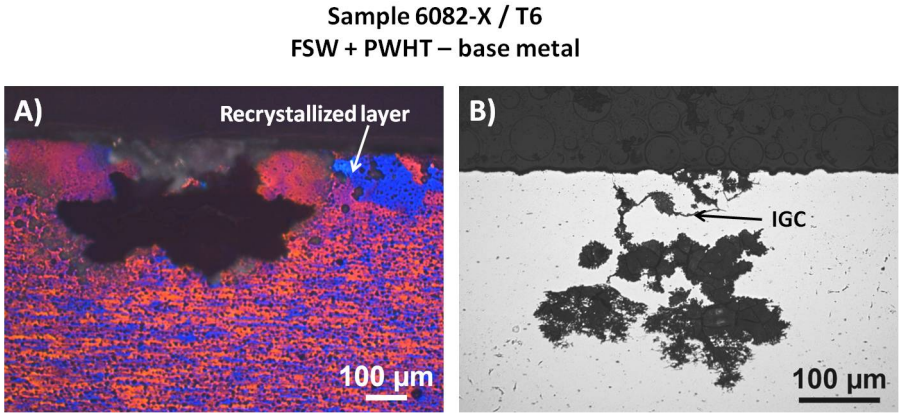

Figure 4.28.: *Micrographs of friction welded 6082-X / T6 after SWAAT testing taken perpendicular to the direction of extrusion.* ***A)*** *Pitting corrosion in the base metal close to the recrystallized layer,* ***B)*** *Pitting and intergranular corrosion of the recrystallized layer.*

Finally, as already mentioned, a high density of small pits were observed in the weld centre of the FSW sample as seen in figure 4.29 below.

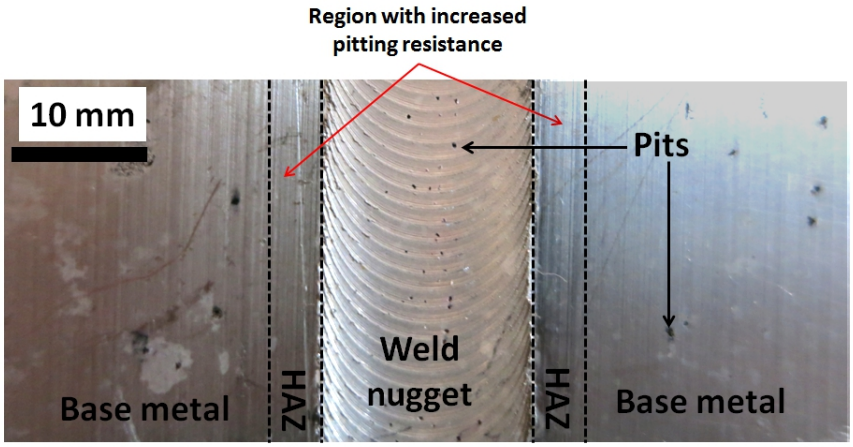

Figure 4.29.: *Macro image showing a high density of pits in the centre of the friction weld in alloy 6082-X.*

Pit measurements

Pit density, size and depth of samples welded by MIG and FSW + PWHT are presented in figure 4.30 through 4.32. An important observation is the lack of pits observed in the HAZ for the sample welded by FSW. In fact, figure 4.30 reveals significant variations in corrosion behaviour in the weld zone for the two welding techniques. For the samples welded by FSW several small pits were observed in the centre of the friction weld. In fact, the pit density was measured to 0.85 pits per cm^2 in the friction weld, as opposed to 0.2 pits per cm^2 in the MIG fusion weld. However, in the narrow HAZ for the FSW samples no pits were observed, as indicated by the lack of data for this region in figure 4.30 through 4.32. It should, however, be noted that the extent of the HAZ in the FSW profiles is significantly smaller than for the MIG welded samples.

Also, for the MIG welded samples the pit density was found to be low in the HAZ. In fact, pits were only observed at distances close to 20 mm from the centre line which represents the transition region between the HAZ and the base material. In conclusion, for both welding techniques the HAZ appears to show a high corrosion resistance, superior to both the base material and the weld metal. Also, as all visible pits in the selected area were registered, no error bars are indicated in the pit density chart.

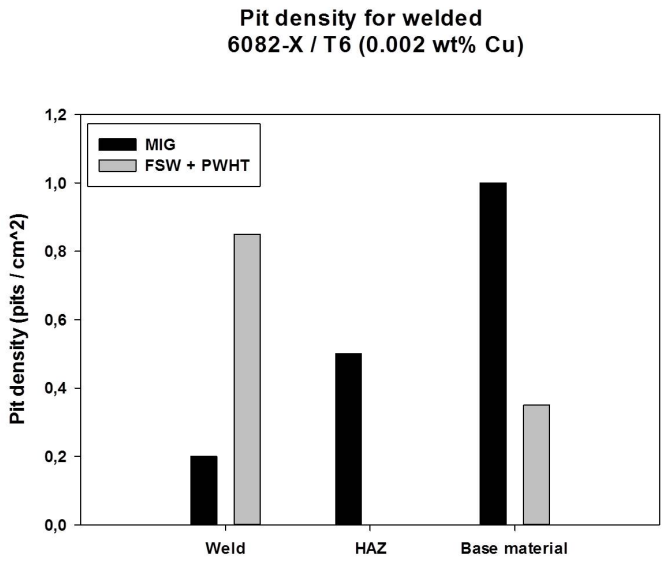

Figure 4.30.: *Observed pit densities in the weld, the heat affected zone (HAZ) and the base material for alloy 6082-X / T6 welded by MIG and FSW. Note that no pits were observed in the narrow HAZ for the FSW samples.*

Finally, for the base material, it appears as if the corrosion resistance is superior for the samples welded by FSW. In fact, as can be seen from figure 4.25, for the base metal in proximity to the HAZ, no pits were observed. However, as mentioned above, due to differences in heat treatments after welding and duration of testing, no absolute comparison between the two welding techniques can be drawn.

Measured pit diameter of SWAAT tested samples are shown in figure 4.31. As can be seen from the figure, no clear correlation between pit size and distance from the weld can be seen. Moreover, figure 4.32 presents measured pit depths and it appears as if the deepest pits are located in the HAZ, were the alloy shows reduced strength. However, as already mentioned, this correlation is only found for the MIG welded samples as no pits were observed in the HAZ for the FSW profiles.

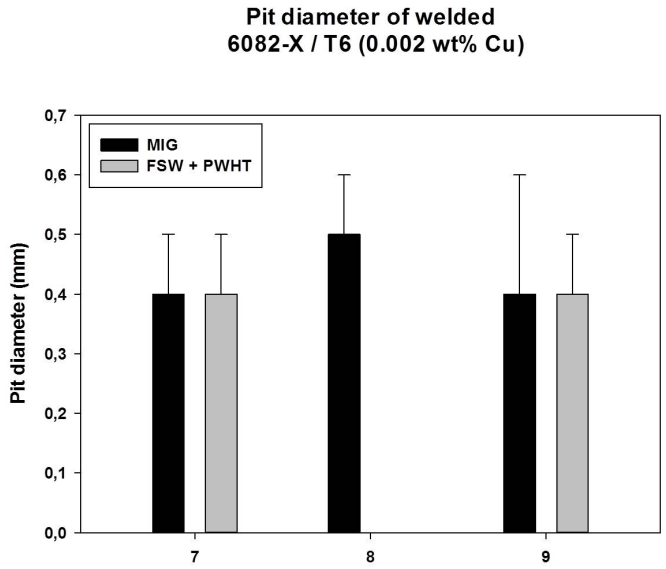

Figure 4.31.: *Observed pit diameters in the weld, the heat affected zone (HAZ) and the base material for alloy 6082-X / T6 welded by MIG and FSW.*

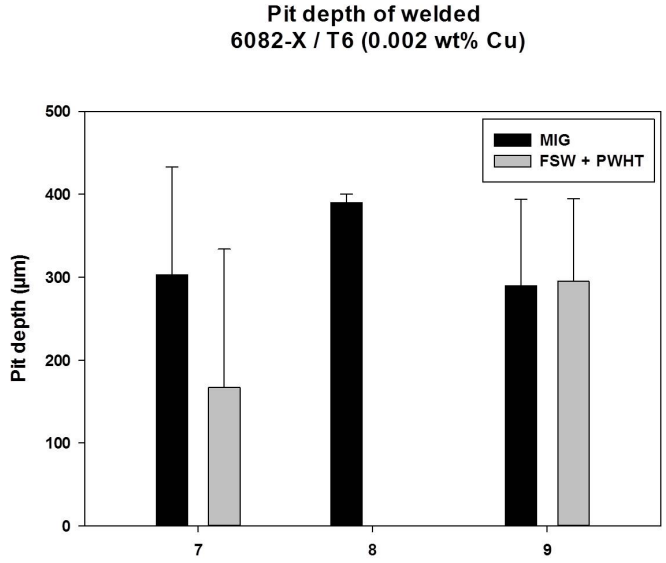

Figure 4.32.: *Observed pit depths in the weld, the heat affected zone (HAZ) and the base material for alloy 6082-X / T6 welded by MIG and FSW.*

4.4.2. Weld simulated samples

This section contains optical micrographs as well as macro images of the weld simulated samples after SWAAT testing. It should be noted that all weld simulated samples were subjected to PWHT prior to corrosion testing. As a result, the indicated temper designation reflects the initial ageing condition. For the macro images the corresponding hardness profiles are presented, in order to examine if there exists a correlation between attacks from pits and microstructural effects. Moreover, the different temperature regions during weld simulation are also presented. The approximate locations of these temperature regions are based on the temperature gradient during shown in figure 3.4.

Figure 4.33 shows macro images of three parallels of alloy 6082-X / T6 together with the hardness profile. From the figure it appears as if there exists a region located approximately 30-35 mm from the centre line with increased sensitivity towards pitting corrosion. Closer examinations of these regions reveal that these areas consists of several smaller pits resulting in macro sized craters. An interesting observation is the location of these heavily attacked areas which appear close to the point of minimum hardness. Moreover, the reduction in hardness may be explained by overageing of the alloy which has been observed to favour pitting corrosion as seen in section 2.5.2 [5, 8–10].

Macro images of alloys 6082-A, 6082-B and 6082-C from T1 tempers are shown in figure 4.34. As opposed to the artificially aged 6082-X sample, no clear correlation between the hardness profile and the susceptibility to pitting corrosion can be observed. However, the pit density is observed to increase drastically with increasing Cu content.

Moreover, figure 4.35 shows micrographs of corrosion attacks after SWAAT testing of weld simulated alloys. As can be seen from the figure, most attacks were in the form of pitting corrosion. However, attacks from IGC along sub grains were also observed, particularly for alloys 6082-B and 6082-C containing 0.10 and 0.60 wt% Cu respectively. However, some IGC was also observed for sample 6082-X / T6 as seen in figure 4.36, despite the Cu deficiency of the alloy. In fact, IGC attacks were observed in the recrystallized layer as well as along sub grains, at distances of 4 and 12 mm from the centre line respectively.

As seen in sections 2.5.1 and 2.6, the susceptibility to both pitting corrosion and IGC increases rapidly with increasing Cu concentration. However, an interesting observation is made for alloy 6082-X / T6. Despite the Cu deficiency of the alloy, significant pitting corrosion can be observed. In fact, pit densities and depths are found to be of similar order as for the naturally aged alloy 6082-B, containing 0.10 wt% Cu. These findings should highlight the importance of temper condition and thermal processing when the susceptibility towards localized corrosion in AlMgSi alloys is to be determined.

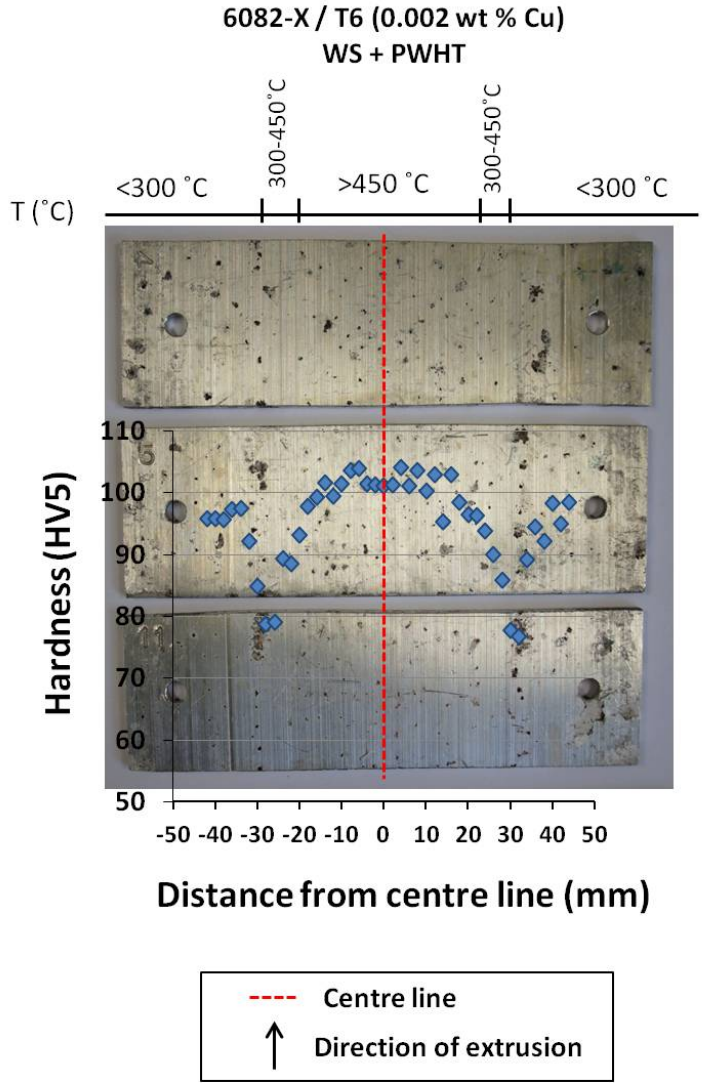

Figure 4.33.: *Hardness profile and macro images after SWAAT testing of alloy 6082-X subjected to weld simulation and PWHT. Temperature regions during weld simulation are shown in the upper part of the figure.*

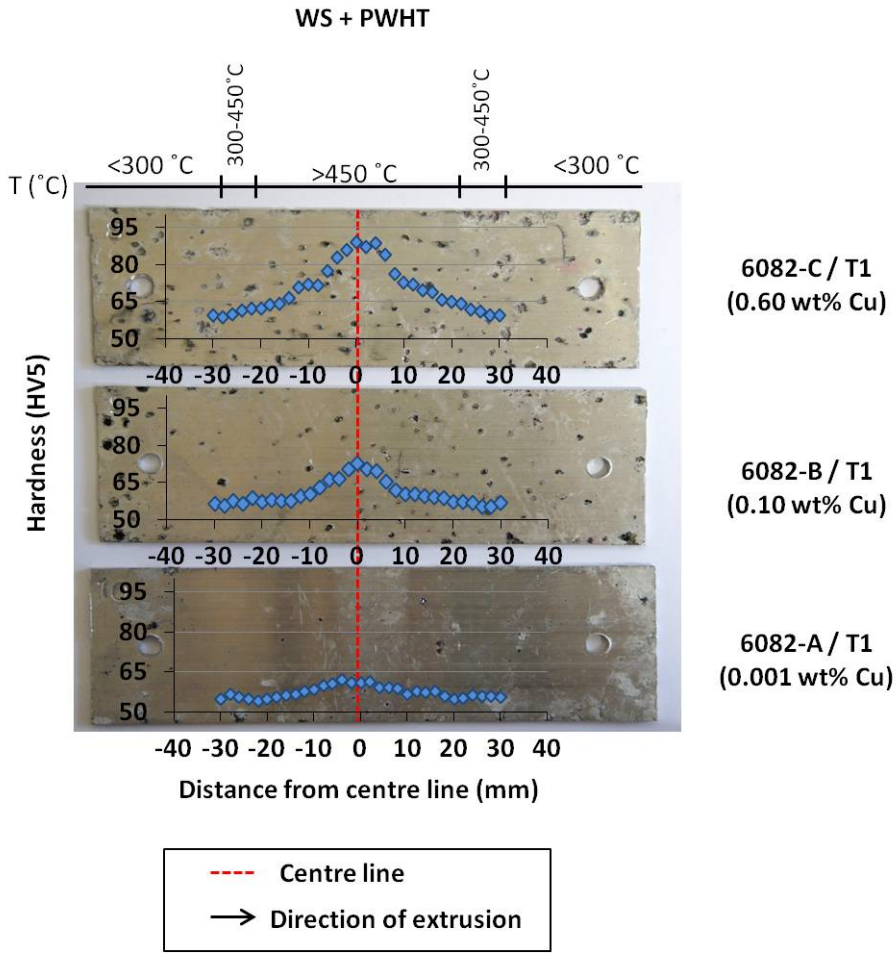

Figure 4.34.: *Macro images after SWAAT testing of alloy 6082-A (bottom), 6082-B (middle) and 6082-C (top) subjected to weld simulation and PWHT, as well as hardness profiles prior to corrosion testing. Temperature regions during weld simulation are shown in the upper part of the figure.*

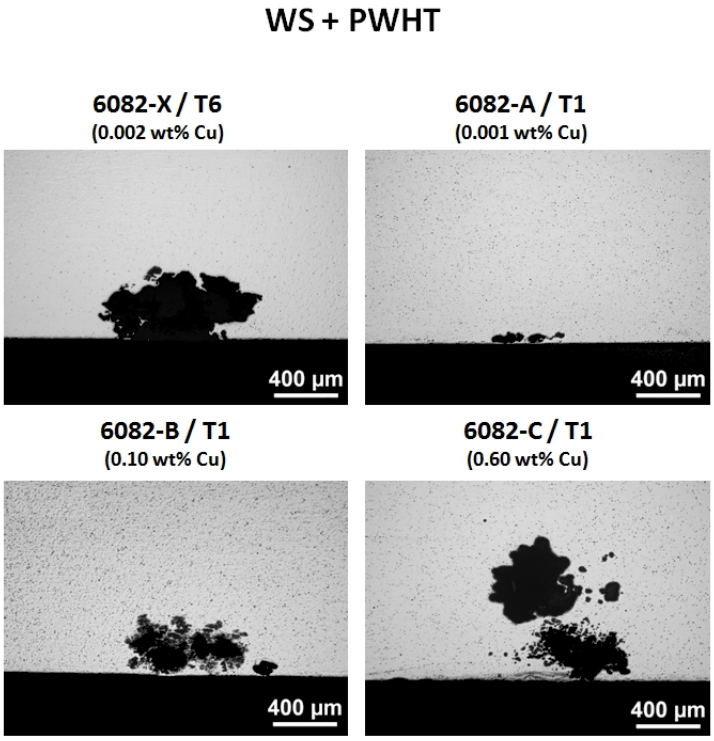

Figure 4.35.: *Corrosion attacks after SWAAT testing of weld simulated alloys. Micrographs taken perpendicular to the direction of extrusion for alloy 6082-X and parallel to the direction of extrusion for alloys 6082-A, 6082-B and 6082-C.*

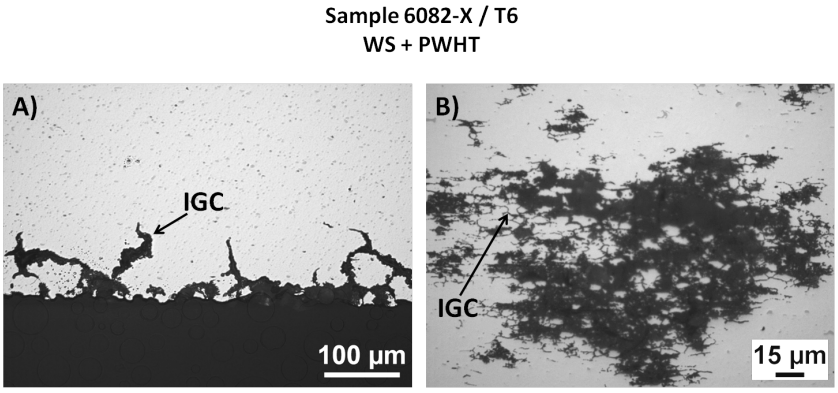

Figure 4.36.: *IGC after SWAAT testing of alloy 6082-X / T6 taken perpendicular to the direction of extrusion. A) Superficial attacks in the recrystallized layer 4 mm from the centre line and B) sligth IGC along sub grains 12 mm from the centre line.*

Pit measurements

Pit density, size and depth of weld simulated samples are presented in figure 4.37 through 4.39, as a function of peak temperature during weld simulation, with the corresponding distance from centre line as shown in table 4.5. However, it should be noted that small variations in the peak temperature during weld simulation were observed as shown in table 3.4.

Table 4.5.: *Peak temperature regions and the corresponding distances from centre line.*

Temperature (°C)	Approximate distance from centre line (mm)
> 450	0 - 20
300 - 450	20 - 30
< 300	30 - 50

Moreover, as all visible pits in the selected area were registered, no error bars are indicated in the pit density chart. For alloy 6082-C some interesting trends in corrosion behaviour with respect to distance from centre line can be observed. In fact, pit densities and the pit depths were observed to decrease with decreasing peak temperature. In contrast, the pit size was observed to increase with decreasing peak temperature. However, as indicated by the error bars in the pit size diagram, substantial variations in observed pit diameter were observed for the low temperature region (<300 °C).

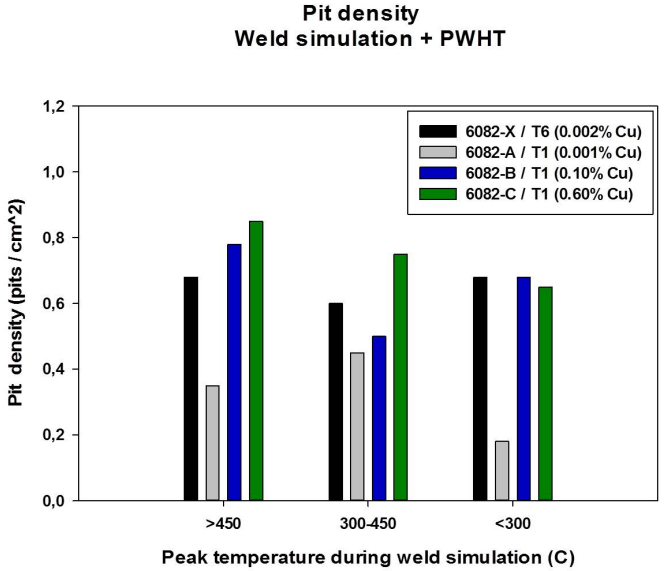

Figure 4.37.: *Observed pit densities for samples subjected to weld simulation and post weld heat treatment (PWHT) as a function of peak temperature during weld simulation.*

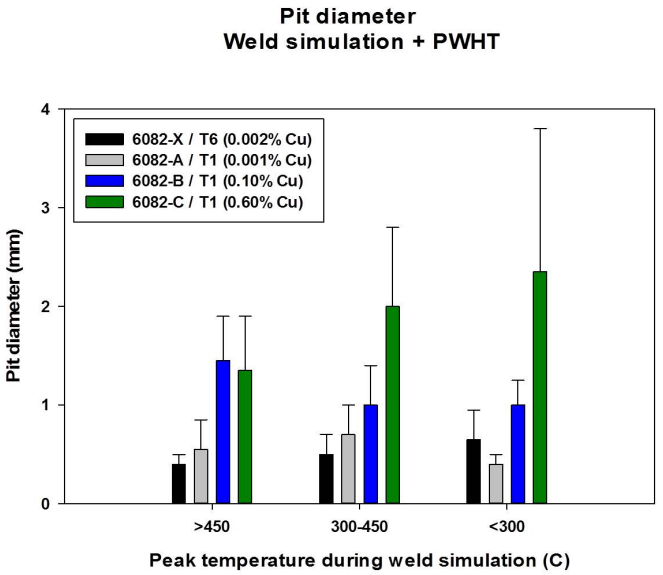

Figure 4.38.: *Observed pit diameters for samples subjected to weld simulation and post weld heat treatment (PWHT) as a function of peak temperature during weld simulation.*

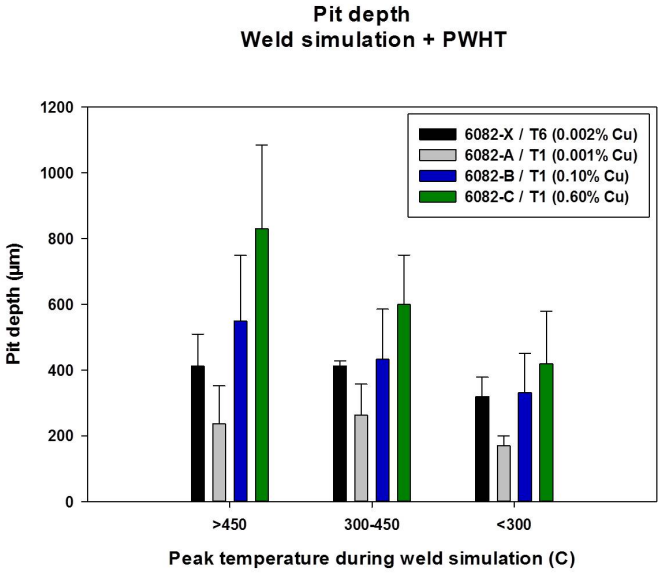

Figure 4.39.: *Observed pit depths for samples subjected to weld simulation and post weld heat treatment (PWHT) as a function of peak temperature during weld simulation.*

4.5. Grain boundary microstructure

Grain boundary characterization was performed on selected samples in order to identify phases responsible for the observed corrosion attacks seen in the previous sections. All phases were characterised by the use of LV-FESEM and EDS analysis and are summarized in table 4.6. However, as the EDS analysis is qualitative, the presented phases are only suggestions and are not absolute. Moreover, presented suggestions are based on studies by Mondolfo [14] and Mrowka-Nowotnik [58]. Examples of EDS analysis of such phases are given in sections 4.5.1 through 4.5.3 below. In the presented analysis, the term 'Al double peak' refers to the simultaneous detection of two characteristic Al X-rays (K_α) causing the measured energy to be doubled.

Table 4.6.: *Phases observed on grain boundaries for the alloys considered in this study. Presented compositions are suggestions based on work by Mondolfo et al. [14] and Mrowka-Nowotnik [58] and are not definite.*

Sample	Cu (wt%)	Suggested phase[a].
6082-X (Base metal, HAZ)	0.002	$(FeMn)_3SiAl_{15}$ Mg_2Si
6082-X (Fusion zone, MIG)	0.002	Mg_2Al_3 $(FeMn)Al_6$ $FeSiAl_5$ Mg_2Si
6082-A	0.001	$(FeMn)_3SiAl_{15}$ Mg_2Si
6082-B	0.10	$(FeMn)_3SiAl_{15}$ Mg_2Si
6082-C	0.60	$(FeMn)_3SiAl_{15}$ Mg_2Si $(Cu)(FeMn)_3SiAl_{15}$(?) $(Cu, Mn)FeSiAl_5$ (?)

[a]Presented phases are suggestions based on work by Mondolfo [14] and Mrowka-Nowotnik [58].

4.5.1. Fe-rich particles

Figure 4.40 shows a LV-FESEM micrograph of a Fe-rich particle in alloy 6082-X, and the corresponding EDS analysis is presented in figure 4.41. As can be seen from the EDS spectrum, the Fe-rich particle contains significant amounts of silicon and some manganese. As a result, a suggested composition of the particle may be $(FeMn)_3SiAl_{15}$.

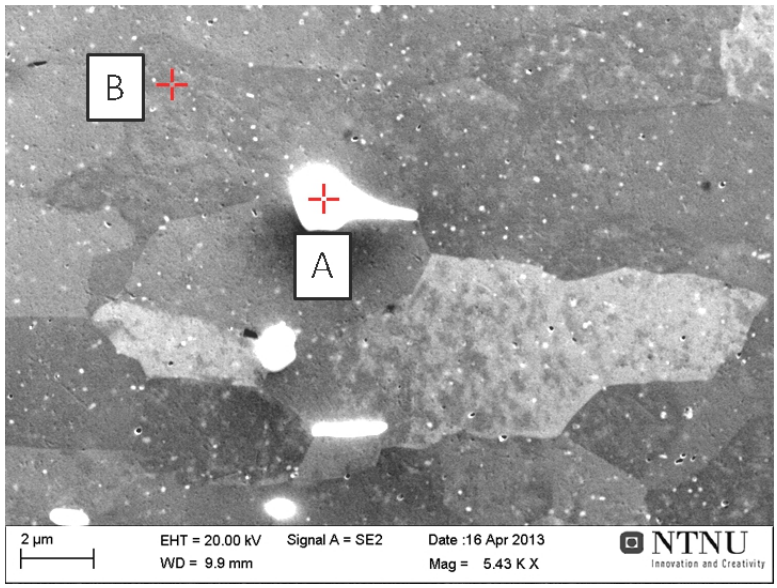

Figure 4.40.: *LV-FESEM secondary electron micrograph of a Fe-rich particle in alloy 6082-X.*

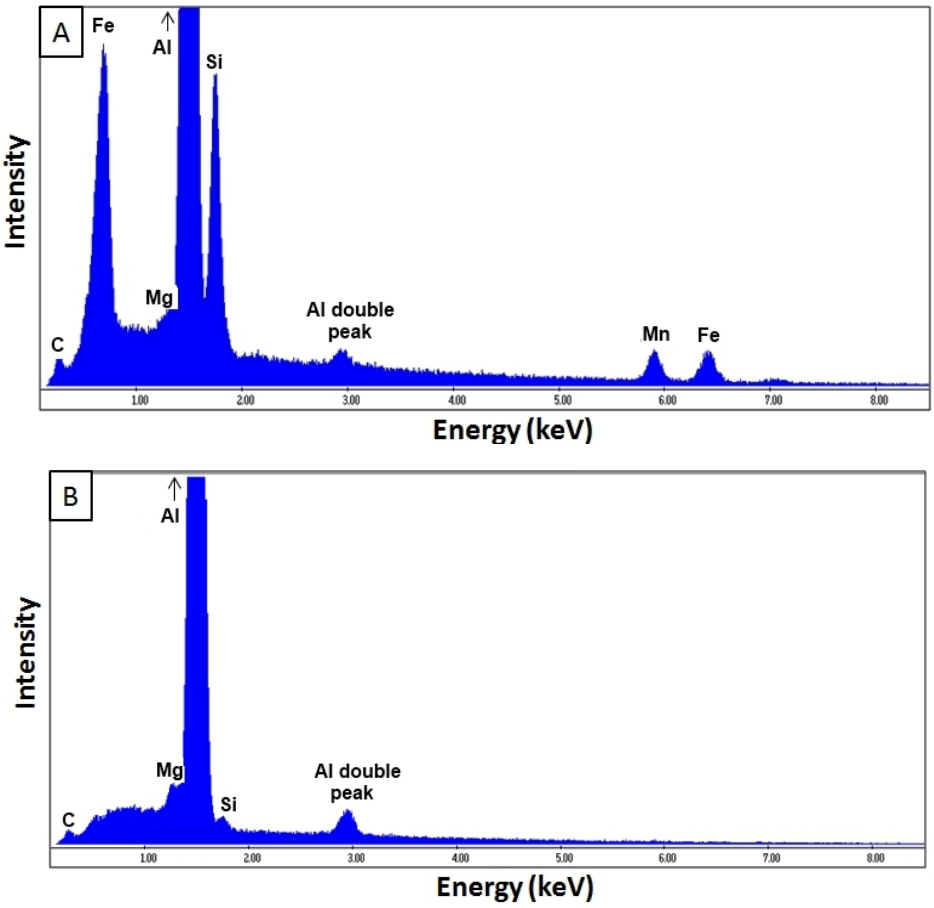

Figure 4.41.: *EDS analysis of a Fe-rich particle in alloy 6082-X.* ***A)*** *EDS analysis of particle and* ***B)*** *EDS analysis of Al-matrix.*

4.5.2. Cu containing phases

Cu-rich phases were only observed for alloy 6082-C with an example shown in figure 4.42 and the corresponding EDS spectra in figure 4.43. However, the characteristic Q-phase ($Al_4Mg_8Si_7Cu_2$) which is believed to cause susceptibility to IGC was not observed. Instead, Cu-containing phases were found to contain significant amounts of Si and Fe in addition to some Mn. Some suggested particle types include $(Cu)(FeMn)_3SiAl_{15}$ and $(Cu, Mn)FeSiAl_5$.

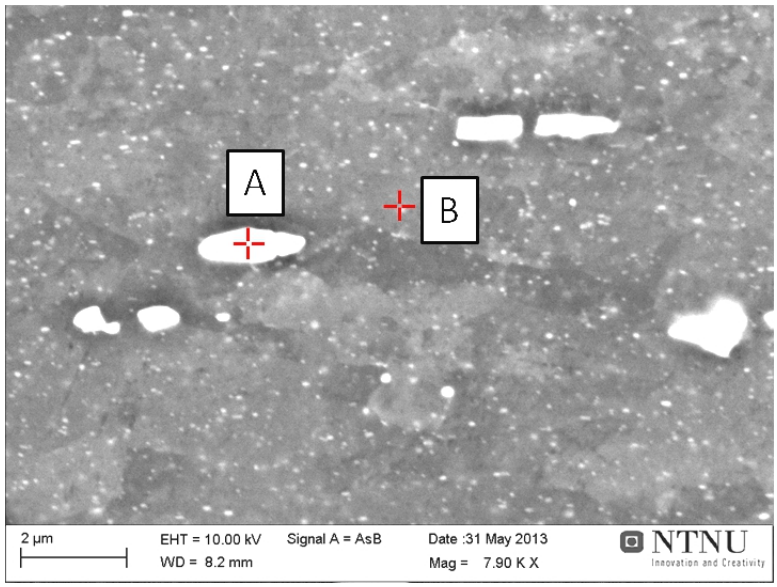

Figure 4.42.: *LV-FESEM secondary electron micrograph of a Cu-rich particle in alloy 6082-C.*

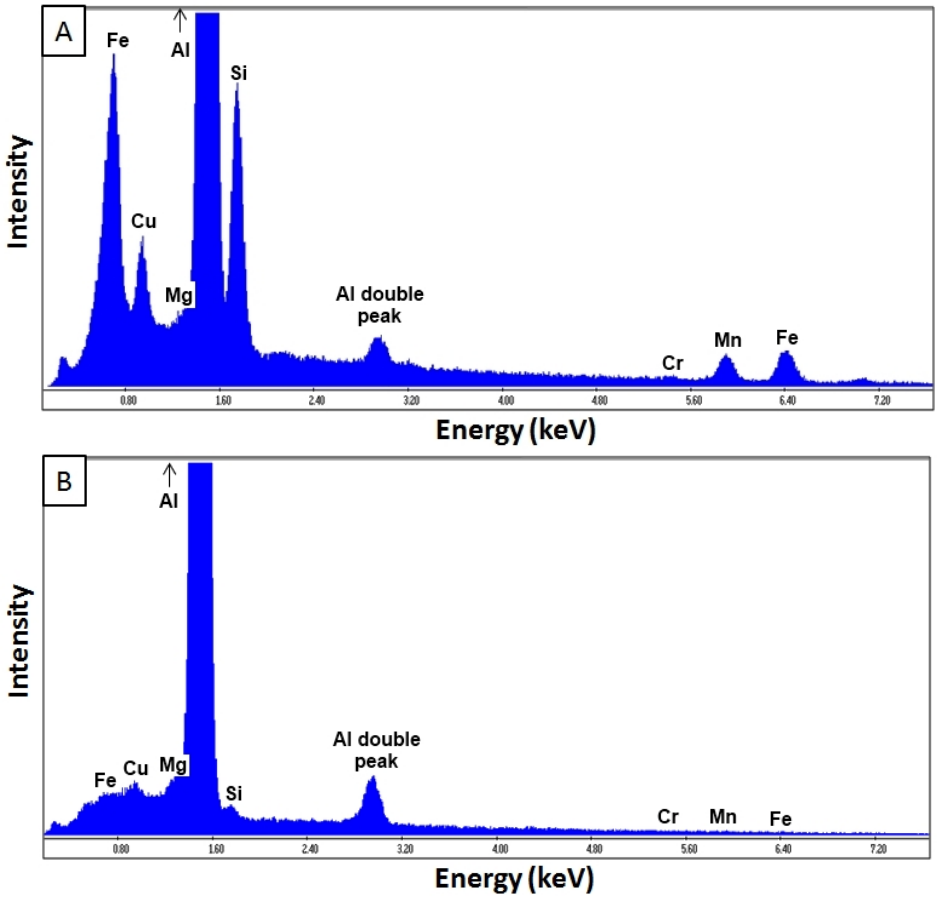

Figure 4.43.: *EDS analysis of a Cu containing particle in alloy 6082-C.* ***A)*** *EDS analysis of particle and* ***B)*** *EDS analysis of Al-matrix.*

4.5.3. Fusion zone (MIG)

Figure 4.44 below shows a LV-FESEM micrograph of grain boundary precipitates in the fusion zone of MIG welded alloy 6082-X. Furthermore, EDS analysis of a Mg-rich and Fe-rich precipitates as well as the aluminium matrix are shown in figure 4.45. The bright particle in figure 4.44 (particle A) is enriched on Mn and Fe and is believed to be $(FeMn)Al_6$. Moreover, the darker particle (particle B) is enriched on Mg and Si and is likely to be a Mg_2Si or Al_3Mg_2 type of phase. Finally, the high concentrations of Mg in the matrix of the weld metal should be noted (figure 4.44C) which arises due to the Mg-rich filler metal.

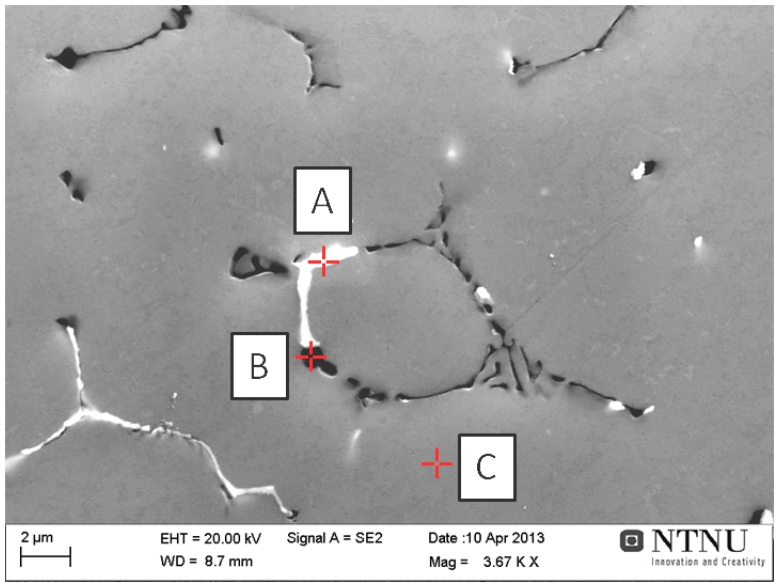

Figure 4.44.: *LV-FESEM secondary electron micrograph of a particles in the weld metal of alloy 6082-X after MIG welding.*

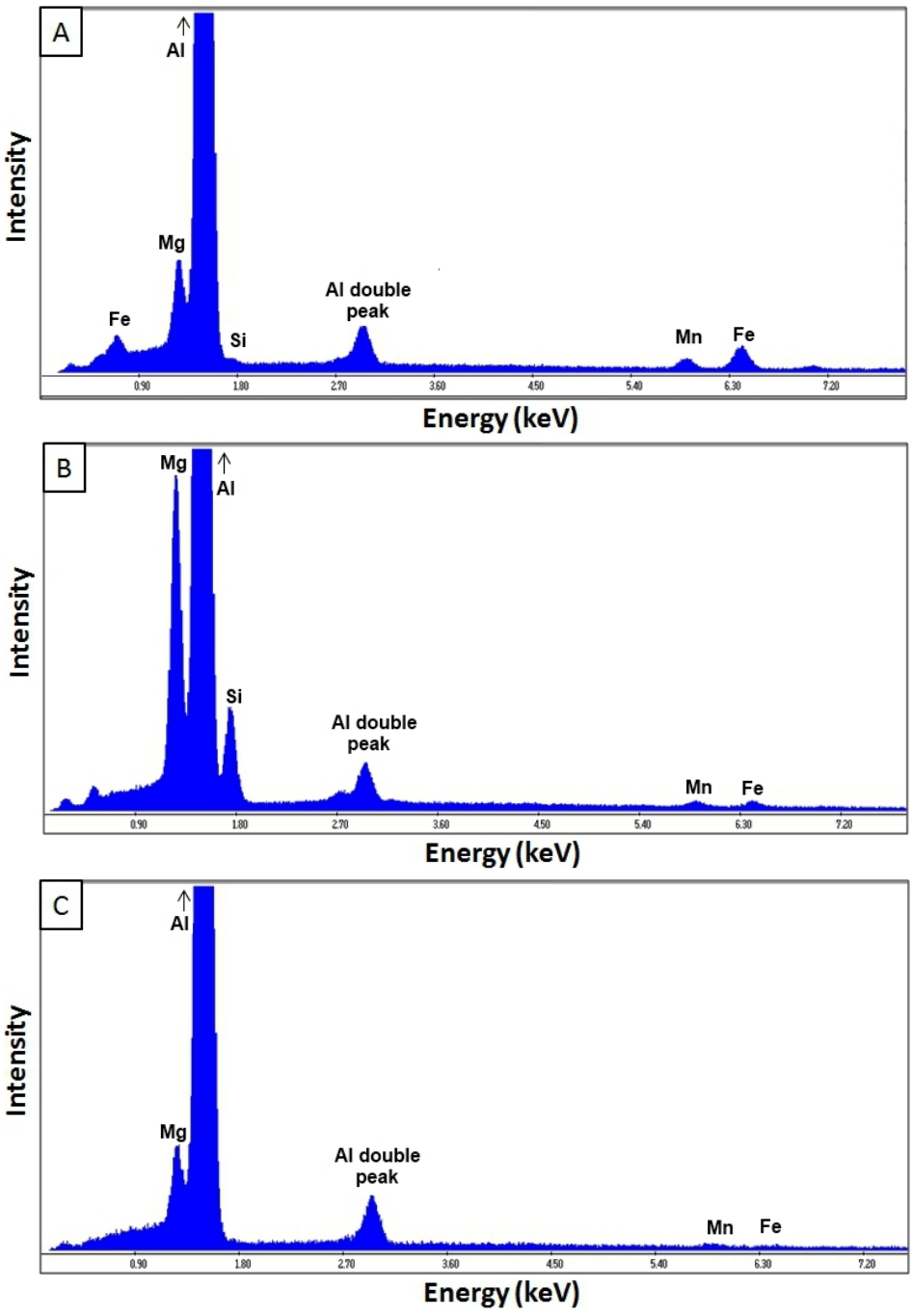

Figure 4.45.: *EDS spectrum of precipitates in the weld metal in alloy 6082-X after MIG welding.* ***A)*** *Fe/Mn-rich particle,* ***B)*** *Mg-rich phase and* ***C)*** *aluminium matrix*

4.6. Potential measurements

Open circuit potential measurements of the weld metal, fusion line, heat affected zone and base material of alloy 6082-X / T6 are shown in figure 4.46 As can be seen from the figure

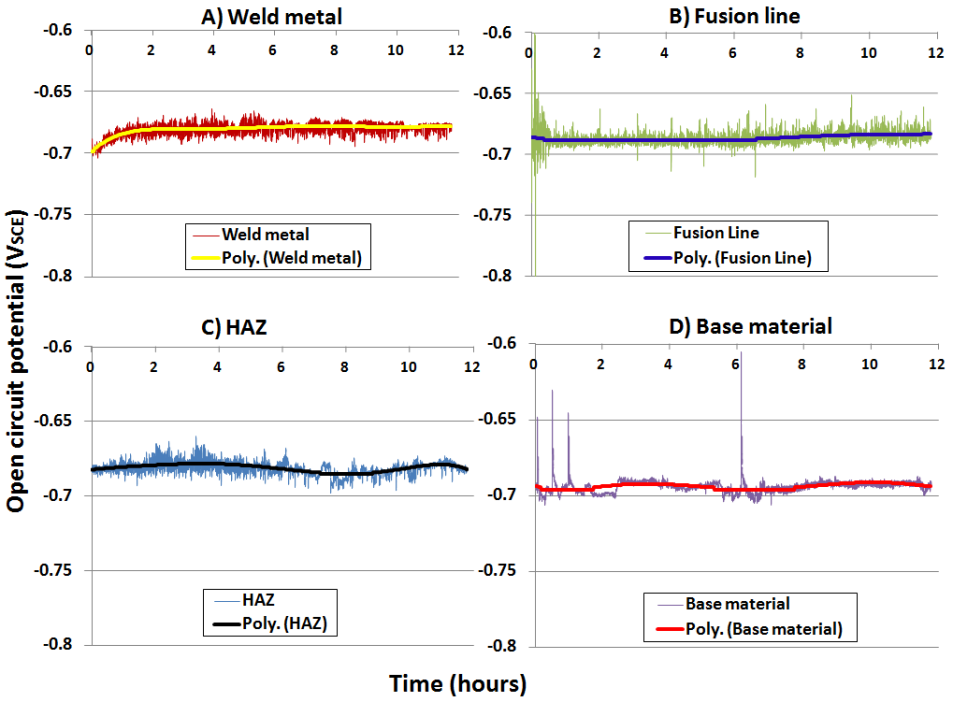

Figure 4.46.: *Open circuit potential measurements and polynomial trend lines for **A)** weld metal, **B)** fusion line, **C)** heat affected zone (HAZ) and **D)** base material.*

no significant variation in the OCP for the different locations across the welded section can be observed. In fact, most measurements are found to be within $\pm$ 30 mV. However, the base material appears to be the most active region and the OCP is observed to be close to -695 mV. Moreover, a small increase in the potential is oberved for the weld metal after 1000 seconds, as the OCP increase from approximately -700 to -680 mV. Calculated average values of the OCP for all regions are shown in table 4.7. As can be seen from the table, no significant variations can be observed, and only a slight decrease in the OCP for the base metal may be seen.

Table 4.7.: *Average potential measurements for the different regions of MIG welded 6082-X / T6.*

Region	$OCP_{average}$ (V_{SCE})
Weld	-0.681
Fusion line	-0.686
HAZ	-0.680
Base metal	-0.694

4.7. Electrical conductivity

In order to estimate the amount of solute in solid solution, and hence the susceptibility towards pitting corrosion, electrical conductivity measurements were performed on 6082-X / T6 samples welded by FSW, FSW with subsequent PWHT and MIG. Measurements were taken in the weld metal, the heat affected zone and the base metal. All measurements were made in the extrusion plane and results are shown in figure 4.47.

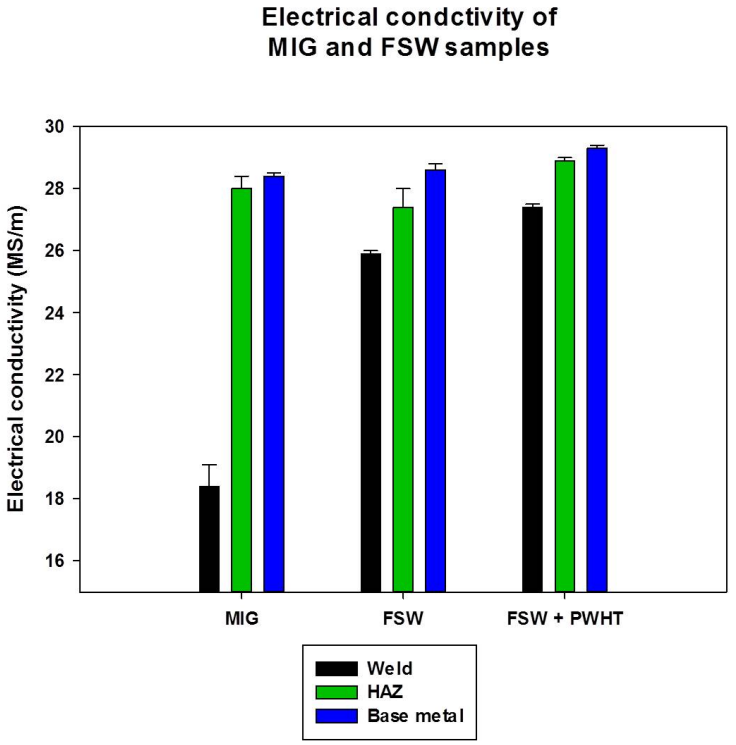

Figure 4.47.: *Electrical conductivity of samples welded by MIG and FSW for various locations along the welded section.*

As can be seen from the figure, the fusion zone in the MIG welded samples display the lowest conductivity due to the as-cast microstructure containing substantial amounts of Mg in solid solution. Moreover, for both set of welds, the electrical conductivity is observed to increase with increasing distance from the weld. As a result, the concentration of solute atoms in solid solution decreases with increasing distance from the weld. This increase is explained by reprecipitation of hardening precipitates which increases the mobility of electrons. Such observations are important when the susceptibility towards pitting corrosion is to be evaluated.

Moreover the conductivity in the base metal is observed to increase after PWHT of the friction welded samples. Such observations are believed to be linked to overageing and coarsening of the hardening precipitates which increases electron mobility. Also, precipitation of the equilibrium phase, $\beta - Mg_2Si$ may have taken place. A complete overview of the all measurements are given in appendix D.

5 | Discussion

In this chapter the most important findings during this study will be discussed in some further detail. Moreover, main focus will be to evaluate and discuss the improved corrosion resistance in the heat affected zone in alloy 6082-X subjected to FSW and MIG welding. A comprehensive discussion concerning this observation is given in section 5.6.1.

5.1. As-received materials

Hardness measurements revealed substantial deviation between claimed strength and actual strength for some test samples. Alloys 6082-A, 6082-B and 6082-C were delivered both in naturally aged (T1) and artificially aged (T6) temper condition. However, hardness measurements of the artificially aged samples concluded that the desired strength level was not met, and the samples could not be considered to be in a T6 temper condition. In fact, samples that were claimed to be in a T6 temper condition, displayed very similar hardness values as the naturally aged samples of the same alloy. As a result, all received samples of alloy 6082-A, 6082-B and 6082-C where designated the T1 temper condition. The observed differences between expected and measured hardness are mainly believed to be linked to improper heat treatment of the above-mentioned alloys.

However, a storage time of several years after solution heat treatment may serve as another explanation of the reduced hardness after artificial ageing. Ideally, artificial ageing should be carried out immediately after solution heat treatment, as the number of quenched-in vacancy clusters and solute is high, and effects from natural ageing are small. However, with a storage time of approximately four years after solution heat treatment, the effects from natural ageing are significant. Nevertheless, as only GP-zones form during natural ageing (as seen by Myhr and Grong in section 2.2), artificial ageing should contribute to an increase in strength due to precipitations of β' and β'' particles. Also, GP-zones are readily dissolved at intermediate temperatures as they are thermally unstable. In fact, an increase in hardness of the above-mentioned alloys was observed after weld simulation as seen in figures 4.11 through 4.13. This effect was further enhanced by performing post weld heat treatment. As a result, a plausible explanation of the ineffective ageing process may be reduced density of quenched-in vacancies clusters and/or solute atoms.

Furthermore, as the concentration of vacancy clusters increases exponentially with temperature, a high temperature during extrusion and solution heat treatment should prove beneficial in order to render the alloy susceptible to artificial ageing. Moreover, a difference in this susceptibility may be expected, as the extrusion temperature was different for alloys 6082-A, 6082-B and 6082-C as compared to alloy 6082-X. In fact, alloys 6082-A, 6082-B and 6082-C where extruded at approximately 410 $^{\circ}\mathrm{C}$, whereas alloy 6082-X was extruded industrially at 515 $^{\circ}\mathrm{C}$. Also, the temperature during solution heat treatment was slightly higher for alloy 6082-X. As a result, alloy 6082-X should prove more susceptible to artificial ageing as the number of quenched-in vacancy clusters is expected to be higher in this alloy. During weld simulation, however, the alloys are subjected to elevated temperatures which may have been sufficient in order to promote the nucleation and growth of hardening precipitates in alloys 6082-A, 6082-B and 6082-C. In fact, precipitation of hardening precipitates may occur in a rather large temperature interval ranging from 70-300 $^{\circ}\mathrm{C}$ [12].

5.2. General corrosion resistance of tested alloys

The overall IGC resistance was observed to be satisfactory for most alloys tested, as corrosion attacks often were limited and highly scattered. Such observations were done despite unfavourable Mg/Si ratios and copper additions up to 0.60 wt%. In particular, the moderate corrosion attacks after IGC testing of alloy 6082-C (0.60 wt% Cu, Mg/Si = 0.68) was unexpected, due to excess Si combined with high concentrations of copper. The improved corrosion resistance is mainly believed to be linked to effects of microstructure which is discussed in section 5.3.

However, all alloys proved far more susceptible to attacks from localized corrosion after SWAAT testing of the samples, with pitting corrosion being the dominant corrosion mode. In fact, pitting attacks were found to be severe with depths close to 1200 μm for alloy 6082-C. Such observations deviate strongly with pit depths reported by Bardal [49] in figure 2.19. However, the correlation presented by Bardal depends strongly on alloy, exposed area and environment.

The improved corrosion resistance after the IGC test as compared to the SWAAT test, may be explained by differences in test duration despite the lower pH during IGC testing. The duration of the SWAAT test was 15-25 days, whereas the accelerated IGC test was limited to 24 hours. Also, the establishment of active zones at grain boundaries may have been sluggish. The latter observation may be linked to the small diameter of sub grains and deformed grains, resulting in a large grain boundary area. Moreover, a large grain boundary area will possibly make the establishment of continuous cathodic networks along the grain boundaries more difficult, thus improving the corrosion resistance towards IGC. This effect is illustrated in figure 5.1.

Moreover, IGC was mainly observed in alloys containing copper (6082-B and 6082-C) with the corrosion attacks being scattered and of moderate size (<200 μm). However, it should be noted that attacks which appear to result from pitting corrosion, may in fact be

grains that have fallen out from the surface as a result of grain boundary corrosion around the entire grain or sub grain. In fact, the small grains observed in the investigated alloys render this explanation even more likely.

Finally, IGC attacks were often observed to be accompanied with attacks from pitting corrosion. Such observations are in accordance with studies by Monetta et al. [51] who studied the corrosion behaviour of friction stir welded AA6056 (section 2.7). Also, the authors reported that pitting corrosion was the dominating corrosion mode, which is also in accordance with observations made in this study.

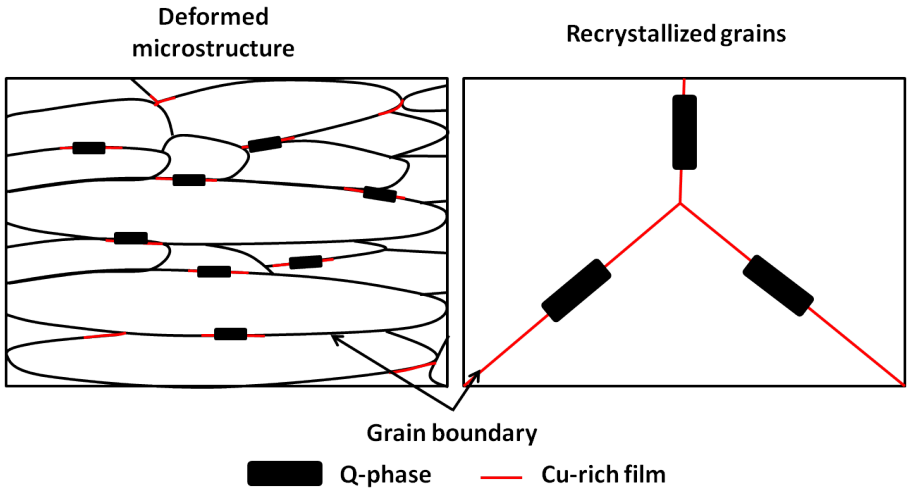

Figure 5.1.: *Effect of microstructure on the susceptibility towards IGC. Sub grains and deformed grains are separated by low angle boundaries, whereas recrystallized grains are recognized by high angle grain boundaries. The microstructure to the left is expected to display the higher corrosion resistance due to low angle grain boundaries and a large grain boundary area. Figure is based on inspiration from work by Svenningsen et al. [5].*

5.3. Effect of microstructure

The effect of microstructure, and moreover the effect of a recrystallized layer, on the corrosion behaviour of AlMgSi alloys were discussed in section 2.5.4. Furthermore, this effect appears to be of vital importance with respect to this present work. All the alloys considered in this study have been extruded into thin plates and the resulting microstructure is highly deformed. Also, the significant amount of Mn and Cr results in a rather fibrous microstructure, as these elements act as grain refiners, thus preventing recrystallization of the alloy after extrusion. Moreover, sub grains with diameters in the range of 1-3 μm were observed by analyses in LV-FESEM.

From a corrosion point of view, a fibrous microstructure is beneficial with regards to corrosion resistance of the alloy as shown by Hurlen Larsen et al. [4], and the effect was explained by Minoda and Yoshida [15]. They suggested that low angle boundaries, typically observed between sub grains, displayed a higher corrosion resistance as compared to high angle boundaries found between larger grains (i.e. in the recrystallized layer). The work presented in this study appear to fit the above-mentioned studies, as IGC attacks were observed to be limited. In fact, even for Cu containing alloys 6082-B and 6082-C attacks from IGC were rare, which can be explained by low angle boundaries between sub grains and the absence of a recrystallized layer containing high angle boundaries.

For alloy 6082-X, on the other hand, the recrystallized layer was measured to be approximately 150 μm, and some superficial attacks from IGC was occasionally observed in this layer after SWAAT testing of the alloy. However, despite the high angle boundaries in the recrystallized layer, no IGC attacks were observed as a result of the IGC test. Such observations may be explained by the low concentrations of copper in this alloy, thus preventing the precipitation of Q-phase and Cu-rich films at the grain boundaries. Although Si-rich precipitates may cause IGC in unbalanced alloys, studies by Hurlen Larsen et al. [4] suggest that grain boundary corrosion in Cu-lean alloys (<0.03 wt% Cu) only result in superficial attacks.

5.4. Effect of quenching rate from elevated temperatures

The effect of quenching rate after extrusion was discussed in section 2.5.3 and was studied by Svenningsen et al. [8–10] and Hurlen Larsen et al. [4]. Moreover, figure 2.15 shows the significance of cooling rate from an elevated temperature (i.e after extrusion) on the susceptibility to IGC. This effect is highly applicable to results obtained in this present study. In fact, all variants were water quenched after solution heat treatment. As a result, the precipitations of Q-phase and Mg_2Si is expected to be reduced. Such considerations may be used to explain the limited attacks from IGC observed in all alloys tested.

Moreover, another factor that must be taken into consideration, is the low temperatures used during extrusion of alloys 6082-A, 6082-B and 6082-C. In fact, these alloys were extruded at no more than 410 $^{\circ}\mathrm{C}$. Such lower temperatures reduce the diffusion of solute atoms significantly, as the diffusion rate increases exponentially with increasing temperature. However, subsequent solution heat treatment at 530 $^{\circ}\mathrm{C}$ should allow substantial diffusion of alloying elements, despite only being subjected to this temperature for 15 minutes. For alloy 6082-X, on the other hand, extrusion was done at temperatures close to 515 $^{\circ}\mathrm{C}$, followed by solution heat treatment at 540 $^{\circ}\mathrm{C}$ for 30 minutes. However, the lack of copper in this alloy renders it rather resistant to IGC, despite high temperatures during extrusion and solution heat treatment.

5.5. Grain boundary precipitation and IGC susceptibility

EDS analyses in LV-FESEM were used to examine grain boundary precipitates in the alloys. With respect to attacks from pitting corrosion, Fe-rich phases are particular harmful sources, as they serve as cathodic sites in the aluminium matrix. As a result, due to high concentrations of Fe in all alloys, such phases were given particular attention. Moreover, EDS analysis revealed that Fe-rich phases contained moderate amounts of Mn, thus rendering them less harmful as seen by Mondolfo [14] and Chadwick et al. [37] in section 2.5.1. However, despite the high concentration of Mn in all alloys, rather aggressive attacks from pitting corrosion after SWAAT testing were observed. As a result, the Mn content of the intermetallic particles may not have been sufficient in order to effectively reduce the activity of these particles. However, Nisancioglu [34] found that the presence of both Mn and Si in Fe-rich particles reduced the activity of these phases, as both the anodic and cathodic reaction rates were reduced. In fact, the Fe-rich particles observed during this study were found to contain significant amounts of Si, as seen in figure 4.41. It should, however, be noted that the role and importance of intermetallic particles on the susceptibility to pitting corrosion is not fully understood [43].

Also, as seen in previous chapters, IGC is closely related to the presence of Si and Cu-rich phases at the grain boundaries. From such considerations substantial attacks from IGC were expected, at least for alloy 6082-C containing 0.60 wt% Cu. Moreover, all alloys contained Si in excess of what is required to form Mg_2Si. However, analyses showed that phases enriched on Cu or Si often contained Mn or Cr, which are reported to reduce the susceptibility towards IGC [14, 36, 37]. Such considerations, in additions to the effect of microstructure discussed in the previous section, may be used to explain the moderate degree of IGC observed even in the Cu-rich alloys 6082-B and 6082-C.

Also, as seen in section 2.5.2, recent studies [4, 5, 8–10] strongly suggest that the susceptibility to IGC is higher for underaged alloys as compared to those which are peak aged. Copper containing alloys 6082-B and 6082-C were both subjected to PWHT after weld simulation. However, hardness profiles of both alloys show reduced hardness far from the centre line. This reduction in hardness may be linked to both overageing and unerageing of the alloy, with only the latter condition being reported recently to cause attacks from IGC. Overageing was reported to cause susceptibility to pitting corrosion which will be discussed in the following section.

Furthermore, attempts during this study were made to prove the existence of Cu-rich phases, and moreover the Q-phase, which have been reported to cause IGC susceptibility in Cu-rich alloys [4–10]. In particular, for alloy 6082-C numerous attempts were made. However, EDS analysis in LV-FESEM proved insufficient in order to investigate such phases. According to Svenningsen et al. [5] such phases are on a nanoscale, and examinations should ideally be performed in transmission electron microscope (TEM). Nevertheless, phases enriched on copper were observed in LV-FESEM as seen in section 4.5. However, evidence of the characteristic Q-phase ($A_{l4}Mg_8Si_7Cu_2$) was not found. Furthermore, analyses showed that Cu-rich phases contained significant amounts of Si

and Fe. As a result, the Cu containing phases are believed to result from copper being incorporated in (Si,Fe)-rich particles. Also, these particles may be a fusion of two particle types with one type being rich in copper, and the other being enriched on Si and Fe. However, this explanation seems unlikely as analysis in electron microscope should be able to distinguish particle of such dimensions (1-2 μm).

5.6. Pitting corrosion susceptibility

The correlation between pitting susceptibility and ageing was studied by Svenningsen et al. [5, 8–10] and Hurlen Larsen et al. [4] as discussed in section 2.5.2. Several studies by the authors concluded that AlMgSi(Cu) alloys were prone to pitting corrosion in an overaged state. This observation seem to be in accordance with present findings. In fact, as seen in figure 4.33, aggressive localized pitting attacks were found to coincide with the point of minimum hardness in alloy 6082-X / T6 subjected to weld simulation and post weld heat treatment. This reduction in hardness is believed to result from local overageing of the alloy in these regions.

In fact, attacks were observed at distances of -28 mm and 32 mm from the centre line, were the peak temperature has been close to 350 $^{\circ}\mathrm{C}$ during weld simulation. This temperature is not high enough in order for complete dissolution of the hardening precipitates β'' and β' to take place. Instead, coarsening of particles occur, forming a soft zone some distance from the 'weld' as shown by Myhr and Grong [18] in section 2.3.2. Finally, as weld simulation is followed by PWHT at 185 $^{\circ}\mathrm{C}$ for 5 hours, additional coarsening of the precipitates occurs, forming an overaged zone some distance away from the centre line. This effect was illustrated in figure 2.4 and 2.11. Finally, precipitaion of the anodic equilibrium phase, $\beta - Mg_2Si$, may have taken place which reduces the pitting resistance even further.

Moreover, as seen in chapter 2.6, the susceptibility to pitting corrosion increases with increasing Cu-content, due to formation of cathodic intermetallic particles [17, 46]. Results from this study are found to be in accordance with such reports, as both pit density, pit size and pit depth were observed to increase with increasing Cu concentration.

Furthermore, electrical conductivity measurements revealed decreasing concentration of solute in solid solution with increasing distance from the weld for both FSW and MIG welded samples. As a result, the regions closest to the weld metal could prove susceptible to pitting, due to the high level of solute atoms in solid solution. However, main alloying elements Mg and Si shift the potential in opposite direction, with the Mg atoms shifting the potential in a more negative direction and the Si atoms shifting it in a more positive direction. As a result, the net shift in potential is not expected to be substantial due to the ambivalent electrochemical behaviour. In fact, potential measurements for the MIG welded samples revealed a total variation of only 30 mV for the various sections (ref. figure 4.46). For the fusion zone in the MIG welded samples, on the other hand, an increase in pitting susceptibility should be expected due to the high Mg content in the filler metal. However, only a small negative shift of 20-30 mV in corrosion potential could be observed.

Nevertheless, even though the potential difference between the weld metal and the HAZ is low, it may still cause the weld metal to act as a sacrificial anode, protecting the HAZ in immediate proximity to the weld seam. This effect is discussed in greater detail in section 5.6.1.

5.6.1. Increased pitting resistance in the HAZ

The heat affected zone of both the MIG welded and the friction stir welded 6082-X samples displayed increased resistance towards pitting corrosion. Moreover, for the FSW samples increased pitting resistance was observed even in the base metal close to the HAZ. Such increased corrosion resistance for this region was unexpected and an obvious explanation could not be found. However, four possible suggestions for this increased corrosion resistance are listed below:

1. Favourable microstructure
2. Thermal oxidation of oxide layer close to the weld
3. Galvanic effects from the weld metal (MIG welded samples)
4. Selective corrosion of excess metal (FSW samples)

Moreover, it should be noted that the first explanation is believed to be the most probable due to extensive variations in the microstructure during the welding cycle.

1. Favourable microstructure

According to Svenningsen et al. [5], coarsening of precipitates and solute depletion of the aluminium matrix increases the driving force towards pitting corrosion. In the heat affected zone close to the fusion line, the temperature has been above the solvus temperature. This allows dissolution of hardening precipitates and some homogenisation of the aluminium matrix (fully reverted region). As a result, improved pitting resistance in the heat affected zone may be expected as compared to the base metal, where the microstructure is unaffected by the welding cycle and the density of precipitates is unchanged. However, in the partly reverted region some distance from the fusion line, reprecipitation of the hardening precipitates β' and β'' has taken place which is expected to reduce the corrosion resistance. Such observations were made for the welded samples, as the corrosion resistance was observed to decrease at distances of approximately 15 mm from the centre of the weld. Figure 5.2, based on work by Myhr et al. [18, 59] illustrates this effect. Moreover, increased resistance to pitting corrosion in high temperature regions was observed after IGC testing of weld simulated samples from T1 starting tempers. Results from this experiment are presented in figure 4.22 and table 4.2 and show increasing attacks from IGC and pitting corrosion with increasing distance from centre line for Cu containing alloys 6082-B and 6082-C.

In addition, the electrical conductivity was observed to be lower in the HAZ as compared to the base material. Such observations indicate increasing amount of alloying elements

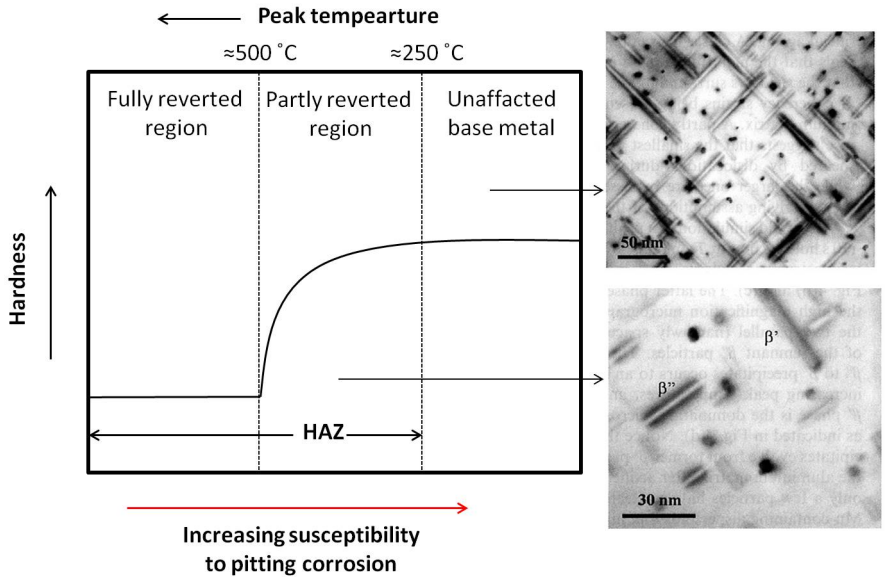

Figure 5.2.: *Effect of welding on the microstructure evolution and hence the corrosion resistance in artificially aged AlMgSi alloys. Precipitation of hardening particles β' and β'' is suggested to increase the susceptibility to pitting corrosion. Figure is based on ideas by Myhr et al. [18, 59].*

located in solid solution in this region, which support the above-mentioned explanation.

Furthermore, pitting corrosion is generally caused by precipitation of active intermetallic particles in the aluminium matrix. By considering the main alloying elements, Mg and Si, the main particle type reported to cause pitting corrosion is Mg_2Si, with a dissolution potential of -1190 mV_{SCE} [46, 48]. However, with increasing amount of Mg and Si located in solid solution in the HAZ, the susceptibility towards pitting corrosion from this particle type is reduced.

However, as seen in section 2.6, the role of MgSi particles on the pitting behaviour is not fully understood. Eckermann et al. [40] showed that dissolution of Mg from these particles started immediately after being immersion in a corrosive environment. The dissolution process left immune SiO particles and MgSi remnants in the matrix. The latter particle type was found to increase the cathodic current density by a factor of three. As a result, it appears as if Mg_2Si particles do have an impact on the overall pitting resistance, and the suggested mechanism for the HAZ may be valid.

The above-mentioned explanation, however, fails to explain why increased pitting resistance was observed in the HAZ for the FSW samples subjected to PWHT. By performing PWHT, reprecipitation of the hardening particles in the HAZ is expected, thus reducing the resistance to pitting corrosion. In fact, reprecipitation of hardening particles in the HAZ was confirmed by a substantial increase in hardness of this region as seen in figure 4.10. Also, the electrical conductivity was measured to increase in the HAZ after PWHT of the

friction welded samples. Such observations indicate that the amount of Mg and Si in solid solution decreases as precipitation of hardening particles take place.

However, by considering the difference in test duration between MIG welded and friction stir welded samples, the above-mentioned explanation may still prove valid. In fact, the FSW samples were only subjected to SWAAT testing for 15 days, whereas MIG welded samples were held for 25 days. As a result, the duration of 15 days may have been insufficient in order for pit initiation in the HAZ to occur. Also, the extent of reprecipitation in the HAZ for the friction welded samples may have been insufficient in order to cause pits to form. For the base metal far from the weld, on the other hand, pit initiation may be accelerated due to overageing which is reported to prove unfortunate with respect to pitting corrosion [4–10]. In fact, some overageing was observed for the T6-FSW samples during artificial ageing (section 4.2).

Moreover, for the FSW samples, the superior corrosion resistance was not limited to the heat affected zone. In fact, part of the base metal in proximity to the HAZ proved resistant to pitting corrosion. Such observations were made, despite the above-mentioned tendencies of overageing of the alloy which should favour pit initiation. A suggested mechanism for this increased corrosion resistance may be linked to selective corrosion of excess metal in the TMAZ which is discussed later in this section.

Finally, figure 4.26B and 4.27 shows extensive etching of the HAZ in MIG welded 6082-X / T6. These attacks are believed to be linked to the dark oxide layer/soot as a result of the welding process (figure 4.1), although no direct evidence was provided. However, no etching of the samples subjected to FSW was observed which should support mentioned oxide/soot-hypothesis.

2. Thermal oxidation of oxide layer

This hypothesis is regarded to be most applicable to the MIG welded samples, due to higher temperatures during the welding cycle.

The oxide layer on AlMgSi alloys are considered to consist of Al_2O3 and MgO [60, 61]. In the heat affected zone, close to the weld metal, the temperature has been elevated (500-600 $^{\circ}$C) during welding of the samples. At such high temperatures oxidation of the oxide layer could occur, resulting in changes in the composition or thickness of the oxide, and possibly also crystallization of the oxide. During the thermal cycle the oxide could also become enriched on Mg, thus improving the stability and corrosion resistance of the layer, and hence the overall corrosion resistance in the HAZ. In fact, Mizuno et al. [60] and Nylund et al. [61] reported that the amount, as well as the thickness, of MgO in the oxide layer was increasing with increasing temperature. However, due to the short period of time at elevated temperatures, such a course of events appear unlikely. As a result, this mechanism will not be discussed in any further detail in this work.

3. Galvanic effects from the weld metal (MIG)

The filler metal used during MIG welding was an Al-Mg alloy containing 4.8 wt % Mg (ref. table 3.2). As a result, highly anodic Al_3Mg_2 precipitates are expected to form in the weld metal, with a dissolution potential of -1150 mV_{SCE} [46]. As a result, selective dissolution of these particles are expected when exposed to a corrosive environment. Moreover, as the weld metal displayed a corrosion potential more negative than the base metal (figure 4.46), some galvanic effects during corrosion testing is expected. As a result, the base material in the HAZ close to the weld metal is expected to experience some protection from the weld metal, which acts as a sacrificial anode. This explanation is illustrated in shown in figure 5.3.

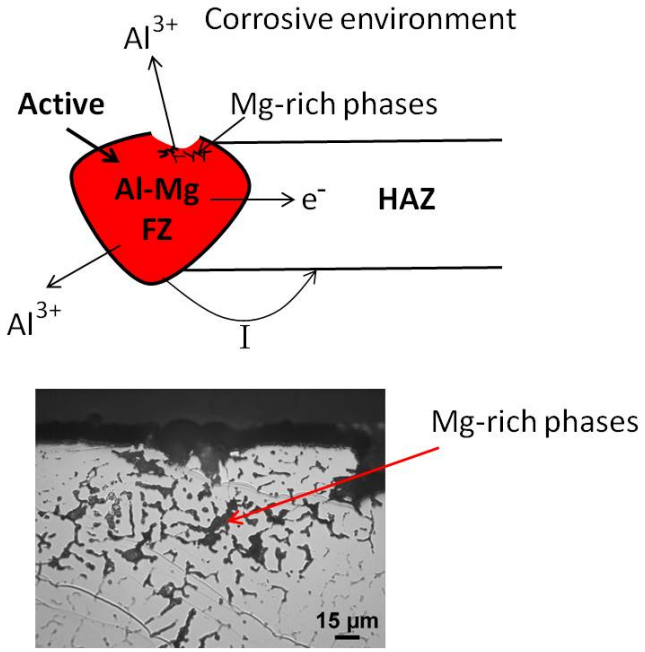

Figure 5.3.: *Active corrosion of the Mg-rich weld metal in MIG welded samples. As a result, the fusion zone (FZ) acts as a sacrificial anode protecting the HAZ in proximity to the weld.*

Moreover, the galvanic effect offered by the weld metal is only expected to include the region in immediate proximity to the weld metal. Such observations were in fact made on the MIG welded samples, as pits were observed at distances no more than 15 mm from the fusion line. As a result, the above-mentioned explanation may prove to be valid. Finally, the open circuit potential of the weld metal was observed to increase from approximately - 700 mV to -680 mV during the first hour of immersion. Such an increase in corrosion potential may be explained by dissolution of Mg from the weld metal, which has been reported to start immediately after immersion [40]. As a result, the weld metal may have offered some protection of the base metal, at least during the initiation stage.

4. Selective corrosion of excess metal (FSW)

As seen in figure 4.19, selective corrosion of excess material at the outer edge of the stir zone after welding was observed. This may have led to some protection of the HAZ, as the corrosion attacks appear to be concentrated to the region containing excess metal. However, hypotheses explaining why these corrosion attacks are limited to the location of excess metal are yet to be found. Nevertheless, a suggested mechanism may be segregation of alloying elements to the interface between the base metal and the outer edge of the weld. As a result, a local potential difference may be established at this interface causing pitting corrosion or IGC to take place. This mechanism will be discussed in some further detail in section 5.6.1.

5.6.2. Susceptibility of weld seam (FSW)

Pits were observed in the weld seam both after MIG welding and FSW. However, sampled welded by FSW proved particularly susceptible, and the pit density in the weld centre was observed to be considerable higher than for the base metal. By considering the mechanism illustrated in figure 5.2, the weld seam should prove resistant to pitting corrosion, as the temperature has been high during welding, thus allowing dissolution of hardening precipitates and improved pit resistance. As a result, another mechanism may be valid for the weld seam.

As already mentioned, segregation of alloying elements to the surface of the weld seam may take place which may cause the corrosion resistant to decrease. Moreover, the heavily deformed microstructure in the weld nugget contains a high density of dislocations which may act as accumulation sites for alloying elements. As a result, pitting corrosion may be initiated due to local potential differences between the accumulation site and the aluminium matrix. The existence of a deformed microstructure in the weld nugget was demonstrated by a substantial increase in hardness in this region as seen in figure 4.25. Also, a heavily deformed microstructure was characterised by the means of optical microscopy as shown in figure 4.3.

Furthermore, the deformation introduced to the metal during welding may cause larger second phase particles to break, forming smaller particles which causes the particle density to increase. The main second phase particle type observed in alloy 6082 is Fe-rich phases. As a result, the density of Fe-rich particles may be higher in the weld as compared to the base metal. As seen in section 2.6, Fe-rich phases are known to cause susceptibility to pitting corrosion [4, 14, 34, 46, 35].

5.7. Further work

Future work should include a more comprehensive analysis of intermetallic phase particles in alloy 6082, involving transmission electron microscopy (TEM) and X-ray diffraction (XRD). By performing such an analysis, a more profound understanding of grain boundary precipitates and hence corrosion susceptibility may be gained. In particular, the particle types responsible for the attacks from pitting corrosion across the welded section may be identified. Also, performing similar corrosion tests as used in this work on a fully recrystallized microstructure, may provide further insight into the importance of microstructure on the susceptibility towards IGC. Particular attention should be paid to the heat affected zone of samples subjected to FSW and MIG welding. Moreover, attempts should be made to understand the mechanisms responsible for the improved corrosion resistance observed for this region as compared to the base metal.

Furthermore, as aluminium alloy AA6082 tested in this study usually does not contain copper on an industrial scale, it would be interesting to study the effect of welding on other AlMgSi alloys that usually contain copper (e.g. AA6005, AA6061). Finally, other welding techniques may also be included such as tungsten inert gas welding (TIG), or the hybrid metal extrusion and bonding (HYB) joining technique. The latter joining method is a state of the art solid state welding technique, which has been reported to provide complete residual strength across the welded section after welding [22]. As a result, this technique may gain considerable momentum over the next decades, and it would be interesting to study the corrosion resistance of such welds.

Conclusion

In this master thesis four variants of AA6082 have been subjected to an accelerated IGC test and a Cyclic Acidified Synthetic Sea Water (Fog) Test (SWAAT test). Main conclusions that can be drawn on the basis of this study are as follows:

- The most aggressive corrosion attacks were seen after SWAAT testing of the alloys, and pitting corrosion was found to be the main corrosion mode in all samples tested.
- The heat affected zone in alloy 6082-X / T6 subjected to MIG welding, and FSW with subsequent PWHT, displayed increasing corrosion resistance as compared to the base material. Also, for the FSW weldments, increased pitting corrosion was observed in part of the base metal close to the HAZ.
- Moreover, the electrical conductivity was found to increase with increasing distance from the weld seam for both FSW and MIG welded samples. As a result, the extent of alloying elements located in solid solution is expected to be higher close to the weld seam, which is attributed to dissolution of hardening precipitates β' and β''. In fact, dissolution of such particles was confirmed by a reduction in hardness in the HAZ. Finally, decomposition of these hardening particles is believed to improve the corrosion resistance, which may explain the improved corrosion resistance observed in the HAZ after FSW and MIG welding.
- However, no significant variation in corrosion potential was observed across the welded section in MIG welded samples of alloy 6082-X / T6. Nevertheless, the Mg-rich weld metal may act as a sacrificial anode protecting parts of the HAZ, despite potential differences of no more than 30 mV.
- The importance of Cu content on pitting susceptibility became apparent as both pit density, pit size and pit depth were observed to increase with increasing Cu concentrations. Also, the total weight loss was found to increase rapidly with increasing Cu additions.
- The effect of PWHT on the corrosion resistance after the accelerated IGC test was observed to be minimal, and only a slight decrease in weight loss was observed.
- SWAAT testing of Cu-lean alloy 6082-X / T6 subjected to weld simulation and PWHT revealed aggressive pitting corrosion of narrow overaged regions. As a result, overageing was observed to increase the susceptibility to pitting corrosion. In fact, pit densities and pit depths were found to be comparable to those observed in 6082-B / T1 containing 0.10 wt% Cu.
- All alloys tested displayed a highly fibrous microstructure as a result of extrusion. For alloys 6082-A, 6082-B and 6082-C no recrystallized layer was observed. Such observations are believed to prove beneficial with respect to IGC resistance, as most grains are separated by low angle boundaries. For alloy 6082-X, on the other hand,

a defined recrystallized layer of approximately 150 μm was observed which is expected to increase the susceptibility to IGC, as recrystallized grains are separated by high angle boundaries. However, the lack of copper in this alloy render it rather resistant to attacks from IGC, and only superficial attacks were observed after SWAAT testing.

- Attacks from pitting corrosion were often observed to be accompanied by IGC along sub grains, particularly in the base metal in alloys 6082-B and 6082-C with Cu concentrations of 0.10 and 0.60 wt% respectively. Also, the deepest pits were observed in high temperature regions (> 450 $^{\circ}\mathrm{C}$), whereas low temperature regions (<300 $^{\circ}\mathrm{C}$) where characterised by larger more shallow pits.

- The weld seam formed during FSW proved more susceptible to attacks from pitting corrosion than the weld seam formed during MIG welding. Such results may be explained by accumulation of alloying elements in the highly deformed friction stir weld, causing a local potential difference between the accumulation site and the aluminium matrix. However, no evidence supporting this hypothesis were provided. Also, PWHT was performed on FSW samples only.

- EDS analyses in LV-FESEM revealed that Cu-rich phases in alloy 6082-C contained substantial amounts of Fe and Si in addition to some Mn. These observations are believed to reduce the overall susceptibility to IGC. However, the characteristic Q-phase ($A_{l4}Mg_8Si_7Cu_2$), frequently reported to cause IGC in AlMgSi alloys, were not observed. Moreover, Fe-rich phases were found to contain significant amounts of Si in addition to some Mn, which should render these phases less harmful. Nevertheless, as already mentioned, aggressive attacks from pitting corrosion were still observed, particularly for Cu-rich or overaged alloys.

- Finally, alloys 6082-A, 6082-B and 6082-C displayed low susceptibility to artificial ageing. In fact, samples that were claimed to be peak aged, showed similar hardness values as the naturally aged samples of the same alloy. As a result, all samples of the above-mentioned alloys were designated a T1 starting temper condition. The reduced effect from artificial ageing is believed to result from low densities of quenched-in vacancies clusters or solute. Alloy 6082-X, on the other hand, displayed expected hardness values after artificial ageing.

References

[1] SINTEF. Arctic materials. http://www.sintef.no/Projectweb/Arctic-Materials/, September 2013. Accessed: 04/06/2013.

[2] Hydro. Aluminium for Future Generations®. http://recycling.world-aluminium.org/home.html, September 2013. Accessed: 01/06/2013.

[3] Jan Ketil Solberg. *Teknologiske metaller og legeringer*. Institutt for materialteknologi, NTNU, 2009. **215-217**.

[4] Magnus Hurlen Larsen. *Effect of composition and thermomechanical processing on the intergranular corrosion of AA6000 aluminium alloys*. NTNU, 2010.

[5] G Svenningsen, MH Larsen, JC Walmsley, JH Nordlien, and K Nisancioglu. Effect of artificial aging on intergranular corrosion of extruded AlMgSi alloy with small Cu content. *Corrosion science*, 48(6):**1528–1543**, JUN 2006.

[6] Magnus Hurlen Larsen, John Charles Walmsley, Otto Lunder, Ragnvald H. Mathiesen, and Kemal Nisancioglu. Intergranular corrosion of copper-containing AA6xxx AlMgSi aluminum alloys. *Journal of the electrochemical society*, 155(11):**C550–C556**, 2008.

[7] Magnus Hurlen Larsen, John Charles Walmsley, Otto Lunder, and Kemal Nisancioglu. Effect of Excess Silicon and Small Copper Content on Intergranular Corrosion of 6000-Series Aluminum Alloys. *Journal of the electrochemical society*, 157(2):**C61–C68**, 2010.

[8] G Svenningsen, MH Larsen, JH Nordlien, and K Nisancioglu. Effect of high temperature heat treatment on intergranular corrosion of AlMgSi(Cu) model alloy. *Corrosion science*, 48(1):**258–272**, JAN 2006.

[9] Gaute Svenningsen, Magnus Hurlen Larsen, Jan Halvor Nordlien, and Kemal Nisancioglu. Effect of thermomechanical history on intergranular corrosion of extruded AlMgSi(Cu) model alloy. *Corrosion science*, 48(12):**3969–3987**, DEC 2006.

[10] G Svenningsen, JE Lein, A Bjorgum, JH Nordlien, YD Yu, and K Nisancioglu. Effect of low copper content and heat treatment on intergranular corrosion of model AlMgSi alloys. *Corrosion science*, 48(1):**226–242**, JAN 2006.

[11] H. Zhan, J. M. C. Mol, F. Hannour, L. Zhuang, and J. H. W. Terryn, H.and de Wit. The influence of copper content on intergranular corrosion of model AlMgSi(Cu) alloys. *Materials and corrosion-werkstoffe und korrosion*, 59(8):**670–675**, AUG 2008.

[12] H.S. Hasting. *Clustering and precipitation in 6xxx Al alloys : TEM and APT studies*. Department of Physics, NTNU, 2006.

[13] Y. Liu, X. Zhou, G. E. Thompson, T. Hashimoto, G. M. Scamans, and A. Afseth. Precipitation in an AA6111 aluminium alloy and cosmetic corrosion. *Acta Materiala*, 55(1):**353–360**, JAN 2007.

[14] L.F. Mondolfo. *Aluminum alloys : structure and properties*. Butterworths, 1976.

[15] T Minoda and H Yoshida. The effect of microstructure on intergranular corrosion resistance of 6061 alloy extrusion. 331-3(Part 1-3):**1689–1694**, 2000. 7th International Conference on Aluminium Alloys (ICAA7), Charlottesville, Virginia, APR 09-14, 2000.

[16] Gene Mathers. *Welding of Aluminium and Its Alloys*. Boca Raton, Fla, 2002.

[17] Alumatter. Corrosion and corrosion control. `http://aluminium.matter.org.uk/content/html/eng/default.asp?catid=177&pageid=2144416642`, 2013. Accessed: 19/05/2013.

[18] OR Myhr, O Grong, HG Fjaer, and CD Marioara. Modelling of the microstructure and strength evolution in Al-Mg-Si alloys during multistage thermal processing. *Acta Materiala*, 52(17):**4997–5008**, OCT 2004.

[19] OR Myhr, S Klokkehaug, O Grong, HG Fjaer, and AO Kluken. Modelling of Microstructure Evolution and Residual Stresses in Processing and Welding of 6082 and 7108 Aluminium Alloys. *Welding Research*, pages **1–6**, JUN 1998.

[20] O. R. Myhr and O. Grong. A Combined Precipitation, Yield Strength and Work Hardening Model for Al-Mg-Si Alloys. 11th International Summer School on Aluminium Alloy Technology, Thermo-mechanical Processing and Forming, Trondheim, Norway, 20-24 June, 2011.

[21] C. D. Marioara, S. J. Andersen, T. N. Stene, H. Hasting, J. Walmsley, A. T. J. Van Helvoort, and R. Holmestad. The effect of Cu on precipitation in Al-Mg-Si alloys. *Philosophical magazine*, 87(23):**3385–3413**, 2007.

[22] Oystein Grong. Recent Advances in Solid-State Joining Of Aluminum. *Welding journal*, 91(1):**26–33**, JAN 2012.

[23] S. Esmaeili and D. J. Lloyd. The role of copper in the precipitation kinetics of 6000 series Al alloys. volume 519-521, pages **169–176**, 2006.

[24] DJ Chakrabarti and DE Laughlin. Phase relations and precipitation in Al-Mg-Si alloys with Cu additions. *Progress in Materials Science*, 49(3-4):**389–410**, 2004.

[25] Wolverton C. Crystal structure and stability of complex precipitate phases in Al-Cu-Mg-(Si) and Al-Zn-Mg alloys. *Acta Materiala*, 49(16):**3129–3142**, 2001.

[26] WA Metwally and M Mosalam. Susceptibility of some 6000 Al weldments to pitting and intergranular corrosion. *Metall*, 50(2):**106–109**, 1996.

[27] O. R. Myhr and O. Grong. Novel modelling approach to optimisation of welding conditions and heat treatment schedules for age hardening Al alloys. *Science and technology of welding and joining*, 14(4):**321–332**, MAY 2009.

[28] Stefano Maggiolino and Chiara Schmid. Corrosion resistance in FSW and in MIG welding techniques of AA6XXX. *Journal of materials processing technology*, 197(1-3):**237–240**, FEB 1 2008.

[29] V. Fahimpour, S. K. Sadrnezhaad, and F. Karimzadeh. Corrosion behavior of aluminum 6061 alloy joined by friction stir welding and gas tungsten arc welding methods. *Materials and design*, 39:**329–333**, AUG 2012.

[30] P. M. G. P. Moreira, A. M. P. de Jesus, A. S. Ribeiro, and P. M. S. T. de Castro. Fatigue crack growth in friction stir welds of 6082-T6 and 6061-T6 aluminium alloys: A comparison. *Theoretical and applied fracture mechanics*, 50(2):**82**, OCT 2008.

[31] O Frigaard, O Grong, and OT Midling. A process model for friction stir welding of age hardening aluminum alloys. *Metallurgical and materials transactions a-physical metallurgy and materials science*, 32(5):**1189–1200**, MAY 2001.

[32] Oystein Grong. *Metallurgical Modelling of Welding*. The Institute of Materials, 2nd edition, 1997.

[33] Kemal Nisancioglu. Corrosion of AlMgSi alloys with Cu additions : final report. Technical report, *SINTEF rapport (SINTEF. Avdeling for metallurgi)*, 1980.

[34] K Nisancioglu. Electrochemical-behavior of aluminum-base intermetallics containing iron. *Journal of the electrochemical society*, 137(1):**69–77**, JAN 1990.

[35] JO Park, CH Paik, YH Huang, and RC Alkire. Influence of Fe-rich intermetallic inclusions on pit initiation on aluminum alloys in aerated NaCl. *Journal of the electrochemical society*, 146(2):**517–523**, FEB 1999.

[36] L.F. Mondolfo. *Manganese in aluminium alloys* . Neuilly sur Seine : Manganese Centre, 1977. **42-46**.

[37] R. Chadwick. The effect of iron, manganese, and chromium on the properties in sheet form of aluminium alloys containing 0.7-percent magnesium and 1.0-percent silicon. *Journal of the institute of metals*, 82(2):**75**, 1953.

[38] Iduvirges L. Muller and Jose R. Galvele. Pitting potential of high-purity binary aluminium-alloys .2. Al-Mg and Al-Zn alloys. *Corrosion science*, 17(12):**995–1007**, 1977.

[39] AK Bhattamishra and K Lal. Microstructural studies on the effect of Si and Cr on the intergranular corrosion in Al-Mg-Si alloys. *Materials and design*, 18(1):**25–28**, 1997.

[40] Fabian Eckermann, Thomas Suter, Peter J. Uggowitzer, Andreas Afseth, and Patrick Schmutz. The influence of MgSi particle reactivity and dissolution processes on corrosion in Al-Mg-Si alloys. *Electrochim. Acta*, 54(2):**844–855**, DEC 30 2008.

[41] Tokinori Onda, Yoji Hirano and Takeyoshi Doko. Effect of Mg and Si addition on the intergranular corrosion of aluminium alloy. *Society of Automotive Engineers*, 268 19:**217–219**, 1993.

[42] Kamal El-Menshawy, Abdel-Wahab A. El-Sayed, Mohammed E. El-Bedawy, Hafez A. Ahmed, and Saed M. El-Raghy. Effect of aging time at low aging temperatures on the corrosion of aluminum alloy 6061. *Corrosion science*, 54:**167–173**, JAN 2012.

[43] GS Frankel. Pitting corrosion of metals - A review of the critical factors. *Journal of the electrochemical society*, 145(6):**2186–2198**, JUN 1998.

[44] George E. Totten and D. Scott MacKenzie. *Handbook of aluminum, Vol. 2, Alloy production and materials manufacturing*. Boca Raton, Fla. : Taylor and Francis/Marcel Dekker, 2003. ch. **11**.

[45] Einar Bardal. *Korrosjon og korrosjonsvern*. Tapir Forlag, 1985. **112-121**.

[46] Dr. Martin P. Schmidt Christian Vargel, Michel Jacques. *Corrosion of aluminium*. Elsevier, 1st edition, 2004. **113-121**.

[47] Muller Il and Galvele jr. Pitting potential of high-purity binary aluminium-alloys .1. Al-Cu alloys - pitting and intergranular corrosion. *Corrosion science*, 17(3):**179**, 1977.

[48] KS Rao and KP Rao. Pitting corrosion of heat-treatable aluminium alloys and welds: A reveiw. *Transactions of the Indian Institute of Metals*, 57(6):**593–610**, DEC 2004.

[49] Einar Bardal. *Korrosjonsprøving - korttidsmetoder. Sammenfattende sluttrapport*, del 1, STF16 A77034. Korrosjonssenteret, SINTEF, Trondheim, 1977.

[50] Ye Ruan, Xiao Ming Qiu, and Wen Biao Gong. Corrosion behavior of 6082-T6 Al joint welded with Twin Wire MIG. 418-420(Part 1-3):**1368–1374**, 2012.

[51] T. Monetta, M. Montuori, A. Squillace, F. Bellucci, and D. B. Mitton. The effect of heat treatment and welding parameters on the corrosion behaviour of a friction stir welded 6056 aluminium alloy. 38:**285–297**, 2008.

[52] ESAB. Ok autrod 5183. `http://products.esab.com/Templates/T041.asp?id=131503`, 2013. Accessed: 09/06/2013.

[53] Rolf-Ulrich Kopp Kay Geels, Daniel B. Fowler and Michael Ruckert. *Metallographic and materialographic specimen preparation, light microscopy, image analysis and hardness testing*. ASTM International, 2007.

[54] Corrosion of metals and alloys - Determination of resistance to intergranular corrosion of solution heat-treatable aluminium alloys, Standard BS 11846:1995, *British Standards Institution*, 1995.

[55] Ane Thorvaldsen. Korrosjonsoppførsel til ulike AA6082 ved forskjellige sveisemetoder. Bachelor Thesis, HiST, 2013.

[56] Standard Pratice for Modified Salt Spray (FOG) Testing, Designation: G85 - 11, 2011.

[57] Standard Practice for the Preparation of Substitute Ocean Water, Designation: D1141 - 98, 2003.

[58] Sieniawski J Mrowka-Nowotnik G and Wierzbinska M. Intermetallix phase particles in 6082 aluminium alloy. *Archives of Materials Science and Engineering*, 28(2):**69–76**, 2007.

[59] OR Myhr, S Klokkehaug, O Grong, HG Fjaer, and AO Kluken. Modeling of microstructure evolution, residual stresses and distortions in 6082-T6 aluminum weldments. *Welding journal*, 77(7):**286S–292S**, JUL 199.

[60] K Mizuno, A Nylund, and I Olefjord. Surface analysis of oxide formed during heat treatment of Al-Mg-Si alloys. *Materials science and technology*, 12(4):**306–314**, APR 1996.

[61] A Nylund, K Mizuno, and I Olefjord. Influence of Mg and Si on the oxidation of aluminum. *Oxidations of metals*, 50(3-4):**309–325**, OCT 1998.

A SWAAT - Inspection form

Table A.1.: *Regular inspections form during SWAAT testing of samples [55].*

Day	Chamber temp. (°C)	Air pressure (bar)	Fallout (mL/h)	Fallout (pH)	Salt solution conc. (%)	Time (h)
4	48.4	1.6	0.757	3.28	3.9	70
5	49.1	1.6			3.8	92
6	49.0	1.6			3.8	110
7	42.0	1.7	0.908	3.3	3.9	131
8	48.9	1.6			3.8	
9	49.9	1.6			3.8	
10	50.0	1.6	0.894	3.29	3.8	207
11	48.4	1.6			3.8	224
12	50.1	1.6			3.9	251
13	51.3	1.6	0.961	3.29	3.8	261
14	49.1	1.6			3.8	284
15	48.0	1.6	0.964	3.2	3.9	308
16	49.2	1.6			3.9	337
17	46.9	1.6	0.978	3.35	3.8	364
18	48.9	1.6			3.8	389
19	50.5	1.6	0.985	3.37	3.9	407
20	50.5	1.6			3.9	427
21	50.6	1.6	0.983	3.38	3.9	460
22	50.7	1.6			3.9	484
23	50.2	1.6			3.9	503
24	50.4	1.6			3.9	524
25	49.0	1.6			3.9	558
26	49.2	1.6	0.954	3.4	3.9	572

B | Pitting measurements

Table B.1.: *Pit densities after SWAAT testing of weld simulated samples (WS) and samples subjected to MIG and FSW welding. Distance refers to position from centre line or weld. Note that no standard deviation is presented as all visible pits within the given area of* $20\ cm^2$ *were counted.*

6082-A / T1 WS	**Pits**	**Density** (cm^{-2})	**6082-B / T1 WS**	**Pits**	**Density** (cm^{-2})
0-1 cm	6	0.30	0-1 cm	17	0.85
1-2 cm	7	0.35	1-2 cm	14	0.7
2-3 cm	9	0.45	2-3 cm	10	0.5
3-4 cm	7	0.35	3-4 cm	16	0.8
4-5 cm	0	0.00	4-5 cm	11	0.55
Sum	**29**		**Sum**	**68**	
6082-C / T1 WS	**Pits**	**Density** (cm^{-2})	**6082-X / T6 WS**	**Pits**	**Density** ($cm^{-2)}$
0-1 cm	16	0.8	0-1 cm	16	0.8
1-2 cm	18	0.9	1-2 cm	11	0.55
2-3 cm	15	0.75	2-3 cm	12	0.6
3-4 cm	15	0.75	3-4 cm	22	1.1
4-5 cm	11	0.55	4-5 cm	5	0.25
Sum	**75**		**Sum**	**66**	
6082-X / T6 MIG	**Pits**	**Density** (cm^{-2})	**6082-X / T6 FSW**	**Pits**	**Density** (cm^{-2})
0-1 cm	4	0.2	0-1 cm	17	0.85
1-2 cm	10	0.5	1-2 cm	5	0.25
2-3 cm	18	0.9	2-3 cm	7	0.35
3-4 cm	22	1.1	3-4 cm	5	0.25
4-5 cm	22	1.1	4-5 cm	10	0.5
Sum	**76**		**Sum**	**44**	

Table B.2.: *Pit diameters after SWAAT testing of weld simulated samples (WS) and samples subjected to MIG and FSW welding. Distance refers to position from centre line or weld. Test area* 20 cm^2. *SD = Standard Deviation.*

6082-A / T1 WS	**Diameter (mm)**			**Average (mm)**	**SD (mm)**	**6082-B / T1 WS**	**Diameter (mm)**			**Average (mm)**	**SD (mm)**
Distance	*#1*	*#2*	*#3*			*Distance*	*#1*	*#2*	*#3*		
0-1 cm	0.3	0.6	0.4	*0.4*	*0.2*	0-1 cm	2.6	1.7	1.3	*1.9*	*0.7*
1-2 cm	0.6	0.3	1.1	*0.7*	*0.4*	1-2 cm	0.9	1.0	1.2	*1.0*	*0.2*
2-3 cm	1.0	0.5	0.5	*0.7*	*0.3*	2-3 cm	0.6	1.1	1.3	*1.0*	*0.4*
3-4 cm	0.5	0.3	0.3	*0.4*	*0.1*	3-4 cm	0.8	1.1	0.8	*0.9*	*0.2*
4-5 cm	0.4			*0.4*	-	4-5 cm	0.8	1.1	1.4	*1.1*	*0.3*
Average				**0.5**		**Average**				**1.2**	

6082-C / T1 WS	**Diameter (mm)**			**Average (mm)**	**SD (mm)**	**6082-X / T6 WS**	**Diameter (mm)**			**Average (mm)**	**SD (mm)**
Distance	*#1*	*#2*	*#3*			*Distance*	*#1*	*#2*	*#3*		
0-1 cm	1.7	1.4	0.6	*1.2*	*0.6*	0-1 cm	0.3	0.5	0.5	*0.4*	*0.1*
1-2 cm	1.9	0.9	1.6	*1.5*	*0.5*	1-2 cm	0.5	0.4	0.3	*0.4*	*0.1*
2-3 cm	1.3	2.9	1.8	*2.0*	*0.8*	2-3 cm	0.7	0.3	0.5	*0.5*	*0.2*
3-4 cm	5.0	1.3	1.3	*2.5*	*2.1*	3-4 cm	0.7	0.3	0.9	*0.6*	*0.3*
4-5 cm	3.0	1.5	2.1	*2.2*	*0.8*	4-5 cm	0.4	0.8	0.9	*0.7*	*0.3*
Average				**1.9**		**Average**				**0.5**	

6082-X / T6 MIG	**Diameter (mm)**			**Average (mm)**	**SD (mm)**	**6082-X / T6 FSW**	**Diameter (mm)**			**Average (mm)**	**SD (mm)**
Distance	*#1*	*#2*	*#3*			*Distance*	*#1*	*#2*	*#3*		
0-1 cm	0.5	0.4	0.3	*0.4*	*0.1*	0-1 cm	0.5	0.3	0.3	*0.4*	*0.1*
1-2 cm	0.6	0.5	0.4	*0.5*	*0.1*	1-2 cm	0.4	0.4	0.4	*0.4*	*0.0*
2-3 cm	0.5	0.6	0.2	*0.4*	*0.2*	2-3 cm	0.2	0.5	0.4	*0.4*	*0.2*
3-4 cm	0.5	0.4	0.2	*0.4*	*0.2*	3-4 cm	0.3	0.2	0.3	*0.3*	*0.1*
4-5 cm	0.5	0.3	0.2	*0.3*	*0.2*	4-5 cm	0.4	0.3	0.5	*0.4*	*0.1*
Average				**0.4**		**Average**				**0.4**	

Table B.3.: *Pit depths after SWAAT testing of weld simulated samples (WS) and samples subjected to MIG and FSW welding. Distance refers to position from centre line or weld. Test area* $20\ cm^2$. *SD = Standard Deviation.*

6082-A / T1 WS	**Depth** (μm)			**Average** (μm)	**SD** (μm)
Distance	*#1*	*#2*	*#3*		
0-1 cm	120	370	370	*287*	*144*
1-2 cm	170	110	280	*187*	*86*
2-3 cm	260	170	360	*263*	*95*
3-4 cm	140	250	150	*180*	*61*
4-5 cm	160			*160*	-
Average				**215**	

6082-B / T1 WS	**Depth** (μm)			**Average** (μm)	**SD** (μm)
Distance	*#1*	*#2*	*#3*		
0-1 cm	800	700	300	*600*	*265*
1-2 cm	550	350	600	*500*	*132*
2-3 cm	400	300	600	*433*	*153*
3-4 cm	300	300	300	*300*	*0.0*
4-5 cm	320	150	620	*363*	*238*
Average				**439**	

6082-C / T1 WS	**Depth** (μm)			**Average** (μm)	**SD** (μm)
Distance	*#1*	*#2*	*#3*		
0-1 cm	670	700	900	*757*	*125*
1-2 cm	1100	460	1150	*903*	*385*
2-3 cm	750	600	450	*600*	*150*
3-4 cm	300	150	180	*210*	*79*
4-5 cm	530	450	900	*627*	*240*
Average				**619**	

6082-X / T6 WS	**Depth** (μm)			**Average** (μm)	**SD** (μm)
Distance	*#1*	*#2*	*#3*		
0-1 cm	370	560	350	*427*	*115*
1-2 cm	480	390	320	*397*	*80*
2-3 cm	400	430	410	*413*	*15*
3-4 cm	400	250	260	*303*	*84*
4-5 cm	350	300	360	*337*	*32*
Average				**375**	

6082-X / T6 MIG	**Depth** (μm)			**Average** (μm)	**SD** (μm)
Distance	*#1*	*#2*	*#3*		
0-1 cm	170	430	310	*303*	*130*
1-2 cm	400	380	390	*390*	*10*
2-3 cm	380	320	330	*343*	*32*
3-4 cm	110	360	310	*260*	*132*
4-5 cm	400	110	300	*270*	*147*
Average				**287**	

6082-X / T6 FSW	**Depth** (μm)			**Average** (μm)	**SD** (μm)
Distance	*#1*	*#2*	*#3*		
0-1 cm	360	70	70	*167*	*167*
1-2 cm	340	100	50	*163*	*155*
2-3 cm	460	330	350	*380*	*70*
3-4 cm	370	330	340	*345*	*21*
4-5 cm	330	420	120	*290*	*153*
Average				**269**	

C | Temperature profiles during weld simulation

This appendix includes the temperature profiles for all weld simulated samples. However, the profiles are observed to be similar and only small variations in the peak temperature cam be observed. Most variation was observed for alloy 6082-X where the peak temperature was slightly lower than for alloys 6082-A, 6082-B and 6082-C.

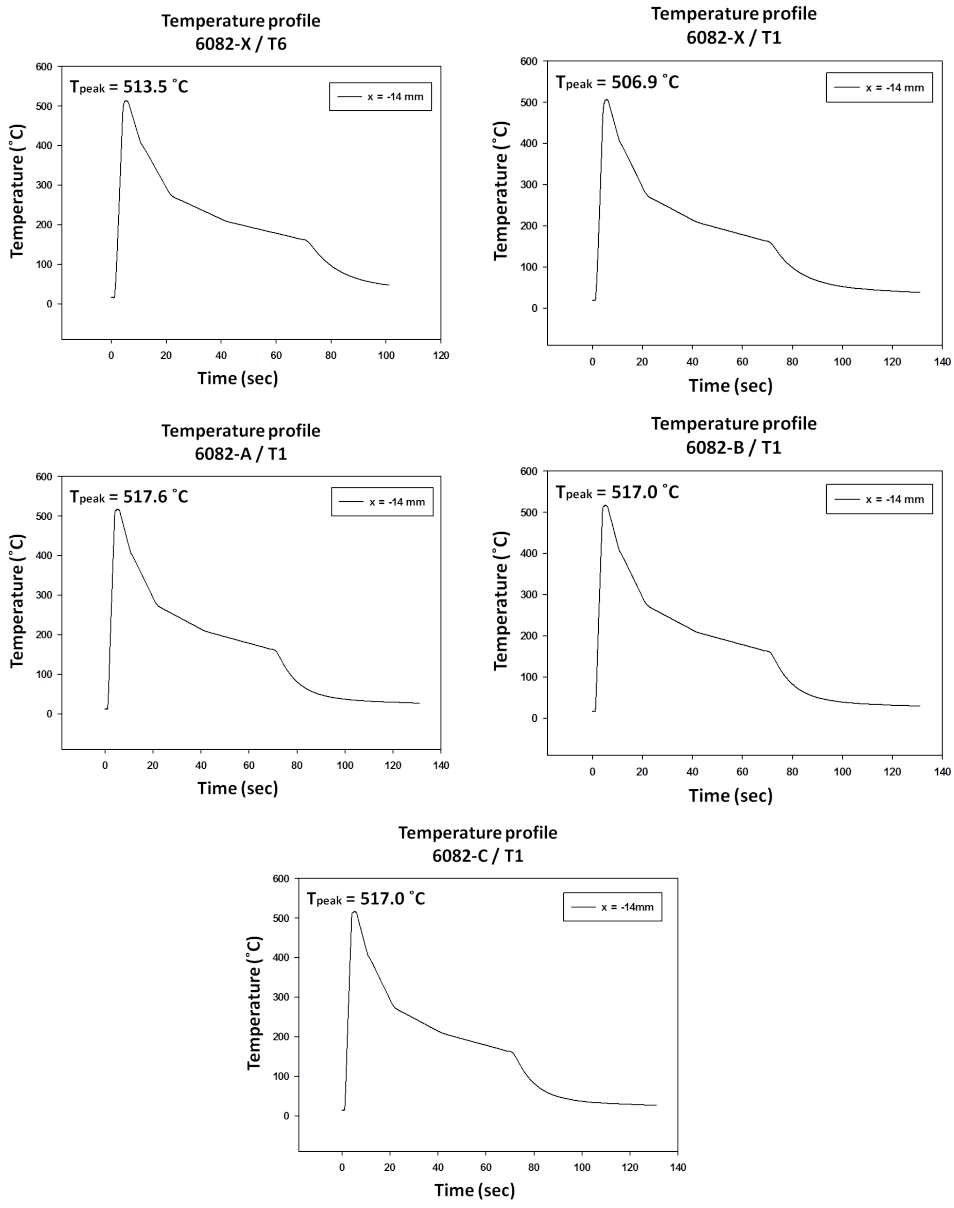

Figure C.1.: *Temperature profiles during weld simulation of all weld simulated alloys. Note the position of the profile being located -14 mm from the centre line (i.e. in the heat affected zone).*

D | Electrical conductivity measurements

Table D.1.: *Electrical conductivity measurements across the welded section for alloy 6082-X /T6 subjected to MIG and FSW. Measurements were taken in the plane of extrusion and are given in MS/m. SD = Standard Deviation.*

	6082-T6/ FSW			6082-T6/ FSW + PWHT		
	Weld	**HAZ**	**Base metal**	**Weld**	**HAZ**	**Base metal**
#1	25.8	27.5	28.6	27.3	28.9	29.2
#2	25.9	26.8	28.6	27.4	28.9	29.2
#3	26.1	27.0	28.7	27.5	28.8	29.3
#4	25.9	27.3	28.2	27.6	28.7	29.3
#5	25.9	28.4	28.7	27.4	28.9	29.2
#6	25.8	27.5	28.7	27.4	28.9	29.3
Average	**25.9**	**27.4**	**28.6**	**27.4**	**28.9**	**29.3**
SD	0.1	0.6	0.2	0.1	0.1	0.1

	6082-T6 / MIG		
	Weld	**HAZ**	**Base metal**
#1	17.7	28.2	28.6
#2	19.8	27.4	28.4
#3	17.9	28.2	28.3
#4	18.4	27.5	28.3
#5	18.2	28.4	28.4
#6	18.6	28.0	28.4
Average	**18.4**	**28.0**	**28.4**
SD	0.7	0.4	0.1